Numerical modelling of soot formation and evolution in laminar flames with detailed kinetics

Agnes Livia Bodor

NNT : 2019SACLC050

Numerical modeling of soot formation and evolution in laminar flames with detailed kinetics

Thèse de doctorat de Policecnico di Milano et de l'Université Paris-Saclay, préparée à CentraleSupélec

École doctorale n°579 Sciences Mécaniques et Energétiques, Matériaux et Géosciences (SMEMAG)
Spécialité de doctorat: Combustion

Thèse présentée et soutenue Milan, le 4 juillet 2019, par

Mlle Agnes Livia Bodor

Composition du Jury :

Prof. Andrea D'Anna
Professeur, Università degli Studi di Napoli Federico II — Rapporteur, Présidente

Dr. Silvana De Iuliis
CNR Researcher (DR), Istituto di Chimica della Materia Condensata e di Tecnologie per l'Energia — Rapporteur

Prof. Alberto Cuoci
Professeur, Politecnico di Milano — Directeur de Thèse

Prof. Nasser Darabiha
Professeur, CentraleSupélec - Paris – Saclay — Directeur de Thèse

Dr. Benedetta Franzelli
CNRS Researcher (CR), CentraleSupélec - Paris – Saclay — Examinateur

Thèse de doctorat

université PARIS-SACLAY

Politecnico di Milano

NNT : 2019SACLC050

Thèse de doctorat

Numerical modeling of soot formation and evolution in laminar flames with detailed kinetics

Coltutelle Doctoral Thesis of Politecnico di Milano and Université Paris-Saclay

Prepared at :

Policecnico di Milano, Department of Chemistry, Materials, and Chemical Engineering

CentraleSupélec Doctoral school n°579 Sciences Mécaniques et Energétiques, Matériaux et Géosciences

Speciality of the PhD: Chemical Engineering, Combustion

The Thesis was presented in Milano on the 4th of July 2019, by

Ágnes Livia Bodor

Composition of the Jury :

Prof. Andrea D'Anna Full Professor, Università degli Studi di Napoli Federico II	Reviewer, President
Dr. Silvana De Iuliis CNR Researcher (DR), Istituto di Chimica della Materia Condensata e di Tecnologie per l'Energia	Reviewer
Prof. Alberto Cuoci Associate Professor, Politecnico di Milano	Thesis Director
Prof. Nasser Darabiha Full Professor, CentraleSupélec - Paris – Saclay	Thesis Director
Dr. Benedetta Franzelli CNRS Researcher (CR), CentraleSupélec - Paris – Saclay	Examiner

Acknowledgment

I would like to thank to Professors Tiziano Faravelli and Nasser Darabiha for their support. I wish to thank to my supervisor Professor Alberto Cuoci for his guidance and support throughout my PhD. I would like to especially thank to Dr. Benedetta Franzelli for the fruitful discussions and her constant support, encouragement and interest. I would also like to thank the members of my committee Professor Andrea D'Anna and Dr. Silvana Di Iluiis for their feedback and suggestions, which helped me to further improve the quality of this work. I would like to thank to Isabella Branca for her essential support in the labyrinths of bureaucracy and everyday life.

I would like to thank to my labmates both at Politecnico di Milano and at Cetrale Supélec for their support in science and for the amazing time I had with them, and whom I would love to list, but luckily the length of the list would exceed the page. I would like to thank to all my friends outside of the labs for their support and the happy times we had along the way. At last, but certainly not at least, I would like to thank to my beloved family for standing next to me through this whole process.

I would like to thank for the founding provided by the European Union's Horizon 2020 research and innovation program under the Marie Sklodowska-Curie Grant Agreement No 643134.

Contents

List of Figures

List of Tables

Nomenclature

α_T	Soot particle thermal accommodation coefficient
β	Evaporation efficiency correction coefficient
$\dot{\Omega}$	Chemical source term
$\dot{\omega}$	Reaction specific chemical reaction rate
$\dot{\Omega}_{\text{abs}}$	Energy flux due to laser absorption
$\dot{\Omega}_{\text{cond}}$	Energy flux due to heat conduction
$\dot{\Omega}_{\text{evap}}$	Energy flux related to evaporation
$\dot{\Omega}_{\text{int}}$	Internal energy change
$\dot{\Omega}_{\text{rad}}$	Radiative heat loss
γ^*	Average value of the specific heat ratio
$\Gamma_{v,s}$	Diffusion coefficient of the soot vapor
λ	Excitation wavelength
λ_δ	Mean free path of gas molecules within the layer of δ thickness
μ	Stoichiometric coefficient of products
ν	Stoichiometric coefficient of reactants
ρ	Mixture density
ρ_{pp}	Primary particle number density
ρ_{soot}	Soot density
$\bar{V}$	Diffusion velocity
$\bar{v}$	Flow velocity

A	Frequency factor
BIN	Soot section
C_{abs}	Absorption cross section
C_{r}	Correction constant for surface rounding
d_{amean}	Arithmetic mean diameter
d_{CMD}	Count median diameter
d_{geom}	Geometrical mean diameter
d_{mono}	Mean d_{pp} derived with assuming monodisperse distribution
$d_{\text{pp,mean}}$	Mean primary particle diameter
$d_{\text{pp},N_{\text{min}}}$	Diameter of smallest soot particle accounted in mean d_{pp} calculation
E	Soot-absorption function
E_{a}	Activation energy
F	Temporal intensity profile of the laser
f	Eucken factor
$H_{\text{v,s}}$	Enthalpy of the vaporized soot
I_{ox}	Oxidation rate
I_{Sg}	Surface growth rate
J_{evap}	Evaporated mass current
k	Kinetic constant
k_{g}	Conduction coefficient for the surrounding gas
M	Molecular weight
m	Complex index of soot refraction
M_{g}	Molecular weight of the gas
m_{p}	Particle mass
$M_{\text{v,s}}$	Molar mass of the soot vapor
n	Temperature exponent in the Arrhenius formula
N_{Av}	Avogadro constant
N_{a}	Number of aggregate soot sections
$N_{\text{C,s}}$	Flux of molecules leaving the surface in the continuum regime
$N_{\text{Fm,s}}$	Flux of molecules leaving the surface in the free molecular regime

N_{g}	Number of gaseous species
n_{pp}	Primary particle number in molecule
N_{s}	Index of smallest BIN with solidified particles
$N_{\mathrm{v,s}}$	Flux of molecules leaving the surface in the transition regime
$p_{\mathrm{C,s}}$	Vapor pressure of the evaporating carbon species
p_{g}	Gas pressure
R	Reaction rate
R_{u}	Universal gas constant
S	Surface
S_{Birth}	Birth rate of primary particles
S_{Death}	Consumption rate of primary particles
S_{nuc}	Nucleation rate
V	Volume
X	Non-aggregate chemical species
Y	Species mass fraction

Abstract in English

An image appearing when the phrase soot is heard is the smoke emitted by an exhaust pipe. The imperfect combustion of hydrocarbon fuels is a source of this harmful pollutant. The industrially controlled combustion of hydrocarbons can provide the carbon black, an industrial product widely used in our everyday life. For both its utilization and its harming effect, the surface of these combustion generated particles plays an important role, therefore, it is of interest to possess information on the particle morphology beside its mass or volume.

Soot particles were found, at various conditions, to have a fractal-like structure built up from spherical shape building blocks, so-called primary particles. This increased interest in the particle surface and its evolution gives the motivation to extend numerical models to provide related information, i.e. particle surface or primary particle size. Furthermore, as the primary particle size influences the chemical and collisional processes, accounting for this parameter can improve the model predictions.

The requirements for numerical models are various depending on the purpose of the simulation. Multidimensional laminar flames, like a laminar coflow diffusion flame, are less complex than flames of industrial combustion systems. However, the soot formation processes are analogous in the two cases, therefore, the investigation of these flames are of interest. In order to obtain a detailed description of the chemical processes, while keeping the computational cost in these flames at an affordable level, using chemical discrete sectional models is a suitable choice. As in their current version, these models do not provide information on the primary particle size their development in this direction is of interest.

Guided by the above motivation, a numerical strategy to determine the primary particle size is presented in the context of the chemical sectional models. The proposed strategy is based on solving the transport equation of the primary particle number density for each considered aggregate section.

In order to validate numerical primary particle size, the comparison to experimental data is required. Due to its numerous advantages, the Time-Resolved Laser-Induced Incandescence (TiRe-LII) technique is a nowadays popular experimental method. However, the comparison of the numerically and the experimen-

tally obtained primary particle size may be charged with uncertainties introduced by the additional measurements or assumptions of the numerous parameters required to derive primary particle size from the detected signal.

In order to improve the validation strategy, an additional approach for primary particle size distribution validation with TiRe-LII is proposed. This is based on the reconstruction of the temporal evolution of incandescence from the numerical results and its comparison with the measured signal. The effectiveness of this 'forward' method is demonstrated *a priori* by quantifying the errors potentially avoided by the new strategy.

The validity of the proposed primary particle tracking model is tested by both the traditional 'inverse' and the 'forward' method on target flames of the International Sooting Flame (ISF) Workshop. In particular a laminar premixed ethylene flame is considered first. Then, two laminar coflow ethylene flames with different dilutions are put under the scope. The sensitivity to the model parameters, such as accounting for the surface rounding and the choice of smallest aggregating particle size, is explored in both the premixed flame and in the coflow flame with highest ethylene content.

To understand the effect of the fuel stream dilution on the primary particle size in the coflow flame, first, the flame-flow interaction and the effect of the dilution on the flame structure is investigated. Then, the correlation between the temperature, the precursor concentrations, the soot volume fraction, and the primary particle diameter is examined. Finally, the formation rates and the residence time along the particle trajectories are studied to understand the effect of dilution on the spatial localization of the biggest particles along the flame.

Résumé français

Les suies de combustion sont principalement connues pour leur caractère nocif, dans le cas des feux de forêt, de fumées de cheminées ou d'émissions polluantes d'un tuyau d'échappement. Cependant, le noir de carbone, un produit industriel de combustion d'hydrocarbures largement utilisé dans notre vie quotidienne.

La surface d'une particule de suies ou de noir de carbon joue un rôle important tant au niveau de son utilisation que de son effet nocif. Il est donc important de connaître la masse, le volume ainsi que la morphologie des suies. En particulier, la surface des particules est un paramètre important pour prédire leur utilisation ainsi que leur effet nocif. Les suies sont généralement des agrégats présentant une structure fractale constituée d'éléments de forme sphérique, appelés particules primaires. Il est possible de connaître la surface des agrégats à partir de la distribution en taille de particules primaires (PPSD-Primary particules size distribution). Compte tenu de l'intérêt grandissant pour la surface des particules et leurs évolutions, il est aujourd'hui nécessaire d'étendre les modèles numériques pour la prévision de la PPSD. De plus, comme la taille des la particules primaires influence les processus chimiques et les processus de collision, la prise en compte de ce paramètre peut améliorer les prévisions des modèles.

Les flammes laminaires multidimensionnelles, comme les flammes de diffusion, sont moins complexes que les flammes rencontrées dans les systèmes de combustion industriels. Cependant, les processus de formation de suies sont analogues dans les deux cas, ce qui rend l'étude de ces flammes intéressante. Afin d'obtenir une description détaillée des processus chimiques ayant lieu dans ces flammes tout en maintenant le coût de calcul à un niveau abordable, l'utilisation de modèles sectionnels discrets chimiques (CDS-chemical discret sectional methods) est un choix approprié. Le développement de modèles CDS est au coeur de cette thèse.

D'abord, une stratégie numérique pour déterminer la taille des particules primaires est présentée dans le contexte des modéles CDS. Elle repose sur la résolution d'une équation de transport pour la densité en nombre de particules primaires pour chaque section d'agrégats considérée. Pour valider la taille des particules primaires déterminée numériquement, les résultats doivent être comparés avec

des données expérimentales obtenues via la technique d'Incandescence Induite par Laser résolue temporellement (TiRe-LII). Cette comparaison, dite inverse, est affectée par les incertitudes expérimentales et les hypothèses sous-jacentes au post-traitement du signal TiRe-LII pour obtenir la PSD. Pour améliorer la stratégie de validation, une nouvelle approche, dite directe, est proposée pour la validation de la PPSD à partir des données obtenues par TiRe-LII. Elle est basée sur la reconstruction numérique de l'évolution temporelle du signal d'incandescence à partir des résultats numériques et de sa comparaison avec le signal mesuré. L'efficacité de l'approche proposée est démontrée a priori en évaluant l'erreur potentiellement évitée par la nouvelle stratégie.

Le modèle proposé pour le suivi des particules primaires est ensuite validé en utilisant à la fois les approches 'directe' et 'inverse' sur les flammes cibles issues de l'International Sooting Flame Workshop (ISF): une flamme pré-mélangée éthylèneair et une flamme de diffusion coflow avec deux dilutions différentes. Le caractère général du modèle est discuté en effectuant une étude de sensibilité des résultats aux paramètres du modèle même. Enfin, le modèle est utilisé pour comprendre l'effet de la dilution du combustible sur la taille des particules primaires dans les flammes de diffusion en examinant les corrélations possibles entre phase gazeuse et phase solide ainsi que l'évolution temporelle des particules le long de leur trajectoires.

Astratto in italiano

Un'immagine che appare quando si sente la fuliggine è legata al fumo che emesso da un tubo di scarico. La combustione imperfetta di combustibili idrocarburici è una fonte di questo inquinante nocivo. La combustione industriale di idrocarburi può fornire il nerofumo, un prodotto industriale ampiamente utilizzato nella nostra vita quotidiana. La superficie delle particelle gioca un ruolo importante sia al suo utilizzo e al suo effetto dannoso, quindi è interessante possedere informazioni sulla morfologia delle particelle accanto alla sua massa o al suo volume. Le particelle di fuliggine sono state trovate, in varie condizioni, per avere una struttura simile a un frattale costruita da blocchi di forma sferica, le cosiddette particelle primarie. Questo accresciuto interesse per la superficie delle particelle e la sua evoluzione dà la motivazione di estendere i modelli numerici per fornire informazioni correlate. Inoltre, poiché la dimensione delle particelle primarie influenza i processi chimici e collisionali, tenere conto di questo parametro può migliorare le previsioni del modello. I requisiti per i modelli numerici sono diversi a seconda dello scopo della simulazione. Le fiamme laminari multidimensionali, come una fiamma di diffusione a coflow laminare, sono meno complesse delle fiamme dei sistemi di combustione industriale, tuttavia i processi di formazione di fuliggine sono analoghi nei due casi, pertanto l'indagine su queste fiamme è interessante. Al fine di ottenere una descrizione dettagliata dei processi chimici, mantenendo il costo computazionale in queste fiamme a un livello accessibile, l'uso di modelli di sezione chimica discreta è una scelta adatta. Come nella loro versione attuale, questi modelli non forniscono informazioni sulla distribuzione delle dimensioni delle particelle primarie (PPSD), il loro sviluppo in questa direzione è di interesse.

Guidato dalla motivazione di cui sopra, una strategia numerica per determinare la dimensione delle particelle primarie viene presentata nel contesto dei modelli di sezione chimica. La strategia proposta si basa sulla risoluzione dell'equazione di trasporto della densità del numero di particelle primarie per ciascuna sezione aggregata considerata. Per convalidare la dimensione numerica delle particelle primarie, è necessario il confronto con i dati sperimentali. Grazie ai suoi numerosi vantaggi, la tecnica Incandescenza Laser-Indotta Risolta nel Tempo (TiRe-

LII) è un metodo sperimentale popolare al giorno d'oggi. Tuttavia, il confronto delle dimensioni delle particelle primarie numerici e sperimentali può essere caricato con incertezze introdotte dalle misure addizionali o dalle ipotesi necessarie per derivare la dimensione delle particelle primarie dal segnale rilevato.

Per migliorare la strategia di convalida, viene proposto un approccio aggiuntivo per la convalida PPSD con TIRE-LII. Questo si basa sulla ricostruzione dell'evoluzione temporale dell'incandescenza dai risultati numerici e dal suo confronto con il segnale misurato. L'efficacia di questo approccio avanzato è dimostrata a priori quantificando gli errori potenzialmente evitati dalla nuova strategia.

La validità del modello di tracciamento delle particelle primarie proposto, sia con il metodo tradizionale e con metodo avanzato, è testata sulle fiamme bersaglio del Workshop Internazionale Fiamma Fuligginosa (ISF). In particolare, una fiamma di etilene premiscelata laminare è considerata prima. Quindi, due fiamme laminari di etilene con diverse diluizioni vengono poste sotto lo scopo. La sensibilità ai parametri del modello viene esplorata sia nella fiamma premiscelata che nella fiamma coflow con il più alto contenuto di etilene.

Per comprendere l'effetto della diluizione del flusso di carburante sulla dimensione delle particelle primarie nella fiamma del coflow, prima viene esaminata l'interazione del flusso di fiamma e l'effetto della diluizione sulla struttura della fiamma. Quindi, viene esaminata la correlazione tra la temperatura, le concentrazioni dei precursori, la frazione di volume di fuliggine e il diametro delle particelle primarie. Infine, i tassi di formazione e il tempo di permanenza lungo le traiettorie delle particelle sono studiati per comprendere l'effetto della diluizione sulla localizzazione spaziale delle particelle più grandi lungo la fiamma.

CHAPTER 1

Introduction

The following chapter first describes the motivation behind investigating the formation and the structure of the hydrocarbon combustion generated particles. The utilization and the negative effects of airborne particles containing elemental carbon (EC) are discussed, in which the surface of the particles, therefore the size of their main building blocks (the primary particles), plays an important role. Then, the formation processes and the morphology of these particles are discussed, with a special focus on the nature of the primary particles. Briefly, the advantages of calculating the primary particle size and investigating laminar coflow diffusion flames are presented. This is followed by a short outlook on the currently available validation methods of numerical primary particle size by measurements. Finally, the scope of the work is presented.

1.1 Motivation

1.1.1 The negative effects of soot

Soot is the undesired byproduct of the combustion. Entering the atmosphere, soot particles join the company of aerosols affecting both the climate and the human health. Atmospheric aerosols have highly variable chemical composition and size distribution [1]. This is due to the various sources of the particle formation processes resulting in both relatively large inorganic aerosols (usually larger than $1\,\mu\mathrm{m}$) and nanoscale organic or solid black carbon, particles. The former can originate from volcanoes, sea spray or mineral dust, whereas the latter is typically the result of human activities, like combustion processes, biomass burning, transportation on land, water and air or energy production by fossil fuel, coal and biomass combustion [2].

An anthropogenic light-absorbing aerosol, like soot - or black carbon, as climate modelers call nowadays combustion-related carbonaceous aerosols that are strongly light-adsorbing [3]-, absorbs the incoming sunlight, thereby directly warming the atmosphere and cooling the surface [4]. The indirect warming effect is related firstly to the reduced cloud and rain formation, secondly, to the longer lifetime and higher reflectivity of clouds, which increases the Earth's albedo [4]. The perturbation of rainfall and cloud formation highly impacts the Earth's thermodynamic balance, which drives the weather and the climate. In the last years, this strong climatic effects of various aerosols have been widely investigated [4–6].

This indirect warming is faced also when soot is deposited on snow. The effect on the snow albedo, i.e. the albedo of the surface covered by snow, was investigated by several researchers [7–10]. The climate forcing due to the albedo change of snow and ice caused by soot can be twice as "effective" as CO_2 in altering the global surface air temperature [9]. Measurements performed on snow crystal in Sapporo, Japan in the 1970s [11] revealed thousands of aerosols, including soot, contaminating the probed sample. Though in central Antarctica, snow crystals were contaminated only by 25-50 aerosols in 1969 [12], it still indicated a high collection efficiency of snow, which can be related to the electrostatic attraction, the thermophoresis (temperature gradient between snowflake and environment), and the diffusiophoresis (vapor pressure gradient between snowflake and environment) [12]. A 100 ppbw concentration of black carbon is enough to double the absorption of sunlight and reduce the visible albedo by 10%, based on the measurements performed in the Alps by Sergent et al. [13]. However, due to the positive feedbacks, i.e. the melting of snow further decreases the albedo resulting in an increased solar energy absorption, a smaller amount of black carbon can already lead to the perturbation of snowmelt.

To indicate the temperature increase over the past years, the annual mean response of the surface air temperature (T_s) observed between 1880 and 2002 by Hansen et al. [14] is shown in Figure 1.1. The temperature increased during the two decades in most areas, except a small region around the southern pole. This may be related to the reduction of surface albedo caused by the black-carbon contamination [9, 15].

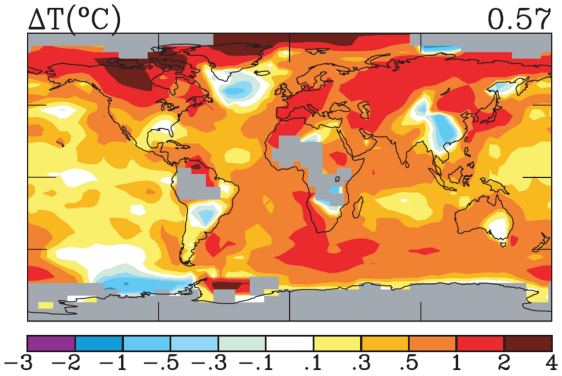

Figure 1.1: *Annual mean response of surface air temperature, reprinted from [9]*

Atmospheric aerosols do not contribute only to climate change, but represent a serious danger for the health. The inhaled particles penetrate to different depths of the respiratory system depending on their size (Figure 1.2). While the particles with a dimension less than $10\,\mu\mathrm{m}$ (PM10) reach only the nose or the mouth, the particles with a dimension less than $2.5\,\mu\mathrm{m}$ penetrate beyond the terminal bronchioles into the gas-exchange region of the lung [16, 17].

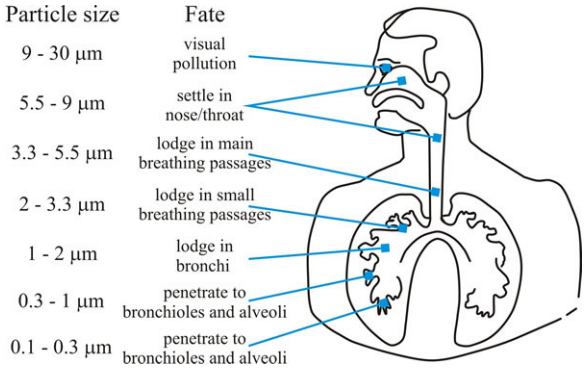

Figure 1.2: *Particle size-dependent penetration depth into the respiratory system [17]*

A recent report of the WHO's (World Health Organization) cancer research agency [18] declared the outdoor air pollution and particulate matter as human carcinogens based on the connection found by the International Agency for Research on Cancer (IARC) between their levels in the air and the cancer risks. More than 1000 scientific studies were included in this research. Combustion-related aerosols emitted into the atmosphere can cause also enhanced respiratory, cardiovascular, infectious, and allergic diseases [5]. Krzyzanowski et al. [19] concluded that combustion-related particles contribute to an increased risk of death, particularly from cardiopulmonary causes. Nanoparticles can also enter the blood stream via inhalation or ingestion and be transported around the body and taken up by organs and tissues, where they cumulate in time causing serious damage [18]. The overload of the body's phagocytes, cells that ingest and destroy foreign matter, can trigger stress reactions that lead to inflammation. Despite small particles do not represent a significant mass of the total soot amount, they are the most toxic ones [18].

All above-listed health and climate-related processes depend not only on the number of particles and their total mass, but mainly on their size and, in particular, on their surface [20]. In general, soot can be formed in various ways as mentioned before, however, in the current work the focus will be on the byproduct of the imperfect combustion of hydrocarbon fuels.

1.1.2 Utilization of carbon black

Fortunately, the byproduct of combustion can also serve us. The first plant producing carbon black, "lampblack" as it was called at that time, was opened in the United States in the 1740s. The name used nowadays (carbon black) was originally a generic name for all goods manufactured from natural gas in the 1870s.

The carbon black is produced inside large furnaces by the combustion of fos-

sil fuels, both in liquid or gas phase, in the excess of fuel. The particle size and morphology can be manipulated by the fuel/oxygen ratio as the internal temperature of the furnace is adjusted. To ensure the good quality of the reinforcing fillet in tires and mechanical rubber or the color pigment in plastics, paints, and inks a high surface to volume ratio is required. Therefore, the particle size and morphology are of high importance in the production of these goods of our everyday life.

The combustion in these cases is performed under well controlled conditions and optimized to maintain specific parameters of the end product, which results in very different characteristics compared to soot [21, 22]. These products are composed mainly of elementary carbon arranged as aciniform particulate with low amount of contamination [23]. On the contrary soot may have a relatively low amount of carbon ($<$60% of the total particle mass) and contains a significant amount of ash and solvent extractable fraction [21]. Only particulates produced by diesel engines tend to show aciniform morphology. However, the chemical processes forming both types of materials originating from the hydrocarbon combustion (carbon black and soot) are the same and the surface area of the particles depends on their morphology which is defined by the history of the particle.

1.2 Soot formation

The formation of soot particles in combustion processes is a very complex phenomenon, controlled by numerous parameters, like the temperature, the pressure and the chemical composition of the gas along the pathway of the formed soot particle. The residence time of the soot particle in the various regions is also of high importance, consequently, the flow field plays a significant role.

A general assumption [24] is that first a multitude of small particles are formed in the flame. Second, their growth by the sediment of gaseous species or by collision results in larger particles that solidify later on. Finally, the collision of the solidified particles produces aggregates. These can grow larger by further aggregation, condensation or surface growth. Oxidation, which reduces the mass of soot, is in competition with the previous processes. The Transmission Electron Microscopy (TEM) images in Figure 1.3 were taken in a coflow flame [25], the observed particle evolution with the residence time and therefore with the height above burner (HAB) is in agreement with the general assumption of soot evolution described above.

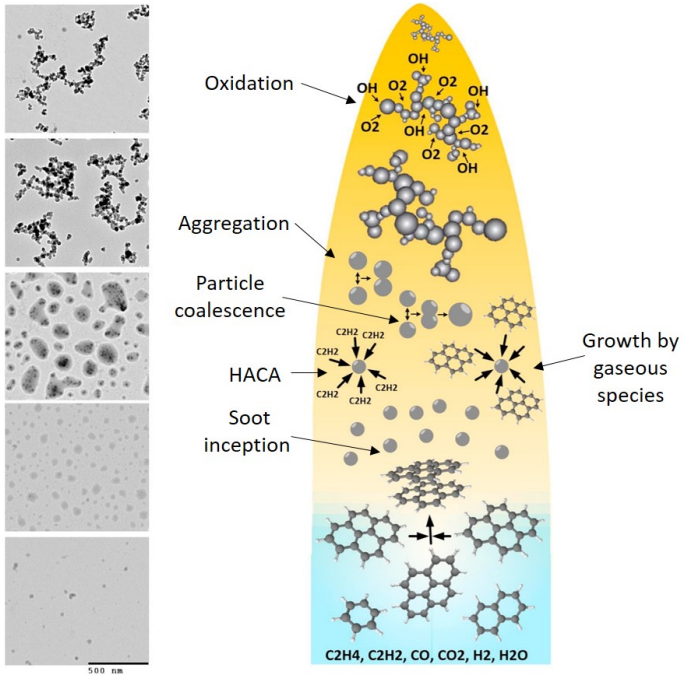

Figure 1.3: *Soot particle formation and evolution. Left: TEM images taken along the centerline of a laminar coflow flame [25]. Right: illustration of soot formation and evolution. Images are reprinted from [26].*

The below-listed processes, visualized in Figure 1.3 according to the illustration presented by Kholghy et al. [26], are usually considered in the evolution of a soot particle:

- Soot inception: formation of a soot particle from gas-phase species
- Hydrogen-Abstraction C_2H_2-Addition Mechanism (HACA): removal of a hydrogen atom and a consequent addition of acetylene
- Growth by gaseous species: the sediment of gaseous species on the particle surface, where these species may be of the following types [27]:
  - Polycyclic Aromatic Hydrocarbon (PAH)
  - Large Molecular Weight PAHs, so-called Heavy PAHs
  - Resonance Stabilized Radicals (RR)
- Particle coalescence: the collision of particles and their consequent merging (particles do not keep their original shape)
- Aggregation: the collision of particles without a consequent merging (particles do keep their original shape)
- Oxidation: removal of mass from soot particle by O, OH, and O_2

The characteristics and the formation of nascent soot particles were intensively studied by several research groups around the world: at Universitá degli Studi di

Napoli Federico II [28–31], at Brown University [32–34], at University of Southern California [35–38] and at Université de Lille [39–41]. It was found that small radicals of the gas-phase generate larger hydrocarbon radicals and polycyclic aromatic hydrocarbons (PAHs). These are known to be precursors of soot formation, as PAH stacking and molecular growth of aromatic compounds are the controlling steps of soot particle formation [27, 29, 36, 42–47].

The transitions from gas-phase species, to liquid-like nanoparticles and finally to mature, solid particles, are not precisely connected to a given size and is still under investigation. Nascent soot particles (with a size of few nm) have a liquid-like behavior [32, 34, 36, 48, 49], therefore they coalesce upon collision. They are characterized by a spherical shape [32, 34, 36, 48, 49], low visible absorption and semi-transparency to an electron beam [25, 50]. The latter makes it hard to detect them by several experimental techniques.

The nascent particles are generally considered to be constructed of large molecular weight "heavy PAHs" linked together by aliphatic bridges [36], and featured more by aromatic than aliphatic character [48, 51, 52]. Consequently, their chemical composition is characterized by a high H/C ratio (0.6-0.25). This decreases with the residence time and consequently with the maturity [53–55]. This decrement of hydrogenation level also means the decline of the ratio between the aliphatic and aromatic H atoms. Nevertheless, they may also contain oxygenated species [35, 51, 52, 56].

The incipient particles grow further by the surface addition and by the coalescence, reaching a size up to 10-60 nm [32, 36, 57, 58]. Hydrogen loss leads to a more graphitic structure. The mature, hardened soot particles do not coalesce but stick to each other keeping their original shape and forming aggregates [29, 34]. The comparison by Mitchell et al. [59, 60] between the particle structure obtained numerically and the experimentally observed particle shapes indicated that aggregation and nucleation are not separated in time, but can coexist. The size of the aggregates increases further on by the coagulation and by the growth via gas-phase compounds addition, like the Hydrogen-Abstraction C_2H_2-Addition Mechanism (HACA) [61] and the growth by Resonance Stabilized Radicals (RR) [62, 63] or PAHs.

The competing process with above-described soot growth is the oxidation by OH• and O• radicals and O_2, which were observed by several researchers [49, 64–68]. It was found that in fuel lean conditions soot aggregates or particles tend to be oxidized more by the O_2, whereas in more fuel rich conditions the oxidizing species is the OH [69]. The oxidation weakens the particle structure, which can lead to its fragmentation, i.e. break up into smaller particles. Fragmentation was first observed by Neoh et al. [69], and later on similar observations were made by Echavarria et al. [66] and Garo et al. [70].

1.3 Soot morphology and primary particle size distribution

Since soot particles are the result of the previously mentioned local chemical and collisional processes, the particle population can show various sizes and morphologies [24, 71–73]. From the TEM images of soot particles presented in Fig-

ure 1.3 it can be observed that small, nascent particles formed in the lower region of the flame tend to have a spherical shape. On the contrary, as the residence time increases, aggregation takes place and fractal-like structures appear.

Despite particle mass can vary on a wide range, the particles show a similar, fractal like structure on a wide range of conditions: laminar premixed [38,53–55, 74,75], laminar diffusion [25,76,77] and turbulent flames [78–80]. These mature, fractal-like particles are composed of small, quasi-spherical building blocks of diameter d_{pp}, which are called primary particles (See Figure 1.4).

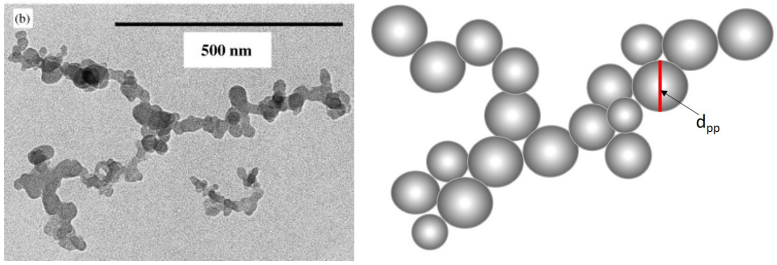

Figure 1.4: *Left: TEM picture of soot aggregate [81]. Right: schematic representation of aggregate highlighting the primary particle diameter.*

An example [82] of dependency on the fuel type and the temperature for the primary particle diameter is summarized in Table 1.1. With the change of fuel type, the mean diameter at similar heights for the same type of flame (laminar diffusion flame) varied between $\sim$14 to $\sim$60 nm. Examples of the primary particle size distribution (PPSDs) and the mean primary particle diameters in a laminar diffusion flame obtained by TEM [77] are presented in Figure 1.5, where the "wing" indicates the middle, circumferential part of the flame where the soot volume fraction is outstandingly high. On the centerline, the distribution is narrow, almost monodisperse, but the mean value changes with the height above burner (HAB). On the "wing" the mean values are larger than at the centerline, and the distribution is wider, primary particles with diameter 5 and 50 nm coexist. These results indicate, that the primary particle size depends significantly not only on the fuel type but also on the probe location. Furthermore, at a certain location, the distribution can be highly polydisperse. In general, the primary particle diameters vary between 10 to 60 nm, with standard deviations of 5 - 25 nm [77, 82–84].

Table 1.1: *Primary particle size for different fuels in gas-jet laminar diffusion flames [82]*

Fuel	Flow rate [sccm]	Axial height [mm]	d_{pp} [nm]	Temperature [K]
Methane	350	50	14.2 ± 1.5	1750
Ethane	255	61	20.4 ± 1.9	1700
Ehtylene	231	50	33.3 ± 3.2	1600
Acetylene	200	50	59.7 ± 3.9	1200

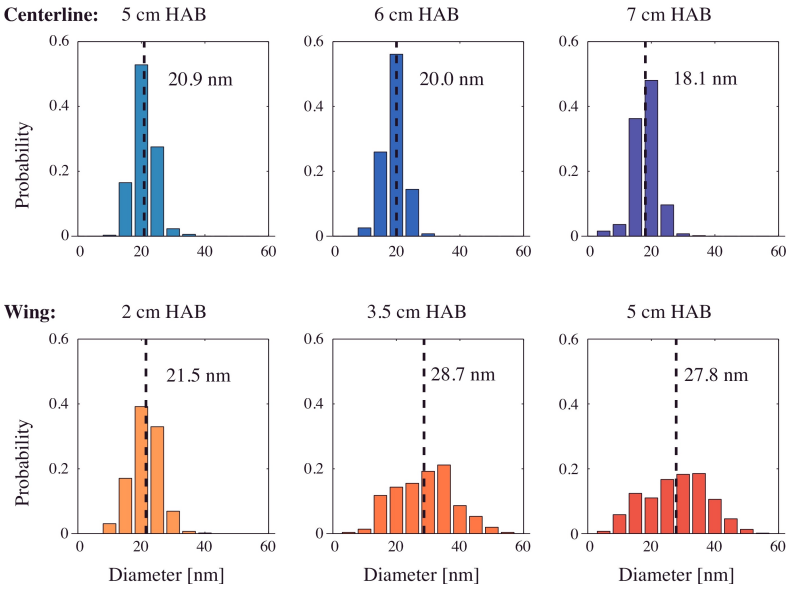

Figure 1.5: *Primary particle size distribution for various HABs in a coflow diffusion ethylene flame (dashed lines indicate the mean value), reprinted from [77]*

Though in many conditions the primary particle size distribution was found to be lognormal [77, 85, 86], it has been also shown that this cannot be considered as a general rule [25, 77, 87–90]. A counterexample is the PPSD at HAB = 5 cm on the "wing" in Figure 1.5.

From numerical simulations, performed by Mitchell et al. [60] to investigate the evolution of the soot particle shape through soot aggregation and surface growth, it was concluded that the two main factors influencing the final shape of the soot particles are the speed of surface growth rate and the colliding primary particle size. These have the following impacts: 1) the surface growth smoothens the particle surface; 2) the smaller size of colliding primary particles (therefore smaller constructing particles of the aggregate) are more probable to result in spheroidal particles, as they are easier the be covered by surface growth processes.

The numerical determination of the particle structure is of high interest for various reasons. First of all, as it was highlighted in Sections 1.1.2 and 1.1.1, the surface of the particles is an important factor for the intensity of the harming effect of this pollutant and at the utilization of black carbon. Once the volume V of one aggregate and d_{pp} are known, and point-contact is assumed between the primary particles in the aggregate, the surface area can been obtained as:

$$S = 6V d_{pp}^{-1} \tag{1.1}$$

Secondly, the interaction between soot particles is influenced by the collision efficiency [27, 60, 91], therefore by the collision diameter (d_c) of the soot particle, which depends on the particle morphology [27] as:

$$d_c = \sqrt{5/3} \cdot d_{pp} \left(\frac{n_p}{k_0} \right)^{1/D_f} \tag{1.2}$$

where D_f is the fractal dimension, n_p is the number of primary particles in the aggregate and k_0 is the scaling prefactor.

Finally, frequently the measurements do not provide the particle mass, but the radius of gyration (R_g defined by Eq. 1.3 [76]) [92–95] or the mobility diameter (d_m) [75, 96–99], which cannot be derived from the particle mass unless information about its morphology is available:

$$R_g = 0.5 \cdot d_{pp} \left(\frac{n_p}{k_0} \right)^{1/D_f} \tag{1.3}$$

Even if the access to the morphological information is granted, several relations between the mobility diameter and the particle characteristics can be found in the literature [38, 100]. Two examples of them are:

$$d_m = 1.624 \cdot d_{pp} k_0^{-1/D_f} D_f^{-0.9} n_p^{0.47} \tag{1.4}$$

$$d_m = d_{pp} n_p^{0.46} \tag{1.5}$$

For these reasons, the knowledge of primary particle size is required both to properly calculate the collision efficiency and to perform validation with experimental data in terms of the gyration or the mobility diameter. It has to be noticed that for particles with spherical shape (i.e. n_p = 1), which is generally characteristic for small, nascent particles, the diameters, R_g, d_m and d_pp agree.

1.4 Soot investigation

Despite the importance of the soot particle surface, numerical and experimental tools for the characterization of this key quantity still have to be improved. This is mainly due to the complexity of the problem, since soot particles are the result of numerous local chemical and collisional processes resulting in a population of particles of various size and morphology [24, 71–73].

Formerly, most of the numerical models were limited to predict exclusively the particle size distribution (PSD) [45, 101–106], which provides information on the mass or the volume of the particles, but not on their primary particles and their surface. Modeling the primary particle size is a challenging and computationally expensive task. However, the inclusion of primary particle size tracking in numerical models has numerous advantages. Firstly, the comparison of the numerical and experimental primary particle size provides a new aspect for model validation. Secondly, the primary particle size determines the surface, which influences the rate of surface related processes like oxidation or surface growth, and the collision frequency, i.e. how frequently the particles collide and have the possibility to interact. Therefore, properly accounting for the primary particle size is expected to improve the model's prediction capability.

Recently, some numerical methods were extended and used to provide information about the primary particle diameter (d_pp). Some of these models provide a very detailed description of the soot morphology. However, due to their computational cost, they are applicable only in zero or one-dimensional simulations [59, 60, 107–110]. Some models can be used on complex geometries

or flames (multidimensional and/or turbulent) thanks to their low computational cost, however, they do not provide information about the primary particle size distribution, but only the mean d_{pp} [91, 111–118]. Multidimensional laminar flames, like a laminar coflow diffusion flame, are less complex than flames of industrial combustion systems. However, the soot formation processes are analogous in the two cases, therefore, the investigation of these flames are of interest. Numerical studies with primary particle size distribution of experimentally investigated multidimensional laminar flames were presented only in 2019 for a coflow diffusion flame [119].

To validate the numerically obtained PPSD, the comparison to experimental PPSD is required. Formerly, the Transmission Electron Microscope (TEM) analysis of thermophoretically sampled soot have been extensively applied to determine the d_{pp} and the PPSD. Nowadays a more and more widespread technique is the Time-Resolved Laser-Induced Incandescence (TiRe-LII) due to its numerous advantages, like the applicability in high-pressure conditions and the high temporal and spatial resolution. Furthermore, using this technique, one does not have to fear that the probe gets clogged or the flow is disturbed. However, at the TiRe-LII measurements, the d_{pp} and the PPSD are not directly measured so that post-processing is needed, which requires various input parameters beside the LII signal decay. Most of these quantities are also not directly measured which further complexifies the determination of the PPSD and the d_{pp}. The uncertainties of this method may undermine the numerical model validation with the TiRe-LII.

1.5 Scope of work

In this work, the first goal is to provide an extension for the chemical discrete sectional models (CDSMs), which are computationally affordable in multidimensional laminar flames while ensuring a detailed description on the soot formation processes, to obtain information on the primary particle size. The second goal is to investigate the performance of an available CDSM combined with the proposed methodology. For this also the improvement of the validation strategy with TiRe-LII is targeted. Finally, by using the combined model, a deeper understanding of the primary particle size evolution and the effect of dilution in a laminar coflow flames is aimed at.

In order to make it possible to predict primary particle size with CDSMs, a new variable, the primary particle number density, will be introduced and its transport equation will be derived. Based on the author's knowledge, no attempts were made earlier to extend CDSM to calculate primary particle size. The proposed primary particle tracking model will then be incorporated in the CDSM model of the CRECK Modeling Group [27].

To improve the validation by the TiRe-LII, a novel strategy to validate the numerical models based on the reconstruction of the LII signal from the numerical simulation will be proposed. The goal with this forward strategy is to take advantage from the experimentally not or hardly determinable variables and parameters available in the numerical simulations. The interest in the suggested approach will be investigated *a priori* by quantifying the potential errors that can

be avoided with this new strategy. For this, a code to simulate the incandescence signal is created based on the work of Hofmann et al. [120] and Liu et al. [121, 122].

The validation of the extended CDSM model will be performed both by the traditional and by the newly proposed approaches on a premixed laminar flame and on a series of coflow laminar diffusion flames, benchmark flames of the International Sooting Flame (ISF) Workshop [123]. After validation, the influence of dilution on the primary particle size in the laminar coflow flame will be put under the scope using the knowledge gained about the soot formation processes by a CDSM. The flames simulated with the combined model are the third premixed ISF target flame (ISF-premixed-laminar-3) and the full series of the third laminar ISF target coflow flames (ISF-coflow-laminar-3). Latter includes the variation of the ethylene/nitrogen volume content in the fuel stream: 32% (F32), 40% (F40), 60% (F60) and 80% (F80).

The Thesis is organized as follows. First, an overview of the available soot models is provided in Chapter 2. Then, in Chapter 3, the general primary particle tracking model for CDSM is presented. The novel variable, the primary particle number density, and the related transport equations are introduced. Its incorporation into the CRECK Modeling Group's CDSM is explained.

In Chapter 4, the experimental methods generally used to obtain d_{pp} and PPSD are presented first, by focusing on the TiRe-LII measurement technique. Then, the concept of numerical PPSD validation with the direct comparison of the incandescence signal is explained, and examples for other variable validations by directly comparing the detected signal to the numerically synthesized signals are provided. The incandescence signal model used in this work is described, and, finally, the errors that are potentially introduced by the post-processing of the TiRe-LII signal to obtain the PPSD are quantified by reviewing results from the literature and by reporting additional error evaluations.

For the model validation, first the premixed flame is discussed in Chapter 5, where, after the flame configuration and the numerical setup is outlined, the numerical results are presented. The numerical soot volume fraction and the mean primary particle size are compared to the experimental results for validation, along with a discussion on the sensitivity to the model and evaluation parameters. Furthermore, the impact of the imposed temperature is examined. Finally, the novel validation approach is used and further conclusions about the numerical PPSD validity are drawn.

The coflow flame series is discussed in Chapter 6. First, the configuration and the numerical setup is presented. Then, the comparison of numerical and experimental temperature and soot volume fraction is presented for validation. The sensitivity of the primary particle size to the evaluation and model parameters is investigated. The agreement with the experimental data based on both the traditional and the novel approach is discussed. Finally, the effect of dilution on the flame structure, the soot formation processes, and the primary particle size is debated.

Conclusions and future directions are summarized in Chapter 7.

CHAPTER 2

Soot formation modeling

In the following chapter the nowadays most popular numerical approaches to model the formation of soot particles will be presented, with a special focus on the chemical discrete sectional model proposed by the CRECK Modeling Group [124], which will be used in this work for the flame simulations.

The objective of soot formation modeling is two twofold. On the one side, it helps the understanding of this very complex process, on the other side, it can be used at design purposes: either to avoid the formation of the pollutant or to enhance the yield of the black carbon production. The requirements and the expectations imposed on the model performances are therefore various. While the fundamental research aims to provide a detailed description, which is associated with high computational costs, the industrial applications require a model computationally affordable on complex geometries even if fewer details are captured.

Some of the numerical soot models, like the Method of Moments (MOM) and the Aerosol Discrete Sectional Model (ADSM), consider hydrocarbon molecules up from nucleation as a multitude with distribution in respect to certain parameters. The models provide alternative techniques to solve the Population Balance Equation (PBE), a continuity statement of the soot particles Number Density Function (NDF: $f(t, \bar{x}, \bar{\xi})$) [125, 126]. The variables of the NDF are the external coordinates ($\bar{x}$), the time (t) and the internal coordinates (ξ). ξ contains the characteristic parameters used to describe the soot particle, such as the particle mass, the particle surface or the hydrogenation level. The NDF defines the number of particles disposing of a certain set of parameters. In case only the particle size, i.e. the particle volume ($\xi = V_p$) or the particle mass ($\xi = m_p$), is considered, this simplifies to the particle size distribution (PSD). The transport equation below describes the evolution of the soot particles' NDF:

$$\frac{\partial f(t,\bar{x},\bar{\xi})}{\partial t} + \frac{\partial}{\partial \bar{x}_i}\left(v_i \cdot f(t,\bar{x},\bar{\xi})\right) - \frac{\partial}{\partial \bar{x}_i} D_x \left(\frac{\partial f(t,\bar{x},\bar{\xi})}{\partial \bar{x}_i}\right) = S_\xi(t,\bar{x},\bar{\xi}) \quad (2.1)$$

with D_x being the diffusion coefficient and S_ξ the source term.

Another approach is to consider soot as the sum of hydrocarbon species and treat their interactions as chemical reactions. However, due to the very high number of species potentially required to describe soot, it is a common approach to split the molecular mass range into sections and represent the species belonging to the same section with one speudo-specie, as done by the Chemical Discrete Sectional Model (CDSM).

Alternatively, the evolution of the soot particles can be treated in a statistical way like the Monte Carlo (MC) approach.

2.1 Method of Moments

The use of the method of moments for soot formation modeling was originally suggested by Frenklach et al. [127] and it is based on the transport of the moments of the NDF function. In principle, the distribution function can be reconstructed if all (integer) moments are known. However, in practical cases the first few moments provide enough information to obtain the sought properties of the distribution [45], therefore, the computational costs can be kept low. Since its first utilization to compute soot mass fraction, an impressive body of work was provided by Frenklach and coworkers [45, 127–132] investigating various aspects for premixed flames.

In the MOM, the set of equations is solved for the integer moments, therefore, a bottleneck of the approach is the determination of fractional moments, which appear in the source terms of the reformulated PBE. These fractional moments originate from the surface dependency of certain process, as the oxidation or the HACA mechanism.

Frenklach et al. [45] obtained these fractional moments by interpolating between the integer moments in the framework of the model called Method of Moments with Interpolative Closure (MOMIC). Another approach to obtain the fractional moments is to approximate the moments by a quadrature integral of the number density function [133]. Marchisio et al. [125] proposed a Dirac-delta kernel function (Direct Quadrature Method of Moments (DQMOM)), and later on, the approximation was obtained by gamma and log-normal kernel functions resulting in the Extended Quadrature Method of Moments (EQMOM) and the Ln-EQMOM, respectively [134]. In these approaches, the equations are solved directly for the weights and for the abscissas of the kernel functions describing the NDF. The quadrature MOM simulations provide a better description of the NDF. However, the computational effort increases due to the higher number of variables.

The univariate model lacks the possibility to recover information about the particle morphology or the primary particles since the particles are considered to be spherical. With the introduction of further variables the description becomes

more accurate, however, the computational cost of these multivariate or quasi-multivariate models is higher. MOMIC was extended by a bivariate description by Mueller et al. [91]. The new PBEs are written in terms of mixed, bivariate moments and the surface dependency of the formation processes is taken into account. Unfortunately, in the work of Roy et al. [135], it was revealed that information on smaller particles is lost, hence negative order moments are not well predicted. Furthermore, this method can lead to oscillations.

An improved version of this model was proposed in [111] by adding a delta function to the interpolation in order to keep in track the effect of the small particles. The coordinates for the delta function are fixed for the properties of the smallest soot particle. The source terms are expressed by the coordinates and weights. Furthermore, using a first order interpolation and the wise choice of moments simplifies the moment transport equations to a linear equation system. A later study of Mueller et al. [136] extended the model to include oxidation induced fragmentation, and the novel model was validated on a series of laminar premixed methane flames and a laminar counterflow diffusion acetylene flame.

Further methods were developed, taking as a basis the above-described ideas. The Conditional Quadrature Method of Moments (CQMOM) by Yuan et al. [112, 113] handles the bivariate nature of the problem with a numerically robust way by conditioning the second internal coordinate with the first one. This simplifies the bivariate moment inversion problem to two consecutive quasi-univariate inversions. The benefit of bivariate description and computational robustness due to conditioning was combined with the kernel function from EQMOM, resulting in the so-called Extended Conditioned Quadrature Method of Moments, presented by Salenbauch et al. [116].

The intensity of the HACA surface reactions depends on the active sites of the soot particle surface. Blanquart et al. [114, 115] extended the DQMOM to a trivariate version which considers, not only the volume and the surface, but also the number of the hydrogenated carbon sites. The resultant soot volume fraction had good agreement with experiments, but the surface reactivity led to contradictions, asking for further investigation.

This family of modeling methods [114, 136–140] were applied on premixed laminar flames [114–117], on counterflow and coflow flames [114, 115] and turbulent flames [118, 139] to investigate primary particle size, but providing only the mean value of d_{pp}.

2.2 Sectional models

Alternative approaches for soot prediction are the sectional soot models. Based on the way of treating the soot particle interactions, aerosol dynamics or chemical reactions, two types of sectional models can be distinguished: the ADSM and the CDSM respectively. For both, the mass spectrum of soot particles is divided into discrete sections, each with a representative particle mass (ADSM) or species (CDSM). To improve the detail of description in certain models, subclasses are defined, e.g. for the hydrogenation level and/or particle surface. The transport equations are solved for these classes' particle number or species mass fraction or

molar concentration.

2.2.1 Aerosol Discrete Sectional Model (ADSM)

In ADSM, soot is considered as a population of aerosol particles whose evolution is governed by the PBE [141–143]. The PBE is the Smoluchowski coagulation equation extended to account for surface growth and oxidation.

$$\frac{\partial f(t,V_p)}{\partial t} + \frac{\partial}{\partial V_p}\Big(I_{Sg}(V_p)\cdot f(t,V_p)\Big) + \frac{\partial}{\partial V_p}\Big(I_{ox}(V_p)\cdot f(t,V_p)\Big) = \\ 0.5\int_0^{V_p}\beta(V_p-\hat{V}_p,\hat{V}_p)f(t,V_p-\hat{V}_p)\mathrm{d}\hat{V}_p \\ -f(t,\hat{V}_p)\int_0^{\infty}\beta(V_p,\hat{V}_p)f(t,\hat{V}_p)\mathrm{d}\hat{V}_p + S_{nuc}(t,V_p) \tag{2.2}$$

where I_{Sg} is the surface growth rate, I_{ox} is the oxidation rate, $\beta(V_{\mathrm{p}},\hat{V}_{\mathrm{p}})$ is the collision kernel for two particles of volume V_{p} and $\hat{V}_{\mathrm{p}}$, and S_{nuc} is the nucleation rate.

By dividing the size range of the particles into sections, the evaluation of double integral in the coagulation kernel is not required. The additional source term describing the nucleation is included for the smallest section only. The nuclei are usually considered to be formed by the coalescence of two dimers [91] and it is generally assumed that the inception is limited by the formation rates of certain PAHs. The formation rate of these PAHs are estimated by using a steady-state expression, which depends on some lower carbon number species concentrations [144, 145].

The surface growth and the oxidation are modeled by assigning the growing and shrinking particles to new sections while keeping the same total number and volume (or other moments) of the new particles. The numerical diffusion caused by considering only the number and the volume ("two-point" method) can be reduced by using a "three point" method, i.e. considering an additional moment (V^2), when assigning to the sections the particles resulted by the growth or shrinking processes [143]. The numerical diffusion can be eliminated by introducing moving-sections [146, 147], where particles do not move to higher sections as a result of surface growth, but the section boundaries are modified. As for numerical reasons the section boundaries have to be identical in spatially inhomogeneous cases, this method is practically applicable only in zero-dimensional, i.e. mainly in plug flow reactor, simulations [148].

For modeling the aggregate nature of the particles, a two-equation per section model was proposed by Park et al. [148]. A new variable, the number concentration of total primary particles, was introduced for each section so that the average number of primary particles in an aggregate for each section could be calculated. This also improved the accuracy of the collision cross-section. Further bivariate models are available in the literature, which either track the particle surface [149] or the primary particle number [105, 150] for each section. For both options, similarly to the one of Park et al. [143, 148], it is assumed that the primary particle

size in a mass section is identical.

Additionally, multiple subsections per mass section can be considered to account for the polydispersed character of d_{pp} in aggregates of a given size, as done by Nakaso et al. [151] for titania nano-particles. However, the associated computational cost is too high for multi-dimensional problems.

An alternative way to predict the primary particle size with the aerosol sectional model is to presume a volume-surface relation. However, it should be noticed that the proposed volume-surface law in [152] is not general. In addition, it can be shown that the retained law implicitly models aggregates as composed by primary particles with a given constant diameter, corresponding to the diameter of the biggest spherical particles allowed by this law itself.

2.2.2 Chemical Discrete Sectional Model (CDSM)

Several chemical sectional soot models were developed and used for soot formation modeling in the last decade [27, 30, 46, 47, 104, 153–156]. These models may differ in the spacing and limits of the mass spectra division, the considered chemical pathways, the reaction constants and the type of subsections. Some of them distinguish between species of the same mass section but different H/C ratio (level of dehydrogenation) [27, 155] or morphology [47]. This expansion of the mechanism with subsection provides more information and an improved description, however, also increases the computational cost.

The interactions between two representative species of the soot sections (BINs) or a BIN and a gaseous species are described by chemical reactions, and the reaction rates are expressed through the Arrhenius' equation with the collision frequency derived from the kinetic theory. Assuming elementary reactions may not be valid to all inter-particle interactions. However, this is a general approach at CDSM.

The kinetic constants are derived from reference reactions of gas-phase species, using analogy and similarity rules, and are usually similar if they belong to the same type of formation, destruction or graphitization processes: soot inception, Hydrogen-Abstraction-Carbon-Addition (HACA), surface growth, PAH condensation, dehydrogenation, coagulation or oxidation.

The CDSM of the CRECK Modeling Group [27] will be used in this work. The detailed kinetic mechanism in [27] also includes the gas phase kinetics constituting of 189 gaseous species up to pyrene ($C_{16}H_{10}$). The CDSM divides the molecular mass range of the hydrocarbon species above pyrene into 20 sections, from which the first four BINs (from BIN_1 to BIN_4) represent the heavy PAHs and the rest the soot particles (from BIN_5 to BIN_{12}) and the soot aggregates (from BIN_{13} to BIN_{20}). In order to cover the aggregate size range in the heavily sooting flames investigated in this work, the kinetic mechanism was extended with 4 further mass sections (BIN_{21} to BIN_{24}). The kinetic mechanism, when calculating the collision diameter (Eq. 1.2), considers soot particles as spheres and soot aggregates as an assembly of uniform sized primary particles, with the size of the last spherical particle (BIN_{12}) equal to 10.14 nm and a fractal dimension of 1.8.

Sections are further divided based on the hydrogenation level. Three subsections (A, B and C) for heavy PAHs and soot particles up to BIN_{10} and two

subsections (A and B) for BIN_{11}, BIN_{12}, and aggregates are defined. Thereby the classes are represented by a combination of lumped pseudo-species with an assigned number of carbon and hydrogen atoms. For each subsection a corresponding radical is also considered. The combination of the particle mass and the H/C ratios providing the total number of 116 subsections are summarized in Table 2.1.

The differentiation with respect to the H/C ratio makes it possible to describe the aging and the dehydrogenation of the soot particles and aggregates. The model was validated in terms of H/C ratio prediction in a rich premixed ethylene flame [27]. The hydrogenation levels are able to represent the core shell structure of the nascent soot particles constituting of heavy PAHs linked by aliphatic bridges and the alkylation which precedes the graphitization.

As mentioned, to calculate the kinetic constant (k), reference gas-phase reactions are used to derive the parameters of the modified Arrhenius formula:

$$k = A \cdot T^n exp(-E_a/R_u T) \tag{2.3}$$

where A is the frequency factor, E_a is the activation energy, n is the temperature exponent, and R_u is the universal gas constant.

Heavy PAHs can form the soot particles (inception) by interacting with each other or by the addition of smaller gas-phase species. For the interactions of two heavy PAHs the kinetic constants are derived from the reference gas-phase reactions, i.e. for the radical-radical interaction from the recombination of cyclopentadienyl radicals ($C_5H_5\bullet$), for the radical-molecule interaction from the benzocyclobutadiene (C_8H_6) and phenyl (C_6H_5) interaction and for the molecule-molecule interaction from the pyrene ($C_{16}H_{10}$) dimerization. The frequency factors are determined from the reference reaction's frequency factor (A_{ref}) based on the collision diameter and the reduced mass (μ_{r}):

$$A/A_{ref} = \frac{d_c^2/\sqrt{\mu_r}}{d_{c,ref}^2/\sqrt{\mu_{r,ref}}} \tag{2.4}$$

where k_B is the Boltzmann constant.

For the HACA mechanism, the reaction parameters are derived from a hydrogen abstraction from a naphthalene radical ($C_{10}H_8\bullet$), and a successive acetylene addition. The rate of H-abstraction is adjusted based on the number of H atoms of the BIN, whereas the frequency factor of acetylene addition is rescaled based on the particle or aggregate surface area and the H/C ratio:

$$\text{Soot particles:} \qquad A/A_{ref} = 1 + \frac{d_p^2 \cdot H/C}{d_{ref}^2} \tag{2.5}$$

$$\text{Soot aggregates:} \qquad A/A_{ref} = 1 + \frac{n_p \cdot d_{pp}^2 \cdot H/C}{d_{ref}^2} \tag{2.6}$$

where d_{ref} = 1.91 nm, which is the size of the smallest particle assumed here (BIN_5).

Heavy PAHs						
BIN_i	nC	Mass [amu]	Diameter [nm]	H/C		
BIN_1	20	~ 250	0.81	0.8	0.5	0.3
BIN_2	40	~ 500	1.02	0.8	0.5	0.3
BIN_3	80	~ 1000	1.28	0.75	0.45	0.3
BIN_4	160	~ 2000	1.62	0.7	0.4	0.3
Soot particles						
BIN_i	nC	Mass [amu]	Diameter [nm]	H/C		
BIN_5	320	$\sim 4{\cdot}10^3$	2.04	0.65	0.35	0.2
BIN_6	640	$\sim 8{\cdot}10^3$	2.57	0.6	0.35	0.15
BIN_7	1250	$\sim 1.55{\cdot}10^4$	3.21	0.55	0.3	0.1
BIN_8	2500	$\sim 3{\cdot}10^4$	4.04	0.5	0.25	0.1
BIN_9	$5{\cdot}10^3$	$\sim 6{\cdot}10^4$	5.09	0.45	0.2	0.1
BIN_{10}	10^4	$\sim 1.2{\cdot}10^5$	6.4	0.4	0.15	0.1
BIN_{11}	$2{\cdot}10^4$	$\sim 2.45{\cdot}10^5$	8.05	0.35	0.1	
BIN_{12}	$4{\cdot}10^4$	$\sim 4.9{\cdot}10^5$	10.14	0.35	0.1	
Soot aggregates						
BIN_i	nC	Mass [amu]	Vol. Eq. Diameter [nm]	H/C		
BIN_{13}	$8{\cdot}10^4$	$\sim 9.7{\cdot}10^5$	12.7	0.3	0.1	
BIN_{14}	$1.6{\cdot}10^5$	$\sim 1.95{\cdot}10^6$	16.0	0.3	0.1	
BIN_{15}	$3.2{\cdot}10^5$	$\sim 3.9{\cdot}10^6$	20.2	0.25	0.1	
BIN_{16}	$6.4{\cdot}10^5$	$\sim 7.8{\cdot}10^6$	25.4	0.2	0.05	
BIN_{17}	$1.25{\cdot}10^6$	$\sim 1.51{\cdot}10^7$	31.8	0.2	0.05	
BIN_{18}	$2.5{\cdot}10^6$	$\sim 3.02{\cdot}10^7$	40.0	0.2	0.05	
BIN_{19}	$5{\cdot}10^6$	$\sim 6.02{\cdot}10^7$	50.4	0.2	0.05	
BIN_{20}	$1{\cdot}10^7$	$\sim 1.21{\cdot}10^8$	63.5	0.2	0.05	
BIN_{21}	$2{\cdot}10^7$	$\sim 2.42{\cdot}10^8$	80.0	0.2	0.05	
BIN_{22}	$4{\cdot}10^7$	$\sim 4.8{\cdot}10^8$	100.8	0.2	0.05	
BIN_{23}	$8{\cdot}10^7$	$\sim 9.7{\cdot}10^8$	127.1	0.2	0.05	
BIN_{24}	$1.6{\cdot}10^8$	$\sim 1.95{\cdot}10^9$	160.1	0.2	0.05	

Table 2.1: *Classes of lumped pseudo-species or BINs (Heavy PAHs, Soot particles, and Soot aggregates) and their properties: mass, equivalent spherical diameter, and H/C ratio [27]*

Beside the HACA mechanism, small resonantly-stabilized radicals (RR•), like propargyl (C_3H_3•), ethylnyl-1-vinyl (CH≡C–C•=CH_2 or i-C_4H_3•), 1,3-butadien-2-yl (CH_2=C•–CH=CH_2 or i-C_4H_5•) and cyclopentadienyl (C_5H_5•) may further grow the soot particle. The reference reactions considered here are those corresponding to their addition to C_6H_6 and C_6H_5•, and the collision frequency change is defined by Eq. 2.4.

Similarly, the PAH and the heavy PAH condensation on the soot particles is described based on the above-listed reactions. However, the kinetic parameters are obtained from the asymptotic values of the reference addition reactions on BIN_{20} and, instead of defining the energy barrier the collision efficiency, (γ) is used:

$$k = A_{ref} \cdot T^{0.5} \cdot \gamma = A_{ref} \cdot T^{0.5} \cdot \frac{100 + d_c^{6.5}}{10^5 + d_c^{6.5}} \tag{2.7}$$

The reference reaction for the dehydrogenation of soot particles is different for the radicals and the molecules. While the reaction parameters of a radical

dehydrogenation is derived from the fluorene ($C_{13}H_{10}$) formation from a benzyl-2-phenyl radical ($C_{13}H_{11}\bullet$), the analogy for molecules is the reaction of the di-phenyl-methane ($C_6H_5CH_2C_6H_5$) forming flourene. The frequency factor depends on the H/C ratios.

H-addition and subsequent demethylation (the ipso-addition reaction) further favor dehydrogenation, but it is assumed to take place only for BINs with a H/C ratio above 0.3. The kinetic parameters are derived from the demethylation of 1-methylnaphthalene ($CH_3C_{10}H_7$). Furthermore, C–H fission can result in surface radicals at very high temperatures, for which the reference kinetic reaction is the benzene C–H fission. Again, the hydrogenation level was considered in recalculating the frequency factor.

For particle coalescence and aggregation, the kinetic parameters for the radicals and the molecules are defined to be similar. However, the reference frequency factor varies between the coalescence of soot particles and the interaction of aggregates with another aggregate or a soot particle. The collision efficiency progressively increases with the particle weight until $\sim BIN_9$, from where a constant, unity γ is considered.

Oxidation is still one of the least understood mechanisms in soot evolution. This process is strongly dependent on the soot particle structure, maturity, and morphology [67]. The oxidation happens due to OH• and O• radicals or O_2 molecules. The reference reactions used in the mechanism are listed below:

$$
\begin{aligned}
&OH\bullet + C_{16}H_{10} \Longrightarrow C_{14}H_9\bullet + CH_2CO\\
&OH\bullet + C_{11}H_{10} \Longrightarrow C_9H_8 + CO + CH_3\bullet\\
&OH\bullet + C_{10}H_7 \Longrightarrow C_9H_7 + CO + H\bullet\\
&OH\bullet + C_{10}H_8 \Longrightarrow C_9H_8 + HCO\bullet\\
&O\bullet + C_{16}H_{10} \Longrightarrow C_14H_8\bullet + HCCO\bullet\\
&O\bullet + C_{10}H_7\bullet \Longrightarrow C_9H_8 + CO\\
&O_2 + C_{10}H_7\bullet \Longrightarrow C_8H_6 + CO + HCO\bullet\\
&O_2 + C_{10}H_7\bullet \Longrightarrow C_9H_7 + C\bullet + CO\\
&O_2 + C_{16}H_9\bullet \Longrightarrow C_{14}H_9\bullet + 2CO
\end{aligned}
$$

The oxidation by $HO_2\bullet$ is also implemented in the kinetic mechanism based on the reference reaction involving the indenyl ($C_9H_8\bullet$) radical. From the kinetic parameters of the reference reactions, the frequency factor is derived by the same scaling method used for the collision frequency at the inception (Eq. 2.4).

The collision frequencies of the processes depend on the collision diameter and consequently on the primary particle size. For calculating the collision frequency, the above-described mechanism assumes spherical particles below a critical size (BIN_{12}) and a constant primary particle size for the larger, aggregate particles. On the contrary several, recent CDSMs assume spherical particles for all sections [47, 104, 154]. However, it has been demonstrated in Section 1.3 that soot particles can have various sized primary particles.

The extension of CDSM to a bivariate version (particle size-primary particle size) is possible and it provides a new perspective to the kinetic mechanism validation. Furthermore, access to the reaction rates and the PPSD can help to reveal

which conditions and formation processes result in particles with large surfaces. Preventing these conditions may help a more focused fight against harmful pollutants.

If two-way coupling is applied, i.e. the effect of the primary particle size change is considered at the reaction rate calculation level, improved performance of the model prediction is expected. The effect on the processes can be estimated based on the change in the collision frequency or in case of aggregation and coalescence also in the collision efficiency. The latter does not show significant sensitivity to the primary particle diameter in the range of 10 to 60 nm, typical values for d_{pp}.

In Figure 2.1, the proportions of the collision frequencies derived by the modified d_{pp} (A_{m}) and by the original assumption of d_{pp} = 10.14 nm (A_0), from Eq. 2.4 and 2.6, are demonstrated. As $n_{\mathrm{p}} \cdot d_{\mathrm{pp}}/d_{\mathrm{ref}} \cdot H/C \gg 1$ was typical, the A_{m}/A_0 ratio from Eq. 2.6 for the different BINs were quasi-identical, in the Figure 2.1, the "$+1$" term in Eq. 2.6 was neglected for calculating A.

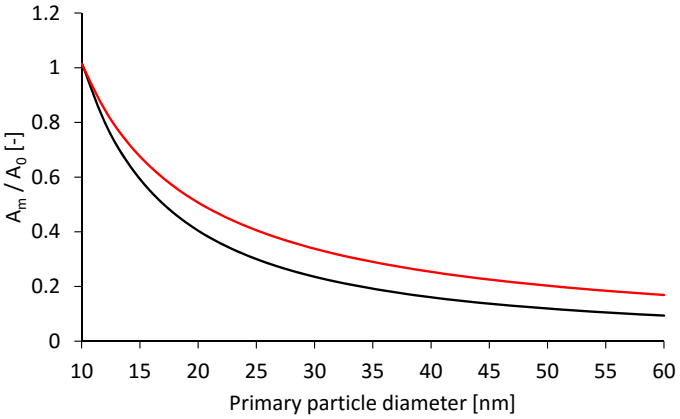

Figure 2.1: *Collision frequency dependency on the primary particle diameter based on Eq. 2.4 and 2.6, normalized by A_0 (d_{pp} = 10.14 nm assumption).*

The effect on the collision frequency is sensitive to d_{pp} at low primary particle diameters and tends to converge with the size increment of the primary particle. Up to 60 nm the collision frequency might drop to the 1/5 or 1/10 of the original value. This affects the HACA mechanism through Eq. 2.6, the RR, the PAH and the heavy PAH condensation, the aggregation, the coalescence, and the oxidation through Eq. 2.4. Unfortunately, as the formation of soot is a result of a complex combination of these processes, their combined effect cannot be assessed by this analysis.

2.2.3 Overview of state-of-the-art laminar diffusion flame simulations

ADSMs have been already used to calculate primary particle size in laminar coflow diffusion flames and by the model proposed in this work the CDSMs becomes suitable for this task too. Therefore, in the following the performance of the state-of-the-art sectional models in coflow flames with respect to soot volume fraction and/or primary particle size are briefly discussed.

The ADSM model was intensively used in the last two decades to investigate

coflow flames by Smooke and coworkers [144, 145, 157–160]. The model from [144] was used by Connelly et al. [161] to simulate the F80 flame and the soot volume fraction peak value was captured. However, the soot volume fractions of flames with higher dilution were over-predicted by a factor up to ∼3.5. The same model was updated by Dworkin et al. [162], providing a good agreement in terms of soot volume fraction along the centerline of a coflow flame, which was the weak point in the earlier study. In this work, the agreement with experiments along the centerline in terms of mean d_{pp} was in a factor of two for a pure ethylene laminar coflow flame [163].

The model of Zhang et al. [150, 164, 165] was recently used in several coflow flame investigations. Kholghy et al. [26] modeled 3 ISF target coflow flames: Flame 1a, 4 and 2d flames which correspond to A, B and C in the referred article. Their model performed well for Flame A [163] (for which the used soot model parameters were originally optimized [164, 165]), however, simulation of Flame B resulted in a ∼3 times smaller value for the centerline peak f_{v}, and no information on the validity of the radial profile was provided. For Flame C, a factor of only ∼1.3 was observed on the peak f_{v} value, however, the location at the various heights mismatched to the experimental observations in terms of maximum soot volume fraction.

In the work of Herdman et al. [166], numerical peak f_{v} values were ∼1-3 times smaller on the F32-F80 coflow flames, the transition of soot volume fraction peak location was captured. However, the f_{v} profile for F40, F60 and F80 flames showed too intense soot formation on the wings. Khosousi et al. [167] studied a wide range of coflow flames (F32-F80 flames and the *Santoro flames* [163, 168] (SF 1-4)) obtaining numerical peak soot volume fraction values within the measurement uncertainty. A good spatial agreement was found along a pathline crossing the wing for the SF1 and SF4 flames, both in terms of the soot volume fraction and the primary particle size. However, the validity of f_{v} and d_{pp} was not presented at further locations, so that the agreement with experiments cannot be definitely assessed.

Another recent work, proving the difficulty of capturing the maximum soot volume fraction transition from centerline to wings with decreased dilution, is presented by Veshkini et al. [169]. They simulated by the model of Thompson et al. [105] numerous coflow flames: the *Santoro flames*, flames F32-F80 and the coflow flames presented in [170]. A good agreement was obtained by introducing a new model parameter, the varying thermal age. However, the trend of the soot location transfer from the centerline to the wings was not captured.

Due to its computational cost, CDSM is moderately used for coflow flame investigations. D'Anna et al. [30] investigated a coflow flame (the *Santoro burner* [163]) underestimating the soot volume fraction peak value by a factor of ∼2. The same flame was modeled by Sirignano et al. [47] providing a good agreement in terms of f_{v} peak value, but a mismatch on the spatial distribution. However, their model performed well for a methane flame [158].

2.3 Monte Carlo simulation

Monte Carlo (MC) simulation is a very accurate statistical approach capable to predict soot particle evolution, potentially providing the exact shape of the resultant particles and the NDF. In MC simulations the particle population is represented by an ensemble of separately tracked stochastic particles, therefore the characteristics of particle population can be recovered on a very high level of detail. Nevertheless, in order to provide this detailed information on the particles, high computational costs arise, which restrict the utilization to zero or one dimension [59, 60, 107–110, 116]. Therefore, the Monte Carlo approach is not at the core of the thesis, since the purpose of this work is to provide a tool applicable in multidimensional flames, thus only a few examples of its application are presented.

Violi et al. [171] investigated the structure of nanoparticles by a combined model of Monte Carlo algorithm and a molecular dynamics module providing information about the atomistic scale structures (bonds, bond angles and dihedral angles). Regarding the aggregate particle shape, in the work of Mitchell et al. [60], several scenarios were tested to investigate the resultant particle sphericity for various rates of surface growth and aggregation. As mentioned in Section 1.3, the two main influencing factors for the final particle shape were found to be the speed of surface growth rate and the colliding primary particle size.

In more recent works [59, 107, 108], the same approach was used to further investigate the shape descriptors for quantifying particle geometry. The importance of nucleation and the primary particle size of aggregating particles was highlighted. A zero-dimensional simulation of a diesel engine was performed by Etheridge et al. [109], by the MC method developed by Celnik et al. [172] to investigate the morphology and chemical composition of soot aggregates. MC simulations were several times utilized to validate another type of statistical soot modeling methods, e.g. the method of moments (MOM) [110, 116].

CHAPTER 3

Primary particle tracking with CDSM[1]

In the following chapter, the motivation behind extending the chemical discrete sectional models (CDSMs) to predict and account for the primary particle size will be recalled. Then, a method to determine the primary particle size with CDSM will be presented. For this, a new variable is introduced and the related transport equations are derived. Finally, the implementation of the model in the CRECK Modeling Group's kinetic mechanism will be presented.

3.1 Motivation

In the CDSMs, the molecular mass scale of large hydrocarbons is split up into discrete sections (BINs), assigning to each one representative species, and the transport equations for the species' mass fraction are solved. Recent CDSMs use an extended description by defining subsections to distinguish between the species (consequently soot particles) with the same molecular weight but different H/C ratio or to differentiate between molecules and radicals.

However, in order to retrieve information on the particles' surface or their primary particles' size, the extension of these model with a new variable is required. By assigning a new variable for each soot section, the mean primary particle size per BIN can be tracked. The evolution of the variable can be described by a dedicated transport equation for the primary particle number. Similarly to the mass fraction of the BINs, the source terms in the governing equations, originating from the inter-particle and gas phase-particle interactions, are determined by the chemical reactions. The size distribution in a single mass section is not resolved,

[1] content of the Chapter was extracted from A.L. Bodor, B. Franzelli, T. Faravelli, A. Cuoci, A post-processing technique to predict primary particle size of sooting flames based on a chemical discrete sectional model: application to diluted coflow flames, Accepted (In press) to Combustion and Flame (2019) [173]

which results in a loss of information on the PPSD, however, a first approximation of the PPSD can be provided.

3.2 The primary particle tracking model

In the following, first, the model used for treating the particle collision and the gas-phase–particle interaction is presented. Then the new variable, the primary particle density (ρ_{pp}), is introduced and the related transport equation is provided. The change of the ρ_{pp} caused by the inter particular and gas-phase–particle interactions is the result of all related chemical reaction, therefore, the chemical source term in the transport equation can be expressed by the sum of their separate contributions. For this reason, the contribution of a generalized chemical reaction will be derived. To treat the obliteration caused by surface growth, and the similar effect caused by coalescence, a correction term is introduced and the related correction factor is derived. The process of information loss on the PPSD due to not resolved PPSD of the sections is demonstrated by an example. The mean diameters extracted from the PPSD are defined. Finally, the CDSM in which the described primary particle tracker (PPT) was implemented is presented.

The pathway for the formation of aggregates considered in the following, and also used by the bivariate ADSM models mentioned in Section 2, was suggested originally by Lahaye [24]. It assumes that first a multitude of small particles are formed. Then, their growth or collision results in larger, but still spherical particles that solidify later on. Finally, the collision of the solidified particles produces aggregates, which can grow larger by further aggregation, by condensation or surface growth. The schematic illustration of the above process can be seen in Figure 3.1.

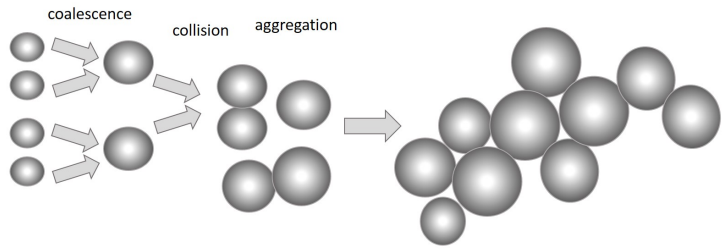

Figure 3.1: *Schematic illustration of particle formation based on the suggestions of Lahaye [24]*

Following the model of Lahaye et al. [24], particles below the solidification limit (BIN_i, $i < N_{\mathrm{s}}$) are considered to coalesce completely, resulting in spherical particles, whereas pure aggregation is assumed between particles larger or equal to the limit (for BIN_i, $i \geq N_{\mathrm{s}}$). The interactions of small and big particles are taken as a splash of the former on the latter, former distributing its mass homogeneously on the surface. This last interaction, similarly to obliteration, leads to a more spherical shape, thickening the connection of primary particles [59, 107, 149]. In the following, the shape modifications leading to increased sphericity will be referred as to "surface rounding" regardless of the process' type.

The new variable, the so-called primary particle number density ($\rho_{\mathrm{pp},i}$), is de-

fined for each soot section and represents the number of primary particles of the type BIN$_i$ per mass unit. For not solidified (spherical) particles, the primary particle number density can be derived from molecular weight (M_i) and mass fraction (Y_i) as:

$$\rho_{pp,i} = \frac{Y_i N_{Av}}{M_i} \qquad i \leq N_s \tag{3.1}$$

where N_{Av} is the Avogadro's number. Therefore, no additional transport equation needs to be solved for BIN$_i$ with $i < N_{\text{s}}$.

$\rho_{\text{pp},N_{\text{s}}}$ is the primary particle number density for the smallest particle colliding without coalescence. This particle is still considered spherical as it was formed by coalescence or surface growth, therefore, $\rho_{\text{pp},N_{\text{s}}}$ can be derived by Eq. (3.1).

The primary particles are assumed to possess the same chemical, thermal, and transport properties as the representative species of the section. Therefore, the transport equation for the $\rho_{\text{pp},i}$ of the BINs corresponding to the aggregate particles (BIN_i $i > N_{\text{s}}$) takes the following form:

$$\frac{\partial}{\partial t}(\rho\rho_{pp,i}) + \nabla \cdot (\rho\rho_{pp,i}\bar{v}) = -\nabla \cdot (\rho\rho_{pp,i}\bar{V_i}) + \dot{\Omega}_{pp,i} \tag{3.2}$$

where ρ is the density of the mixture, $\bar{v}$ is the velocity, $\bar{V_i}$ is the diffusion velocity of the BIN$_i$ [174] and $\dot{\Omega}_i$ is the chemical reaction source term. Due to the high Schmidt number characterizing the soot particles [175], the contribution of molecular diffusion is negligible.

Only thermal diffusion plays a significant role [176] and was included in the transport equation. The chemical reaction source term is the sum of the contributions of all reaction related to BIN$_i$ ($\dot{\omega}_{l,i}$), the sum of the sink ($S_{\text{Death},l,i}$) and the formation ($S_{\text{Birth},l,i}$) terms of the specific reactions:

$$\dot{\Omega}_{pp,i} = \sum_l \dot{\omega}_{l,i} = \sum_l \left(S_{Death,l,i} + S_{Birth,l,i}\right) \tag{3.3}$$

where *l* is the index of the reaction.

The source term depends only on the primary particle number of particles colliding without coalescence and can be determined for a general reaction of shape:

$$\begin{aligned} &\sum_{i=N_s}^{N_s+N_a} \nu_i BIN_i + \sum_{i=1}^{N_s-1} \nu_i BIN_i + \sum_{j=1}^{N_g} \nu_j X_j \Longrightarrow \\ &\sum_{i=N_s}^{N_s+N_a} \mu_i BIN_i + \sum_{i=1}^{N_s-1} \mu_i BIN_i + \sum_{j=1}^{N_g} \mu_j X_j \end{aligned} \tag{3.4}$$

where X are gaseous species, N_{g} is the number of gaseous species, N_{a} is the number of BINs corresponding to the aggregate particles (aggregate BINs), ν_i and μ_i are the stoichiometric coefficients. Regarding the change in the primary particle number, only the first terms on the two sides of the reactions are relevant, as coalescing BINs and gaseous species do not affect the primary particle number directly (only through surface rounding).

The primary particle number in the i^{th} aggregate BIN species ($n_{\text{pp},i}$) can be expressed by:

$$n_{pp,i} = \frac{M_i \rho_{pp,i}}{Y_i N_{Av}} \tag{3.5}$$

The consumption of BIN$_i$ type primary particles originating from reaction l can be expressed by:

$$S_{Death,l,i} = -\frac{\nu_i M_i \rho_{ppi}}{Y_i} R_l \tag{3.6}$$

where (R) is the reaction rate and it is expressed in molar units.

The total number of new particles resulted from reaction l is the sum of the original particles (LHS of the reaction) multiplied by the term (1 - C_{r}) to account for the surface rounding phenomenon, with C_{r} being the correction factor derived later. Consequently, the total source term for the birth of the primary particles by reaction l ($S_{\text{Birth},l}$) is expressed as:

$$S_{Birth,l} = \sum_{k=N_s}^{N_s+N_a} (1 - C_r) \frac{\nu_k M_k \rho_{PBk}}{Y_k} R_l \tag{3.7}$$

The born primary particles are assigned to the resultant aggregate BINs conserving the average primary particle mass, similarly to the model of Wen et al. [105]. The resultant chemical source term can be written in the form:

$$\dot{\omega}_{l,i} = \underbrace{\frac{\mu_i M_i}{\sum_{k=N_s}^{N_s+N_a} \mu_k M_k} \sum_{j=N_s}^{N_s+N_a} (1 - C_r) \frac{\nu_j M_j \rho_{pp,j}}{Y_j} R_l}_{S_{Birth,l,i}} \underbrace{- \frac{\nu_i M_i \rho_{pp,i}}{Y_i} R_l}_{S_{Death,l,i}} \tag{3.8}$$

A drawback of this type of primary particle assignment to the resultant species is that all new primary particles have the same size, causing a narrower PPSD. However, the mean primary particle mass is conserved.

In the current model, the primary particles are assumed to have point contact within a soot particle at all instance. Actually, surface rounding would increase the area of contact between the neighboring primary particles partially merging them. In order to account for the above-mentioned merge of primary particles, the primary particle number is decreased for all related reactions, which is realized by C_{r}.

The correction factor is derived from the assumption of Patterson et al. [149], i.e. the change of the particle surface area (dS) for a deposited dV volume is related to the initial surface S_{init}:

$$\frac{\mathrm{d}S}{\mathrm{d}V} = 2 \left(\frac{S_{init}}{4\pi} \right)^{-1/2} \tag{3.9}$$

The deposited volume can be obtained for the general reaction by:

$$\mathrm{d}V = \frac{1}{\rho_{soot}}\left(\sum_{i=N_s}^{N_s+N_a}\nu_i M_i - \sum_{i=N_s}^{N_s+N_a}\mu_i M_i\right) \tag{3.10}$$

where ρ_{soot} is the soot density.

By using the relation between the aggregate volume and primary particle number, the change in primary particle number due to surface rounding becomes:

$$\mathrm{d}n_p = \frac{2dV}{V_{init}}\left(\sqrt{n_{pp,init}} - n_{pp,init}\right) \tag{3.11}$$

where V_{init} and $n_{\mathrm{pp,init}}$ are the initial volume and primary particle number respectively.

Therefore, the correction factor takes the form:

$$C_r = \frac{2}{V_{init}n_{pp,init}}\left(1 - \frac{1}{\sqrt{n_{pp,init}}}\right) \tag{3.12}$$

It has to be noticed that due to the not resolved primary particle size distribution in each single mass section, i.e. one ρ_{pp} assigned to one BIN, the aggregation narrows the PPSD. In Figure 3.2 the schematic representation of the collisions of two pair of aggregates from different size classes (BIN_A,BIN_B and BIN_C) are presented.

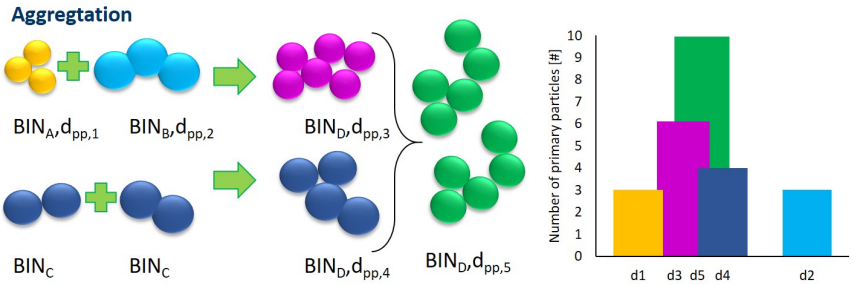

Figure 3.2: *Left: The schematic illustration of particle aggregation treatment with the proposed method. Right: The primary particle size distribution at the different stages.*

First of all, the first collision would result in a BIN_E size particle with 3 smaller ($d_{\mathrm{pp,1}}$) and 3 larger ($d_{\mathrm{pp,2}}$) primary particles. However, as only the total number of particles is tracked for a BIN, from the available information (BIN_E particle being composed of 6 primary particles) a $d_{\mathrm{pp,3}}$ value in between the two original ones ($d_{\mathrm{pp,1}} < d_{\mathrm{pp,3}} < d_{\mathrm{pp,2}}$) will be recovered. In terms of distributions, this would mean that instead of the distribution resulted from the yellow and light blue column in Figure 3.2, the one represented by the purple column will be recovered.

Secondly, both collisions result in a particle with the size $\mathrm{BIN}_{\mathrm{E}}$, but with different primary particle sizes ($d_{\mathrm{pp,3}}$,$d_{\mathrm{pp,4}}$). For the same reason as above, the recovered particles will have primary particles with the average diameter of $d_{\mathrm{pp,5}}$ instead of the three different diameters $d_{\mathrm{pp,1}}$,$d_{\mathrm{pp,2}}$ and $d_{\mathrm{pp,3}}$. Therefore, instead of the distribution resulted from the yellow, light blue and dark blue column,

in Figure 3.2, the one represented by the green column will be recovered. The aggregation homogenizes the primary particle size, which is unphysical.

To overcome this issue, a multi-subsectional model would be required, which might prevent the usage of the model in multidimensional flames due to the increased computational costs. Therefore, at the moment, only one additional variable per mass section will be used. Nevertheless, a more accurate PPSD could be potentially achieved with the multi-subsectional model, and the loss of accuracy cold be quantified. This might be an objective for the future.

The derived governing equations were implemented in the OpenSMOKE++ [177] and the laminarSMOKE [174] codes to simulate the primary particle size evolution in laminar flames. From the obtained PPSD, three different characteristic diameters may be extracted: the arithmetic mean diameter (d_{amean}), the geometrical mean diameter (d_{geom}) -which is equal to the count median diameter (d_{CMD}) in case of a lognormal distribution- and a diameter assuming monodisperse distribution while preserving the total soot mass and primary particle number (d_{mono}). They are defined as follows:

$$d_{amean} = \frac{\sum_{k=N_{min}}^{N_{max}} d_{pp,k}\rho_{pp,k}}{\sum_{k=N_{min}}^{N_{max}} \rho_{pp,k}} \tag{3.13}$$

$$d_{geom} = \left(\prod_{k=N_{min}}^{N_{max}} (d_{pp,k})^{\rho_{pp,k}} \right)^{1/\prod_{k=N_{min}}^{N_{max}} \rho_{pp,k}} \tag{3.14}$$

$$d_{mono} = \left(\frac{6}{\pi \rho_{soot}} \frac{\sum_{k=N_{min}}^{N_{max}} Y_k}{\sum_{k=N_{min}}^{N_{max}} \rho_{pp,k}} \right)^{1/3} \tag{3.15}$$

where N_{max} and N_{min} are the indexes of largest and smallest BIN considered to calculate the mean diameter, respectively. This also determines the low cut-off size, i.e. the smallest particle accounted ($d_{\text{pp},N_{\text{min}}}$) to calculate the mean diameter.

3.3 Implementation in the CDSM proposed by the CRECK Group

In this work, the kinetic mechanism including a CDSM of the CRECK Modeling Group [27] was extended by the above-described method. To keep the consistency with the original assumption of the kinetic model, N_{s} = 12 is taken, i.e. the smallest aggregating particle has a diameter of $\sim$10 nm ($d_{\text{pp},N_{\text{s}}} = 10.14$ nm). This means one primary particle per molecule was assumed for BINs smaller or equal to BIN_{12} (spherical particle assumption) and the transport equation was solved only for the BINs corresponding to the aggregate particles (BIN_i $i > 12$). The implementation of the primary particle tracking was done without the two-way coupling between d_{pp} and the kinetic mechanism, meaning that new results on d_{pp} are not considered to recalculate the reaction rates derived from the original assumption (d_{pp} = $\sim$10).

CHAPTER 4

Approaches of numerical PPSD validation by experimental data

In the following, first the three main measurement techniques used to obtain information about the primary particle diameter (d_{pp}), and the Primary Particle Size Distribution (PPSD) in the presence of aggregates are presented, with more details on the Time-Resolved Laser-Induced Incandescence (TiRe-LII). Then, a few precedents of applying the approach of synthesized signal comparison (forward method) instead of the traditional "fundamental quantity comparison" (inverse method) are provided. In order to perform the validation with the forward method, the incandescence signal has to be modeled. The model implemented in the code to reconstruct LII signal from the numerical PPSD data is based on the work of Hofmann et al. [120] and Liu et al. [121, 122] and the details of the model are presented in this chapter.

Then, in order to investigate the potential of the forward approach for the numerical PPSD validation by TiRe-LII, the uncertainties related to the traditional approach, and possibly avoided by the novel approach, are quantified. This is done by overviewing former analysis from the literature and by performing sensitivity studies on the incandescence signal through numerical LII signal simulation.

4.1 Experimental methods to determine PPSD

Since the importance of the primary particle size distribution was revealed, experimentalists sought the best method to provide the PPSD for all conditions. The most frequently used approaches are the Transmission Electron Microscope (TEM) and the Helium-Ion Microscopy (HIM) analysis of thermophoretically

sampled soot particles and the Time-Resolved Laser-Induced Incandescence (TiRe-LII).

TEM analysis of thermophoretically sampled soot have been extensively applied to determine d_{pp} and PPSD [74, 76, 77, 83, 88, 98, 178, 179] for a long time. In TEM, the d_{pp} is directly measured from the picture taken by the microscope. The direct observation of the particle allows gaining information about the shape of the particles too. The images shown in Section 1.3 were provided by this technique. Despite only a two dimensional projection is available from these pictures, important information becomes available thanks to this method, e.g. the transition from spherical particles to aggregates can be detected.

Unfortunately, such an invasive method can significantly perturb the system under study. The perturbation caused by the sampling grid with different offsets for slow (0.35 m/s) and fast (2 m/s) flow was numerically investigated by Kempema et al. [77]. In Figure 4.1 their results are shown for the origin of particles that reach the TEM grid surface at different sample times, where δ is the distance between the radial location of upstream particles that reach the grid surface and the probe's front surface.

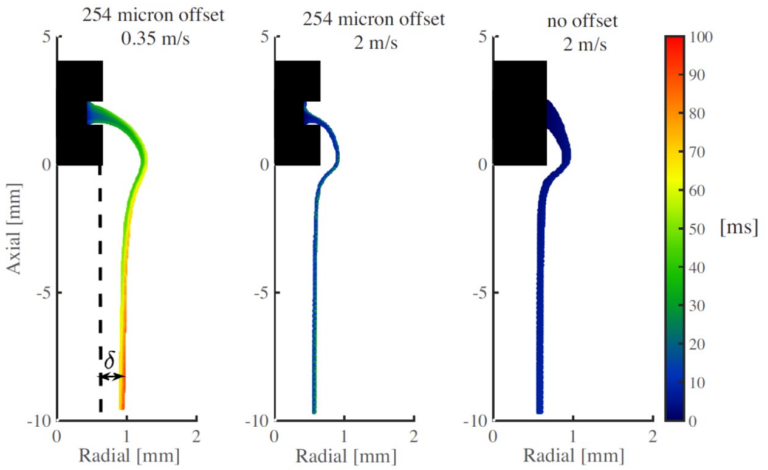

Figure 4.1: *Thermophoretic sampling simulations with grid offsets of* $254\,\mu m$ *(u = 0.35 m/s, left),* $254\,\mu m$ *(u = 2 m/s, center), and* $0\,\mu m$ *(u = 2 m/s, right), reprinted from [77]*

As the sampling is performed point-wise and at each location, a relatively large amount of images are required to ensure a high signal-to-noise ratio, this can result in a sampling time of 80-170 ms [77]. Therefore, the method cannot achieve high temporal and spatial resolutions. Furthermore, the results may depend on the algorithm and/or research criteria used to visually determine the number and shape of d_{pp} of an aggregate. Nevertheless, TEM is still one of the best techniques to visualize soot particles down to the size of $\sim$10 nm [98].

Helium-Ion Microscopy (HIM) was developed and applied for nanoscale microscopy and metrology a decade ago [180]. The retrieved information and the difficulties are similar to TEM, however since the HIM can achieve higher contrast, it is able to capture soot particles as small as 2 nm [35, 181].

Alternatively, laser diagnostics developed notably in the last decades and became a very accurate experimental approach suitable to perform investigations

even in the harsh conditions of combustion [78, 89, 182]. Among them, the Time-Resolved Laser-Induced Incandescence (TiRe-LII) is an in-situ minimally invasive diagnostic technique that can be used to retrieve information on d_{pp} and PPSD [84, 85, 88, 183]. In addition, with the TiRe-LII, high spatial and temporal resolution is feasible. Furthermore, it is easily applicable in high-pressure conditions as no lead-through for the sampling line is needed. Even heavily sooting flames can be investigated as there is no fear from the clogging of the sampling system.

In TiRe-LII particles are heated with a nanosecond laser pulse and the induced incandescence signal is subsequently recorded [184]. As large soot particles cool more slowly than small ones, the temporal evolution of the incandescence signal, which is a function of the particle temperature, can be used to determine the primary particle size.

Due to their advantageous properties, the TiRe-LII technique and laser diagnostics, in general, are powerful tools to investigate soot formation. However, it should be noticed that when using laser diagnostics, the fundamental quantities of interest are usually not directly measured, the validation of the numerical models in terms of PPSD relies on comparing the numerical PPSD to the one derived from the LII signal by the post-processing. For this, most of the time, various quantities have to be quantified simultaneously, leading to additional measurements, post-processings, and assumptions. Unfortunately, each of them may be considered as a new source of uncertainty.

In order to recover the PPSD from the LII signal decay, the LII signal is reconstructed by solving the mass and the energy balance equations for assumed PPSDs. Usually, the problem is recast as a minimization problem, that allows identifying the distribution parameters minimizing the deviation between the measured signal and the reconstructed one. This is obtained either by iteratively solving the conservation equations describing the particle cooling and calculating the incandescence for each measured signal until the deviation is below the desired level [85, 88, 185, 186], or by preliminary storing a selection of reconstructed signals for many distributions, with a wide range of characteristic parameters, into a lookup table and identifying the best match between tabulated and measured signals [84, 187, 188]. Current models obtain the signal decay by solving the energy and mass equations of the particles, which will be described in more detail in Section 4.3.

It has to be highlighted, that, while soot particles and aggregates can be heated up by the laser beam over a broad spectrum, from the ultraviolet to the infrared, and their behavior can be described by black-body radiation, internal energy transfer and dissipation, for very small particles, especially close to the molecular scale, this may not be true. Nanostructures are mainly characterized by visible-transparency and they tend to interact with light in a different way due to their condensed phase state and transitional nature [29, 189–191]. For these particles laser induced fluorescence was observed both in the presence and in the lack of soor particles and aggregates [29, 189, 190, 192–195]. In the work of Sirginano et al. [191] the size of these nanoparticles was around 2-4 nm, showing no LII emission in ethylene/air premixed flames. On the contrary, in the study of Betran-

court et al. [186], particles of the same range were observed to emit LII signal in two sooting flat premixed flames of n-butane. These contradictory observations ask for further investigation and may indicate that not just the size but also other properties of the nanoparticles may influence its ability to emit incandescence signal.

4.2 Validation strategy of numerical PPSD through incandescence signal comparison[2]

Despite the extensive use of TiRe-LII for primary particle size prediction, the validation of the numerical PPSD with this measurement technique is still affected by uncertainties, especially because the d_{pp} is not directly measured. Nowadays, computational simulations provide a broad range of variables with constantly improving accuracy. This provides a motivation to perform the validation by directly comparing the experimental signal to the one synthesized from the numerical results. This idea can be applied for numerical PPSD validation by comparing the experimentally detected incandescence signal decay and the one reconstructed from the numerical results.

One example of utilizing the idea of comparing directly experimental data to the synthesized signal is the work of Boyce et al. [197], where interferometric maps of a hypersonic flow fields from simulation and measurement were compared. Another example is the one of Danehy et al. [198], where planar laser-induced fluorescence (PLIF) signal was reconstructed from CFD simulation with determining the quenching dependence for the existing flow conditions. Connelly et al. [199] applied the approach for two different quantities; NO laser-induced fluorescence (LIF), both in non-sooting and sooting diffusion flames, and luminosity in sooting diffusion flames. In this work, the Boltzmann and quenching corrections, required to derive the NO concentration from the NO LIF signal, nearly doubled the noise level: from 3% (measured NO LIF) to 5% (measured NO mole fraction) of the 70 ppm average [199]. These corrections are calculated from the temperature and the major species concentration, which can be easily accessed from the numerical simulations, without noise. Therefore, though their comparison led to the same conclusions with the traditional comparison and the new approach, the latter ensured higher certainty.

In order to perform a similar validation for the PPSD, the incandescence signal of the numerical PPSD has to be modeled. The code developed to recover the LII signal from the numerical PPSD is based on the model described in the following.

4.3 TiRe-LII signal modeling

Both the forward and the inverse method require the modeling of the incandescence signal. Recent models derive the signal by solving the energy (Eq. 4.1) and mass (Eq. 4.2) equations of the particles. The internal energy change ($\dot{\Omega}_{\text{int}}$) originates from the absorption of the laser energy [122, 200, 201], the blackbody

[2] content of the Chapter was extracted from [196]

radiation [202], the conductive cooling [203] and the sublimation [204]. The energy balance can be written as

$$\dot{\Omega}_{abs} = \dot{\Omega}_{int} + \dot{\Omega}_{evap} + \dot{\Omega}_{cond} + \dot{\Omega}_{rad} \tag{4.1}$$

where $\dot{\Omega}_{\text{abs}}$ is the energy flux due to laser absorption, $\dot{\Omega}_{\text{evap}}$ is the energy flux related to evaporation, $\dot{\Omega}_{\text{cond}}$ the energy flux due to heat conduction and $\dot{\Omega}_{\text{rad}}$ the radiative heat loss. The particle mass (m_{p}) changes due to the evaporation, so that

$$\frac{dm_p}{dt} = J_{evap} \tag{4.2}$$

where J_{evap} is the evaporated mass current.

The more detailed model of Michelsen et al. [184] also accounts for thermal annealing, oxidation, and thermionic emission. A schematic figure of all occurring phenomena are shown in Figure 4.2.

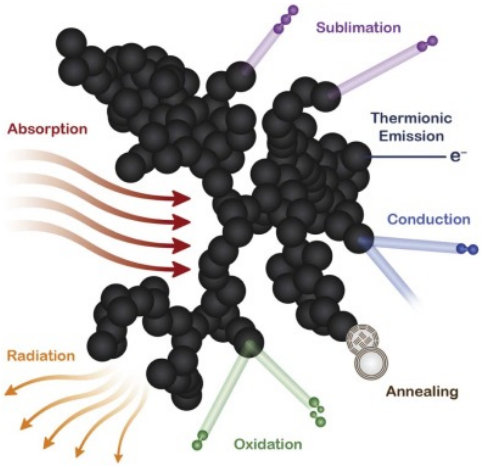

Figure 4.2: *Schematic plot of particle energy balance for TiRe-LII, reprinted from [205]*

Details on the phenomena and the equations, used in the code created to reconstruct the incandescence signal in this work to determine the terms in Eq. (4.1) and Eq. (4.2), are presented in the following based on the work of Hofmann et al. [120]. This also means that the approach of Fuchs et al. [206] was used to model the conduction and that the shielding effect was accounted for according to the study of Liu et al. [121, 122] by introducing an effective diameter (d_{eff}) of the particle.

Absorption

First, the particle absorbs partially the laser beam's energy, the ratio between the total and absorbed energy depends on the number of primary particles in the aggregate (n_p) and the primary particles' absorption cross section (C_{abs}). So that, the absorption of the laser light by a particle is described by

$$\dot{\Omega}_{abs} = n_p C_{abs} F(t) \tag{4.3}$$

where $F(t)$ is the temporal intensity profile of the laser. For sufficiently large laser wavelength, i.e. $\pi d_p/\lambda < 0.3$, C_{abs} takes the form of

$$C_{abs} = \frac{\pi^2 d_{pp}^3}{\lambda} E(m) \tag{4.4}$$

with the excitation wavelength λ and the soot-absorption, $E(m)$, which is a function of the complex index of refraction [207].

Conduction

The heated particle releases heat to the surrounding. The treatment of heat conduction is split up into three regimes depending on the local gas-kinetic conditions: free-molecular regime ("FM"), the continuum regime ("C") and the transition regime ("T"). The flames investigated in this work are operated on atmospheric pressure and the temperature range is between 293 and 2300 K. Therefore the mean free path is varying between a few nm to a few 100 nm, resulting in a Knudsen number Kn ≈ 1, which addresses the transition regime.

Filippov et al. [208] showed that in case of large particle-to-gas temperature ratios, like in the case of LII measurements, the simple harmonic mean method can produce significant errors. Therefore, the Fuchs approach [206] was applied, which is applicable for the entire range of Knudsen number, even in the transition regime.

The model of Fuchs splits up the environment of the particle into two separate domains. An inner domain is considered with the free-molecular regime type of heat conduction within a limiting sphere surrounding the particle with a thickness of δ. Outside of this domain, the heat conduction is modeled with the continuum regime equations. Within the limiting sphere the temperature is between the particle temperature (T_p) and the limiting sphere temperature (T_δ), and outside between T_δ and the gas temperature (T_g).

In the free-molecular regime, the heat conduction is dominated by the molecule-particle collisions. Therefore, the heat conduction can be described by the following expression [208]:

$$\dot{\Omega}_{cond,FM} = \alpha_T \pi d_{eff,fm}^2 \frac{p}{8} \left(\frac{8RT_g}{\pi M_g}\right)^{1/2} \frac{\gamma^* + 1}{\gamma + 1} \left(\frac{T_p}{T_g} - 1\right) \tag{4.5}$$

where α_T is the soot particle thermal accommodation coefficient, d_eff is the effective diameter, p_g is the gas pressure, M_g is the molecular weight of the gas and γ^* is the average value of the specific heat ratio [208], which can be calculated from

$$\frac{1}{\gamma^* - 1} = \frac{1}{T - T_\delta} \int_{T_\delta}^{T_p} \frac{dT}{\gamma - 1} \tag{4.6}$$

The expression for the continuum regime is:

$$\dot{\Omega}_{cond,Cont} = 4\pi \left(\delta + \frac{d_{eff,fm}}{2}\right) \int_{T_g}^{T_\delta} k_g dT \tag{4.7}$$

Table 4.1: *Constants in the thermal conductivity expression of N_2*

a_1	a_2	a_3	a_4
1.1885e-02	-2.8964e+00	5.5142e-01	-2.7292e-02

were k_{g} is the conduction coefficient for the surrounding gas. To calculate δ, the ratio of the limiting sphere radius to the effective radius ($r_{\mathrm{eff}} = d_{\mathrm{eff}}/2$) is given by [209]:

$$\frac{\delta + r_{eff}}{r_{eff}} = \frac{r_{eff}^2}{\lambda_\delta^2}\left(\frac{1}{5}\Lambda_1^5 - \frac{1}{3}\Lambda_2\Lambda_1^3 + \frac{2}{15}\Lambda_2^{5/2}\right) \tag{4.8}$$

with λ_δ being the mean free path of the gas molecules within the layer of δ thickness, and Λ_1 and Λ_2 are defined by the following expressions [208, 209]:

$$\Lambda_1 = 1 + \lambda_\delta / r_{eff}, \Lambda_2 = 1 + (\lambda_\delta / r_{eff})^2 \tag{4.9}$$

The mean free path is calculated by the expression suggested by Liu et al. [122]:

$$\lambda_\delta = \frac{k_g(T_\delta)}{f(T_\delta)p_g}[\gamma(T_\delta) - 1]\sqrt{\frac{\pi m_\delta T_\delta}{2k_B}} \tag{4.10}$$

With the Eucken factor [210] f:

$$f = (9\gamma - 5)/4 \tag{4.11}$$

The temperature dependence of the thermal conductivity of the surrounding gas is calculated using the approach available in CHEMKIN® [211], i.e a polynomial fit to the logarithm of k_g is estimated based on the standard kinetic theory expressions for the gaseous species:

$$ln(k_g) = \sum_{i=1}^{n} a_i \cdot ln(T)^k \tag{4.12}$$

In the current work a 4$^{\text{th}}$ order expression valid for N_2 was used and the related constants are provided in Table 4.1.

To account for the shielding effect, i.e. that the inner particles are "thermally" shielded by the outer particles from cold ambient gas molecules (so that they cool down slower), an effective diameter of the aggregate (d_{eff}) proposed by Liu et al. [121, 122] is used in the heat conduction term, Eq. 4.5.

$$d_{eff} = (n_p/k_0)^{1/D_f} d_{pp} \tag{4.13}$$

where the values of k_0 and D_{f} depend on the regime.

In the continuum regime, above constants are defined as:

$$k_{0,Cont} = 1.32 \tag{4.14}$$

$$D_{f,Cont} = 2.07 \tag{4.15}$$

In the free-molecular regime, they are dependent on the thermal accommodation coefficient, α_{T}:

$$k_{0,FM} = 1.04476 + 0.22329\alpha_T + 7.14286 \cdot 10^{-3}\alpha_T^2 \tag{4.16}$$

$$D_{f,FM} = 1.99345 + 0.30224\alpha_T - 0.11276\alpha_T^2 \tag{4.17}$$

It has to be mentioned that for n_{p} = 1 the term is not consistent, therefore in such a case $d_{\mathrm{eff}} = d_{\mathrm{pp}}$ is used. The non-uniform temperature distribution within an aggregate is neglected, i.e. the particles within an aggregate are considered to have the same temperature.

Vaporization

High or intermediate fluence causes intense evaporation, therefore the signal decay is strongly influenced by the volume loss from sublimation. The heat loss due to evaporation is determined by the enthalpy of the vaporized soot ($\Delta H_{\mathrm{v,s}}$):

$$\dot{\Omega}_{evap} = \frac{\Delta H_{v,s}}{M_{v,s}} J_{evap} \tag{4.18}$$

where $M_{\mathrm{v,s}}$ is the molar mass of the soot vapor.

The treatment of heat and mass loss varies between the different models significantly [212]. In the model provided by Hofmann et al. [120], the mass leaving the particle is proportional to the molecular flux defined by

$$J_{evap} = \frac{dm_p}{dt} = -\pi d_{pp}^2 N_{v,s} \frac{M_{v,s}}{N_A} \tag{4.19}$$

where $N_{\mathrm{v,s}}$ is the flux of molecules that leave the surface in the transition regime and N_A is the Avogadro constant.

$N_{\mathrm{v,s}}$ is calculated from the molecular flux in the free-molecular regime ($N_{\mathrm{Fm,s}}$) and the continuum regime ($N_{\mathrm{C,s}}$) [213]:

$$N_{v,s} = \left(\frac{1}{N_{Fm,s}} + \frac{1}{N_{C,s}} \right)^{-1} \tag{4.20}$$

where the fluxes are defined as:

$$N_{FM,s} = \beta \frac{p_{v,s}}{k_B T_p} \sqrt{\frac{R T_p}{2\pi M_{v,s}}} \tag{4.21}$$

and

$$N_{C,s} = 2 \frac{p_{v,s}}{k_B T_p} \frac{\Gamma_{v,s}}{d_{pp}} \tag{4.22}$$

with k_{B} being the Boltzmann constant, $p_{\mathrm{v,s}}$ the vapor pressure of the evaporating carbon species, β a constant in the range of [0,1] used to adjust the evaporation efficiency (generally set to 1 [120]), and $\Gamma_{\mathrm{v,s}}$ the diffusion coefficient of the soot vapor. The expression for the diffusion coefficient is given as follows [184]:

Table 4.2: *Coefficients for the polynomial expressions of the vapor pressure, the molecular mass of the vapor, enthalpy of vaporization and the molecular cross-section of the vapor in SI units [120]*

i	p_i	m_i	h_i	σ_i
0	-111.4	0.01718	205398	$1.8{\cdot}10^{-19}$
1	0.0906	$6.865{\cdot}10^{-7}$	736.6	$-1.857{\cdot}10^{-17}$
2	$-2.764{\cdot}10^{-5}$	$2.996{\cdot}10^{-9}$	-0.4071	$1.404{\cdot}10^{-15}$
3	$4.175{\cdot}10^{-9}$	$-8.595{\cdot}10^{-13}$	$1.199{\cdot}10^{-4}$	$-2.593{\cdot}10^{-14}$
4	$2.488{\cdot}10^{-9}$	$1.049{\cdot}10^{-16}$	$-1.795{\cdot}10^{-8}$	$2.075{\cdot}10^{-13}$
5	0	0	$1.072{\cdot}10^{-12}$	$-6.667{\cdot}10^{-13}$

$$\Gamma_{v,s} = \frac{f k_B T_p}{4 \Sigma_{v,s} p} \sqrt{\frac{R T_p}{\pi M_{v,s}}} \tag{4.23}$$

with $\Sigma_{v,s}$ being the molecular cross section of the vapor. The most relevant species at evaporation and their evaporation enthalpy dependence on temperature is discussed in [214]. The most important species is C_3, however, all species from C_1 to C_7 can be found in the vapor.

The vapor pressure, the molecular weight of the soot vapor, and the enthalpy of vaporization are defined based on a polynomial fit to experimental data performed by Smallwood et al. [215]:

$$p_{v,s} = exp\left(\sum_{i=0}^{5} p_i T_p^i \right) \tag{4.24}$$

$$M_{v,s} = \sum_{i=0}^{5} m_i T_p^i \tag{4.25}$$

$$\Delta H_{v,s} = \sum_{i=0}^{5} h_i T_p^i \tag{4.26}$$

The constants, p_i, m_i and h_i, are summarized in Table 4.2 along with the coefficients used by Hofmann [120] for the polynomial fit for the molecular cross-section performed on the experimental data of Michelsen [184]:

$$\Sigma_{v,s} = \sum_{i=0}^{5} \sigma_i T_p^i \tag{4.27}$$

In case of low fluence, the vaporization is negligible and this term can be neglected [85, 88, 121, 122, 184, 212].

Internal Energy

All above-described processes contribute to the internal energy change, which is given by

$$\dot{\Omega}_{int} = \frac{d(m_p c_{p,s} T_p)}{dt} \tag{4.28}$$

with T_{p} as particle temperature and $c_{\mathrm{p,s}}$ as the heat capacity [120].

Incandescence signal

Once the temperature decay of the particle is derived, the LII signal can be calculated from the Planck's law modified by the emissivity to correct for deviations from the perfect blackbody radiation [184]:

$$S_{LII} = 2\pi^2 hc^2 d_{pp}^2 \int_0^\infty \frac{\epsilon(\lambda)}{\lambda^5 [exp\big(hc/\lambda k_B T_P\big) - 1]} d\lambda \tag{4.29}$$

where h is the Planck constant and ϵ is the spectral emission of soot, which is derived from the expression [184]:

$$\epsilon = \frac{4C_{abs}}{\pi d_{pp}^2} = \frac{4\pi d_{pp} E(m)}{\lambda_{det}} \tag{4.30}$$

To calculate the detected incandescence signal ($S_{\mathrm{LII,det}}$), the detection limits of the bandpass filter, λ_1 and λ_2, and the spectral response function of the detection system (Ω_{res}) have to be considered:

$$S_{LII,det} = 2\pi^2 hc^2 d_{pp}^2 \int_{\lambda_1}^{\lambda_2} \frac{\Omega_{res}(\lambda)\epsilon(\lambda)}{\lambda^5 [exp\big(hc/\lambda k_B T_P\big) - 1]} d\lambda \tag{4.31}$$

In general, the LII signal decay is approximated by an exponential function [182], or sometimes a double exponential function [84, 187, 216]:

$$S_{LII} = S_1 \cdot exp\left(\frac{-t}{\tau_1}\right) + S_2 \cdot exp\left(\frac{-t}{\tau_2}\right) \tag{4.32}$$

with S_1 and S_2 being the pre-exponential factors, τ_1 and τ_2 the exponential decay times. It has to be noticed that this approximation may introduce errors. As the primary particle size is related to the signal decay speed and not to its initial peak value, the evaluation is generally performed by considering the signal normalized by the initial peak value ($S_{\mathrm{LII,peak}}$):

$$S_{LII,n}(t) = \frac{S_{LII}(t)}{S_{LII,peak}} \tag{4.33}$$

4.4 Uncertainties at PPSD validation by TiRe-LII[4]

On the one hand, the reconstruction of the LII signal is known to be strongly dependent on the model used to describe the source terms in the mass and the energy balance equations as exhaustively discussed by Schulz et al. [217] and Michelsen et al. [212]. On the other hand, most of the models rely on the same input quantities, summarized in Table 4.3, which are not necessarily known. Many

[4] content has been published in A.L. Bodor, A. Cuoci, T. Faravelli, Towards a more consistent validation of numerical modeling of primary particle diameters in sooting flames, Submitted to Applied Physcs B. (2019) [196]

of these variables are properties of the experimental equipment ("Equipment"), some of them are properties of the gaseous field around the investigated soot particles ("Ambient"), and numerous of them are characteristics of the soot particles themselves ("Soot"). The uncertainty related to the parameters of the equipment, like the fluence, plane width, and laser temporal profile, cannot be recovered from the numerical simulations, therefore they are not discussed here. The variables potentially determined by measurements are marked by "M". However, these measurements may possibly introduce additional errors and require additional devices and/or post-processing. Some parameters are frequently assumed ("As") as their determination by experiments would require significant extra effort. The parameters available in the numerical simulations are marked by "N". The role of each parameter in the signal modeling was explained in Section 4.3.

Equipment	
Laser wavelength (λ)	
Temporal beam profile or FWHM	
Laser fluence (J)	
Bandpass wavelengths (λ_1, λ_2)	
Ambient	
Pressure (p)	As, N
Temperature (T)	As, M, N
Molecular weight (M_g)	As, N
Mass accommodation coefficient (β)	As
Soot	
Soot absorption function ($E(m)$)	As, M
PPSD shape	As, M, N
Number of primary particles in the aggregate (n_p)	As, M, N
Thermal accommodation coefficient (α_T)	As, M

Table 4.3: *Required input parameters*

Five of these parameters are related to variables that are known from the numerical simulations (the pressure (p), the temperature (T), the molecular weight of gas phase (M_g), the PPSD shape and the number of primary particles in the aggregate (n_p)). Therefore, the related errors and/or complementary measurements can be then potentially avoided when the validation is performed by comparing the synthesized and the experimental LII signals, instead of comparing d_pp or PPSD.

In the following, the effect of the uncertainties introduced by these parameters on d_pp is discussed. After the overview of the earlier performed investigations, a sensitivity study is presented to complete the scenario. By highlighting the potential errors that can be avoided with the proposed forward approach the interest in the novel validation method can be assessed *a priori*.

Soot absorption coefficient

The absorption coefficient ($E(m)$) influences the ratio of the total and absorbed laser beam energy, through the absorption cross-section (Eq. 4.3 and 4.4). Therefore, it affects the peak temperature of the particle. Furthermore, it influences the intensity of the incandescence signal through the spectral emission

of soot (Eq. 4.30). However, it does not have a direct impact on the temperature decay of the particle. The absorption coefficient is wavelength dependent and it is a function of the optical properties of the material, i.e. the refractive index (m). Therefore, it is not surprising that a wide discrepancy can be observed in the $E(m)$ values reported in the literature, which was overviewed in [212, 218]. The wavelength-dependency of $E(m)$ was investigated by several researchers [200, 219, 220]. However, in general, $E(m)$ is assumed to be constant for a wide range of wavelengths above 500 nm [221]. Such an assumption was confirmed by several studies [218, 222–224].

Several researchers found that $E(m)$ changes with the height above the burner in the flame [88, 193, 219, 225, 226], even while using the same laser wavelength. Bladh et al. [88] investigated a premixed flame with a laser of 1064 nm wavelength and found that $E(m)$ increases from $\sim$0.2 to $\sim$0.45 with the HAB. However, they also highlighted the significant uncertainty of the values due to soot particle density, and specific heat assumption.

In general, soot matures with the HAB, consequently with the residence time. Therefore, the change in the absorption coefficient can be related to the the change in the refractive index of soot particles, as already highlighted in [225, 227]. Cleon et al. [193] and Migliorini et al. [219] presented the HAB dependency of the absorption coefficient normalized by the $E(m)$ for 1064 nm value. The wavelength-dependency of $E(m)$ was found to vary with HAB especially for small wavelengths.

In several studies two main classes are distinguished based on the wavelength absorption, the nanoparticles of organic carbon absorbing up to $\sim$350 nm and soot particles whose absorption is down to the visible range [228–230]. For the investigation of the soot particle refraction index (m = n - ki) various values can be found in the literature. The values of early studies are summarized by Mulholland et al. [231] highlighting that even for a given wavelength (633 nm) n and k may vary in the range of [1.53,1.9] and [0.38,0.8] respectively. In this work they found that the good agreement with the soot aggregate absorption coefficient would require an index of m = 1.55 - 0.8i ($E(m)$ = 0.366). In a more recent work by William et al. [50] measurements at 635 nm imply n = 1.75 and k = 1.03 ($E(m)$ = 0.372), which is in good agreement with the above mentioned study. They also highlighted that numerous refraction indices found in the literature do not provide a reasonable absorption coefficient. However, their values do not explain the variation of $E(m)$ with the HAB observed by the measurements.

Regarding the difference between nanoparticles and soot particles, n and k in the UV range at 266 nm for nanoparticles in non-sooting flames were determined as n = 1.35 $\pm$ 0.05 and k = 0.09 $\pm$ 0.03 ($E(m)$ = 0.05) by Cerece et al. [232]. At the same wavelength for soot particles n = 1.4 and k = 0.75 ($E(m)$ = 0.395) was found by Chang and Charalampopoulos [233], resulting in a factor of 8 in the soot absorption coefficient. This is in agreement with the observations that the absorption coefficient increases with the HAB. However, a comprehensive theory and relation between soot maturity and refraction index is currently not available. Once the exact relation to the H/C ratio and the particle size is determined, the varying $E(m)$ value of the soot particles this two parameters can be included

further improving the reliability of the forward validation method.

The change in the temperature decay of the particle with the variation of $E(m)$ was presented by Snelling et al. [200] but not analyzed in detail. Even if $E(m)$ is characterized by high uncertainties, the work of Daun et al. [185] showed that most of the LII models are insensitive to $E(m)$ while assuming that two-color pyrometry is used. More specifically, in this work, it has been shown that a variation of ± 0.1 from the reference value ($E(m) = 0.3$) does not lead to significant change in the retrieved PPSD, except when using the model of Lehre et al. [86]. If the peak temperature is estimated by including the laser-excitation term in Eq. 4.1, which is necessary if only one wavelength is measured in the probe volume (not measured directly with two-color pyrometry), uncertainties in $E(m)$ may introduce significant errors in the peak temperature and consequently the retrieved PPSD [185].

Mass accommodation coefficient

The mass accommodation coefficient is a key parameter for the description of particle sublimation (Eq. 4.21). In the literature, this quantity is characterized by a high uncertainty: its value varies between 0.5 and 1 [212]. To avoid the possible errors due to an inaccurate estimation of the mass accommodation coefficient, recent experimental studies suggest to work with low laser fluence so that the sublimation phenomenon is negligible compared to the other processes occurring after the interaction of the laser with the particles [85, 88, 121, 122, 184, 212]. Uncertainties on β are therefore not considered in this work.

Ambient temperature

Several studies concern the impact of the uncertainty of the gas phase temperature (T_{g}) on the experimental estimation of d_{pp} from the Tire-LII signal. Sun et al. [234] demonstrated that a variation of ± 200 K from 1700 K leads to errors on the value d_{pp} of ± 3 nm for d_{pp} = 15 nm and ± 5 nm for d_{pp} = 40 nm. The significant impact of the flame temperature on the derived primary particle size was presented also by Will et al. [235]. For a variation of ± 180 K from 1800 K ($\pm 10\%$) the relative error of the diameter was about ± 6 nm ($\pm 30\%$) and ± 8 nm ($\pm 20\%$) for a particle of 20 and 40 nm, respectively. Cenker et al. [89] observed a deviation up to $\pm 20\%$ in the primary particle diameter for the temperature variation in the range of $\pm$ 200 K.

Daun et al. [185] quantified the difference between two lognormal PPSDs derived from the same LII signal when varying the temperature around its exact value. The measure of difference was the Cramér-von Mises (CVM) goodness-of-fit parameter, which was defined as the area contained between the recovered and the exact particle size cumulative distribution functions, i.e. the perfect agreement between the PPSDs results a zero CVM value. The CVM parameter for the temperature variation of ± 30 K from the nominal 1700 K varied between ~ 0.1 to ~ 0.43, depending on the model used for the LII signal calculation [185]. [5]

Experimental uncertainties on temperature depend both on the retained experimental technique as well as the investigated configuration with an error that can

[5] As an example, the CVM parameter is 0.658 when comparing a lognormal distribution characterized by a geometrical mean d_g and a standard deviation σ_g $\{d_g,\sigma_g\}$ = {30 nm, 1.25} and a lognormal distribution with $\{d_g,\sigma_g\}$ = {26 nm, 1.23} of [185].

reach ± 200 K [84, 85, 236–242]. Even worse, the temperature value is often assumed when extracting PPSD information from TiRe-LII signal [84, 243, 244] greatly increasing the error bars on d_{pp}. On the contrary, the numerical simulations provide the gas phase temperature in the whole domain, so that uncertainty on this quantity can be reduced by numerically reconstructing the LII signal and comparing it to the experimental one (supposing that the numerical models have been previously validated).

Thermal-accommodation coefficient

The thermal-accommodation coefficient is expected to depend on the soot maturity based on recent experimental [85, 245] and theoretical studies [246–248]. The roughening and the increased hydrogenation of the particle surface enhance the heat exchange between the gas phase and the particle surface [249, 250] and, consequently, the thermal-accommodation coefficient. A relation between α_{T}, the temperature, and the surface hydrogenation was derived by Michelsen and coworkers [245]. Unfortunately, this relation was verified on a limited set of data, so that it cannot be considered as a general rule [205]. Thermal accommodation coefficients in a premixed ethylene flame were determined for different HABs by Bladh et al. [85], and values of 0.5 to 0.61 were retrieved (increasing with the HAB). For an ethylene coflow diffusion flame a value of 0.37 was determined by Snelling et al. [200]. The difference in the particle properties in diffusion and premixed flames may point in the direction of the intense dependence on the particle's chemical characteristics and α_{T}. Furthermore, because of the temperature uncertainty of 5% associated to the experimental determination, a ±7-10% uncertainty of α_{T} may originate [85]. In the literature, values from 0.23 to 0.9 are used for α_T [212]. The wrong assumption can lead to significant inaccuracies at the estimation of the d_{pp}, since a variation of just ±0.05 can result in significantly different PPSD (the CVM goodness parameter was above 1 for all simulation models [185]). As long as the connection between α_{T} and soot maturity is not established, the uncertainty related to this parameter is not avoidable. However, once this relation is established, the LII signal reconstruction from numerical results can potentially overcome the issue.

Number of primary particles in the aggregate

In most of the cases self-standing particles are assumed for the TiRe-LII signal evaluation [84, 85, 88, 183, 234], even if the cooling process strongly depends on the number of primary particles in the aggregate (n_{p}) due to the shielding effect [122, 202, 205, 216], as discussed in Section 4.3. To account for this phenomenon when deriving d_{pp} from experimental LII signal, the exact determination of n_{p} is needed. This would require the usage of TEM, which results in the loss of advantages gained by using the TiRe-LII technique.

Accounting for n_{p} may have a strong impact on the results. As an example, the reevaluation of the measured TiRe-LII signal with n_p = 100 instead of n_{p} = 1 by Bladh et al. [88] led to the drop of the derived mean d_{pp} by ∼30%. The same exercise was performed by Sun et al. [234], where the difference between the two derived diameters is more than 30% (29 nm for n_p = 1 and 19 nm for n_{p} = 100). As long as the LII experiment is not accompanied by TEM measurements, the

aggregate structure is unknown, leading to uncertainties on n_{p} and consequently on the derived d_{pp}. On the contrary, the numerical prediction provides information about the number of primary particles in the aggregate, so that the LII signal reconstruction can account for the phenomenon. In the following section it will be shown, that even if the exact value of n_{p} is not known, the prediction of the LII signal improves significantly if the aggregate structure is considered ($n_{\mathrm{p}} > 1$). Therefore, as the numerical results are expected to indicate the presence of aggregates, the related uncertainty is expected to be reduced.

PPSD shape

The presumed PPSD shape is one of the most relevant uncertainties. In many cases, a monodisperse distribution is assumed for the sake of simplicity [85, 88, 183]. However, primary particle distribution is often observed to be lognormal [77,85,86]. A lognormal distribution can be characterized by the geometric mean diameter (d_{g}) - which is equal to the count median diameter (d_{CMD}) - and the variance (σ_{g}). When assuming a monodisperse distribution, all particles have the same d_{mono} diameter. In case of a lognormal distribution, the relation between a monodisperse equivalent mean particle diameter (obtained by preserving the total volume and primary particle number but assuming monodisperse distribution) and d_{g} is related to σ_{g}, as depicted in Figure 4.3. Depending on the σ_{g}, the ratio of the two characteristic diameters can vary significantly.

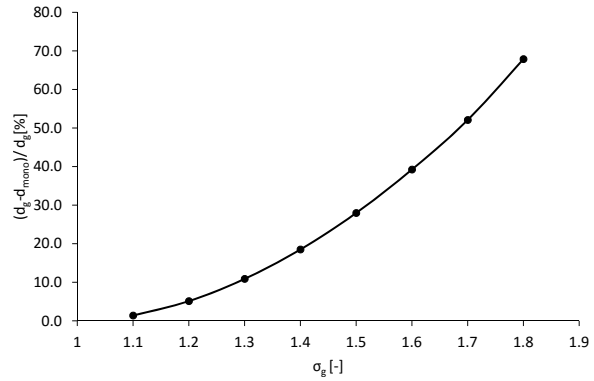

Figure 4.3: *Relation between monodisperse equivalent mean particle diameter (d_{mono}) and d_g for lognormal PPSD distribution*

An exhaustive analysis was performed by Cenker et al. [89] on the possible d_{mono} values retrieved from LII signals constructed from a lognormal distribution with a wide range of $\{d_{\mathrm{g}},\sigma_{\mathrm{g}}\}$ pairs (at 1750 K, 1 bar and n_p = 1). In this work, the significant difference between d_{mono} and d_{g} extracted from the same signal was presented, e.g. for $\{d_{\mathrm{g}},\sigma_{\mathrm{g}}\}$ = $\sim${30 nm,1.4} the resultant $d_{\mathrm{mono}} \sim$ was 40 nm. Sun et al. [234] also reevaluated a typical TiRe-LII signal with both monodisperse and lognormal distribution assumptions (at 1700 K, 1 bar and n_p = 100). The resultant characteristic diameters were d_{mono} = 19 nm and d_{g} = 15 nm with σ_{g} = 1.25. However, is important to mention that in both investigations [89, 234] the diameter derived by assuming monodispersity from the LII signal does not coincide with the monodisperse equivalent mean particle diameter of the lognormal distri-

bution[6], which is 35.5 nm for $\{d_g,\sigma_g\}$ = {30 nm,1.4} and 16.2 nm for $\{d_g,\sigma_g\}$ = {15 nm,1.25}. This also means that even if the numerical PPSD is correct, when the equivalent d_{mono} is compared to the one derived from the experimental signal, a disagreement is found.

Franzelli et al. [84] evaluated the measured LII signals of a series of coflow laminar flames with both monodisperse and lognormal PPSD assumption. In this work, besides d_{mono}, the mean primary particle diameter defined as d_{amean} = exp (lnd_g + (lnσ_g)^2 / 2) (which is the arithmetic mean diameter for lognormal distributions) is presented. While d_{amean} varied in the range of 10 to 65 nm, d_{mono} reached up to $\sim$ 90 nm. This meant a difference as high as $\sim$30% for the heavily sooting flame. All previously mentioned works enlighten that different PPSD shape assumptions can lead to very different characteristic diameters.

Dankers et al. [187] suggested to derive two characteristic LII signal decay times, $\tau_1(\Delta t_1)$ and $\tau_2(\Delta t_2)$ for two subsequent measurement time intervals (Δt_1 and Δt_2). In this work, it was demonstrated that for lognormal distribution the correlation between $\{\tau_1,\tau_2\}$ and $\{d_g, \sigma_g\}$ is unambiguous. However, Daun et al. [185] showed that - even when the lognormal PPSD shape is valid - entirely different $\{d_g,\sigma_g\}$ pairs might almost (within the experimental error) minimize the objective function of the iterative process, i.e. various PPSDs can be considered as a good match to the experimental signal. Furthermore, it has been also shown that obtaining lognormal PPSD shape cannot be considered as a general rule [25, 77, 87–90], so that no shape could be presumed with confidence even if this is commonly done when post-processing TiRe-LII data.

Smallest detected diameter

Once the d_{pp} value is obtained by post-processing the TiRe-LII signal, the comparison with the numerical results may be affected by an additional parameter, i.e. the smallest particle that can emit an LII signal. Only recently, the study of Betrancourt et al. [186] pointed out that soot particles as small as 2 nm may absorb laser energy and emit LII signal. However, even larger particles may not emit a signal detectable by the detection system [191]. This might be related to the fact that the optical properties of soot particles may vary. Therefore, with TiRe-LII it is not possible to identify bimodality [244] and the exact value of the smallest detectable diameter ($d_{det,min}$) is still uncertain.

Even if such a piece of information is not relevant when comparing experimental to numerical results in terms of soot volume fraction (since the contribution of small particles to the LII signal in the presence of large particles is negligible [217]), it can greatly affect the validation for d_{pp} using the inverse method as it will be discussed in Section 5.4 and 6.4. Information about $d_{det,min}$ value is especially important when capturing bimodal PPSD, where a large number of particles in the range of 2-5 nm are expected [38, 74, 103, 154, 251], or when a transition from a unimodal to a bimodal PPSD occurs.

[6] the diameter calculated from the PPSD by assuming monodispersity and retaining the soot volume fraction and primary particle number

4.4.1 Sensitivity study

In order to further investigate the impact of the different assumptions, first a reference signal is produced with a set of base parameters, then the parameters are varied and the effect on the LII signal decay is evaluated. The signals are calculated based on the model described in Section 4.3. Where not stated differently, monodisperse distributions with four different d_{pp} values (5, 15, 25, and 35 nm) are investigated and the base set of parameters ($\bar{\Phi}_0$) represent the most frequently used assumptions:

$$\bar{\Phi}_0 = (n_{p,0}, T_0, M_{g,0}, p_0, E(m)_0, \alpha_{T,0}) \tag{4.34}$$

where $n_{\mathrm{p,0}}$ = 1, T_0 = 1700 K, $M_{\mathrm{g,0}}$ = 28 kg/kmol and p_0 = 1 bar. The parameters not recoverable from the numerical simulation were chosen as $\alpha_{T,0}$ = 0.37 and $E(m)_0$ = 0.3. As nowadays the general approach is to work with low fluence of the laser, so that the evaporation can be neglected, the fluence was set to 0.13 J/cm^2 and evaporation was neglected. The parameters of the optical system were set as follows: laser wavelength = 1064 nm, shot duration = 11 ns, bandpass filter = 575$\pm$16 nm.

Cenker et al. [89] pointed out that, while for monodisperse distribution the LII signal decay can be approximated with an exponential function, for polydisperse distributions a double-exponential (Eq. 4.32) fit is more suitable. The latter approach is widely used in recent studies [84, 89, 187, 216, 243]. In order to quantify the differences between the LII signals, the effect on the exponential fit parameters will be considered.

In the following, to analyze the impact of the parameter uncertainties, the behavior of the decay time, $\tau_{d_{\mathrm{pp}}}$ calculated for a given d_{pp} value will be evaluated by varying some of the parameters of $\bar{\Phi} = (n_{\mathrm{p}}, T, M_{\mathrm{g}}, p)$. $\tau_{0,d_{\mathrm{pp}}}$ corresponds to the decay time for a given d_{pp} value when all parameters are provided by $\bar{\Phi}_0$. The variation of the parameters will lead to the deviation of τ from $\tau_{0,d_{\mathrm{pp}}}$, potentially overlapping with the decay time of a different $\hat{d_{\mathrm{pp}}}$, $\tau_{0,\hat{d_{\mathrm{pp}}}}$. This means that for the decay time extracted from the experiment ($\tau = \tau_{0,\hat{d_{\mathrm{pp}}}}$), $\hat{d_{\mathrm{pp}}}$ will be recovered instead of d_{pp}. Furthermore, even if the PPSD is correctly captured, it might be proven invalid.

The relative error in the decay time related to a modified set of parameters ($\bar{\Phi}$) is also calculated as:

$$\frac{\Delta\tau}{\tau} = \frac{\tau(\bar{\Phi}) - \tau(\bar{\Phi}_0)}{\tau(\bar{\Phi}_0)} \tag{4.35}$$

Pressure

To our knowledge, the effect of inaccuracies of the pressure value on the LII signal has not been explored in the literature. The pressure influences the heat conduction between the soot particle and the gas phase through Eq. 4.5 and 4.10 and the evaporation through Eq. 4.23. A sensitivity analysis is here performed by applying a variation of $\pm$2.5% and $\pm$5% respect to 1 bar. To see the potential combined effect of temperature and pressure variations, the temperature is also

modified with ±50 K and ±150 K. In Figure 4.7, τ is shown for the various conditions. To interpret the results, it is important to understand how much results from different d_{pp} values may overlap in the range of the investigated pressure and temperature fluctuations.

It can be observed from Figure 4.4 that for small d_{pp}, the decay time does not vary significantly with the pressure. On the contrary, for higher values of d_{pp}, τ becomes more sensitive to the pressure (and temperature too). This makes more difficult to recognize the d_{pp} value originating the incandescence signal, which results a potentially inaccurate estimation of d_{pp}. The introduced relative error ($\Delta\tau/\tau$) due to temperature variation does not depend significantly on d_{pp} and p in this range. However, the absolute error becomes larger with the diameter.

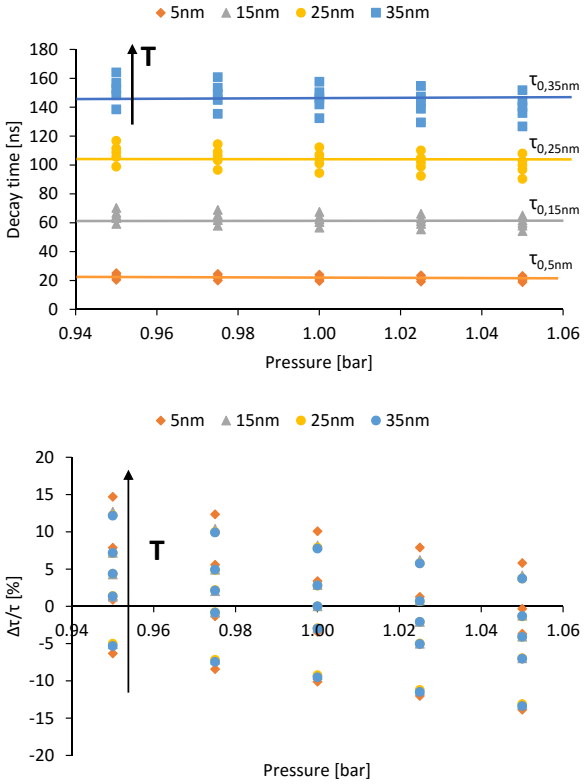

Figure 4.4: *Decay time (a) and its relative error (b) as a function of pressure for four different d_{pp} (5, 15, 25 and 35 nm) and for four different temperatures (1550, 1650, 1700, 1750 and 1850 K)*

Nowadays, pressure measurement can be carried out with high accuracy, especially for constant pressure burners, so that small errors are expected from pressure uncertainties at atmospheric pressure. To perform the sensitivity study at elevated pressures would be of interest due to its practical applications. However, the signal decay at elevated pressure (e.g. at 10 and 50 bar) is not exponential, so that a different parameter is required to address the sensitivity. Therefore, an analysis using a different parameter is proposed as future work. Computational simulations give access to the pressure value so that with the novel approach the related uncertainties can be reduced even for complex flames, where pressure measurement may be more difficult to carry out.

Soot absorption coefficient

The LII signal depends both on the laser beam wavelength and the soot refractive index through the soot absorption coefficient. Therefore, these parameters are not separately perturbed, only the $E(m)$ is varied over a wide range (between 0.1 to 1). The soot absorption coefficient does not impact directly the decay time, only through the peak temperature reached by the particle. This is important, as the various sized and matured particles might have different refraction indices, therefore different soot absorption coefficients, which may again bias the derived mean primary particle size when a constant value is assumed. The results showed no sensitivity to the soot absorption coefficient when the evaporation was neglected. However, when evaporation was included, the decay time varied with the $E(m)$ as shown in Figure 4.5. The decay time is especially sensitive in the region of the generally observed $E(m)$ values for the soot particles, i.e. between 0.1 to 0.4. This means that the higher peak temperature caused by the larger absorption can lead to a more intense evaporation, however, if low enough fluence is used the related error in τ is marginal.

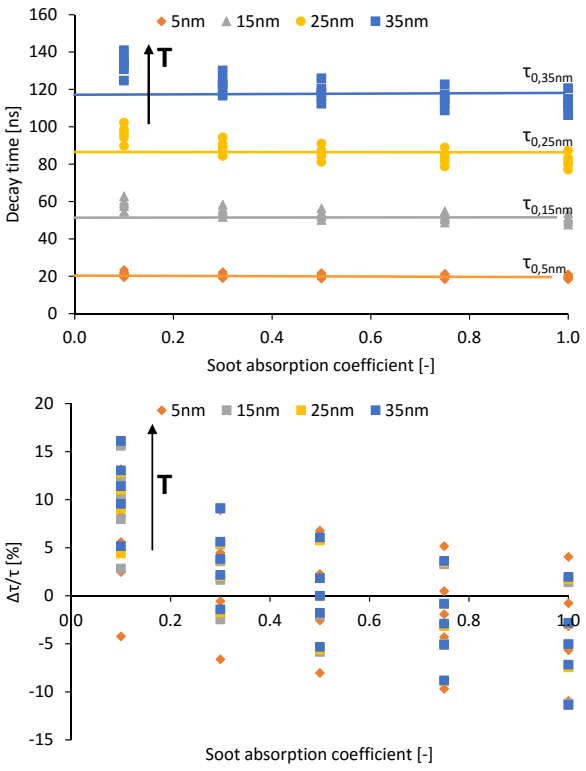

Figure 4.5: *Decay time (a) and its relative error (b) as a function of the soot absorption coefficient for four different d_{pp} (5, 15, 25 and 35 nm) and four different temperatures (1550, 1650, 1700, 1750 and 1850 K)*

Thermal accommodation coefficient

In Figure 4.6, the sensitivity to the thermal accommodation factor is presented (for clearer presentation, instead of 0.37, $\alpha_{T,0}$ = 0.4 was considered). The variation in the decay time is enormous, the relative errors are similar for the different

diameters. τ varies with $\pm 50\%$ for the variation of ± 0.2 so that a particle with d_{pp} = 15 nm and α_{T} = 0.2 would be detected as a 25 nm diameter particle. Unfortunately, as long as the relation between the thermal accommodation coefficient and the chemical properties of the soot particle is not established, this error can not be avoided. However, it indicates the significant potential of the forward method.

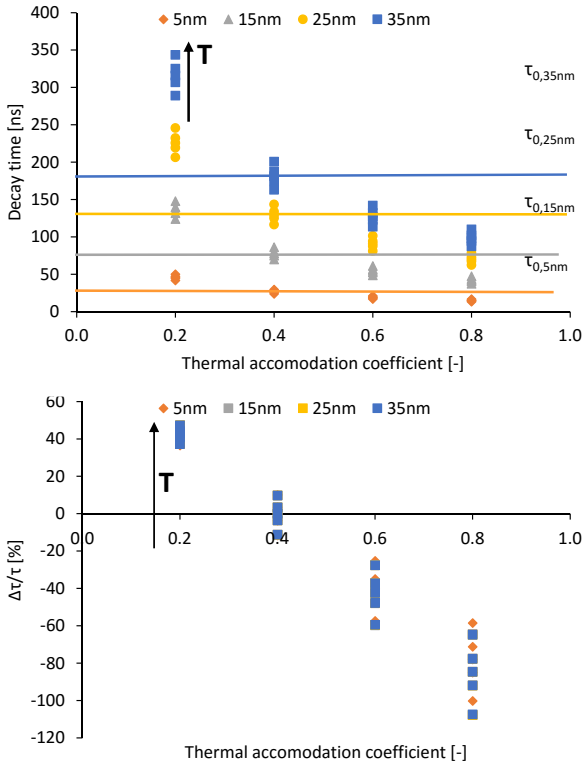

Figure 4.6: *Decay time (a) and its relative error (b) as a function of the thermal accommodation coefficient for four different d_{pp} (5, 15, 25 and 35 nm) and four different temperatures (1550, 1650, 1700, 1750 and 1850 K)*

Molecular weight

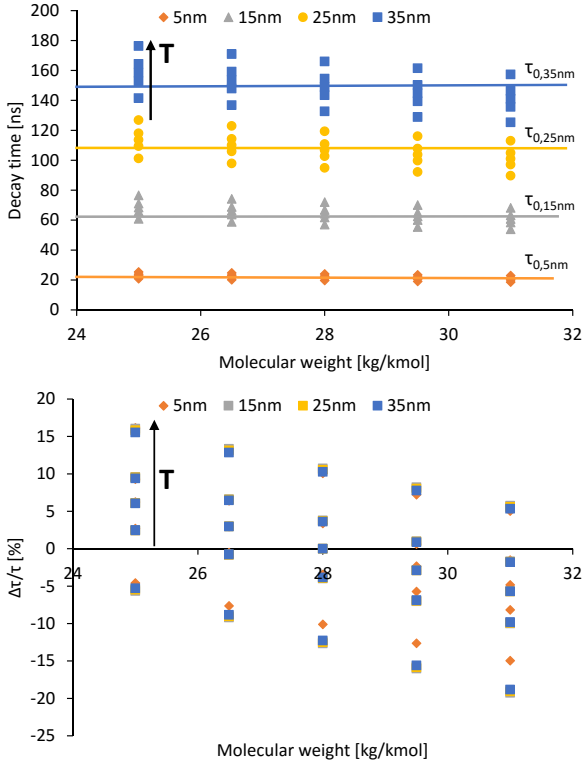

Figure 4.7: *Decay time (a) and its relative error (b) as a function of the molecular weight for four different d_{pp} (5, 15, 25 and 35 nm) and four different temperatures (1550, 1650, 1700, 1750 and 1850 K)*

To experimentally evaluate the gas phase molecular weight (M_g), information on the local composition is required. Many species can be measured today with high accuracy. However, to access these quantities, extra experimental equipments and post-processing are needed. Even when using ethylene as fuel (whose molecular weight is similar to nitrogen), the gas phase molecular weight might differ significantly from the one of air in the sooty region since soot is accompanied by several high molecular weight gas phase species, like heavy PAHs, but also lighter species as hydrogen, water vapor or acetylene. Therefore, the generally used approach, i.e. assuming air properties [84, 85, 88], might be inaccurate. As an example, the M_g value has been extracted from numerical simulations of sooting flames investigated in this work. For the premixed ethylene laminar flame with an equivalence ratio of 2.1 and the coflow ethylene laminar flames with various ethylene content in the fuel stream (32, 40, 60 and 80 % volumetric ratio), the M_g value varied between 25 to 30 kg/kmol in the sooty region, whereas the general assumption is M_g = 28 kg/kmol.

The sensitivity study presented in Figure 4.7 reveals that though other parameters (like n_p or α_T) cause higher variations in the decay time, i.e. higher uncertainties, the error introduced by an inaccurate M_g estimation is not negligible. The error of τ for the variation of M_g with $\pm$ 3 kg/kmol without temperature variation can reach up to $\pm$5%. In addition, when the temperature is also varied, the error can reach $\pm$10 % and $\pm$17 % for $\pm$50 K and $\pm$150 K, respectively. The relative error due to temperature variation does not show strong dependency

on the d_{pp} and M_{g} in this range, however, the absolute error of the decay time becomes larger with the diameter.

Since the gas phase molecular weight is one of the base variables of numerical simulations, the novel approach can remove the uncertainty related to M_{g} without any additional cost compared to the classical validation strategy.

Thermal conductivity

The thermal conductivity of the surrounding gas and the gas in the δ-thick layer used in the model of Mc Coy and Cha [203] is determined by Eq. 4.12. The experimental parameters result in an uncertainty of the thermal conductivity, however, the sensitivity analysis performed on k_g showed, that as long as the parameters do not result in a change of k_g larger than a factor of $10^{\pm 4}$ the decay time does not show a noticeable variation.

Number of primary particles in the aggregate

To examine the sensitivity to the number of primary particles in the aggregate, n_{p} was varied from 1 to 100 (1, 5, 30, 60 and 100) along with the temperature (1550, 1650, 1700, 1750 and 1850 K). In Figure 4.8 the decay times of the exponential fit and $\Delta\tau/\tau$ are presented.

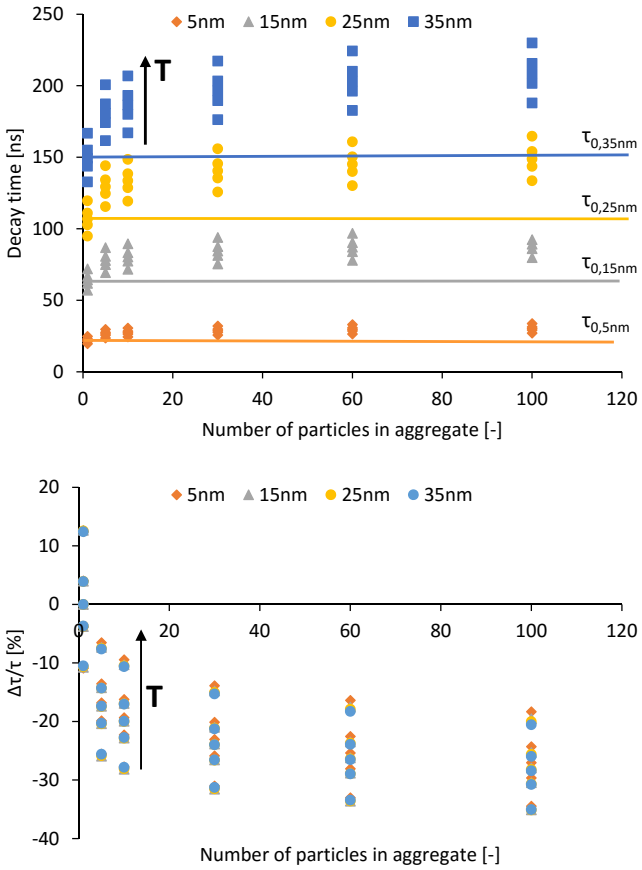

Figure 4.8: *Decay time (a) and its relative error (b) as a function of n_p four different for four different d_{pp} (5, 15, 25 and 35 nm) each with four different temperature values (1550, 1650, 1700, 1750 and 1850 K)*

For all the considered diameters, the decay time drastically changes between a single particle and an aggregate even when it is characterized by a small number of primary particles. The relative error reaches 20% already at n_{p} = 10. Whereas the difference in τ between n_{p} = 60 and n_p = 100 is less relevant compared the difference between n_{p} = 1 and n_{p} = 10.

When the aggregate nature of the particle is not considered a smaller τ, i.e. a faster signal decay, is observed in agreement with results from the literature [121]. This will imply an over-prediction of the d_{pp} value since for a given decay time, for example τ = 150 ns, a larger diameter, 35 nm is estimated when n_{p} = 1 whereas for n_{p} = 100 d_{pp} = 25 nm.

It has to be mentioned that the difference between the τ derived from the single-exponential fit and the τ_1 (with $S_1 > S_2$) of the double-exponential fit reached 5-10% for the hight temperature cases (1750 and 1850 K). However the main conclusions regarding the importance of the n_{p} is not affected by this.

Overall, it should be noticed that the error introduced by an inaccurate prediction of n_{p} is moderate compared to the one caused by completely neglecting the aggregate nature. Therefore, if the presence of aggregates is expected, despite the lack of knowledge on the exact n_{p}, an assumption of n_{p} in the range of 30 to 50 may be retained since the introduced error will be lower than considering n_{p} = 1. Furthermore, by reconstructing the LII signal from a numerical simulation that provides information about the aggregate nature of the particle, the accuracy of the validation can be improved compared to the traditional validation method.

In case the numerically obtained value of the above-listed input parameters provides a better prediction compared to the assumption made in the experiment, the reliability of the validation is expected to improve by using the numerically obtained values of these parameters. For the flames investigated in this work, an additional validation will be carried out with the novel approach, as many of the parameters in Table 4.3 are expected to be better predicted by the numerical model than the assumption used at the measurement evaluation.

PPSD shape

The dependence of the experimentally derived characteristic diameter on the assumed PPSD shape was widely investigated in earlier studies, as it was presented in the previous section. However, when validating a numerical model in respect to the primary particle size and number, it is of interest to know if d_{mono}, i.e. the total number of primary particles, can be confirmed even if the shape of the PPSD is not captured. For this reason, three different distributions with the same monodisperse equivalent mean particle diameter were used to reconstruct the LII signal: 1) A lognormal distribution with $\sigma_{\mathrm{g}} = 1.2$, $d_{\mathrm{g}} = 13.05$ nm; 2) a bimodal distribution with the second mode being lognormal ($\sigma_{\mathrm{g}} = 1.2$, $d_{\mathrm{g}} = 15$ nm); 3) a monodisperse assumption with the diameter d_{mono} = 13.7 nm. The PPSDs are presented in Figure 4.9, where the d_{mono} is marked by a black line. The LII signals obtained with the base set of parameters ($\bar{\Phi}_0$) are plotted in Figure 4.10 along with the parameters of the double fit (Eq. 4.32). The LII signals are normalized by their peak value.

The prefactor of the second exponential function (S_2) is almost two orders of magnitude smaller than S_1 for the monodisperse distribution, i.e. the LII signal

decay is similar to a single-exponential function. On the contrary, S_2 is only one order of magnitude smaller than S_1 for the lognormal distribution, so that the second exponential becomes more significant, which is in agreement with earlier observations [89,187]. The second decay time, τ_2, is almost two times larger than τ_1 for this distribution.

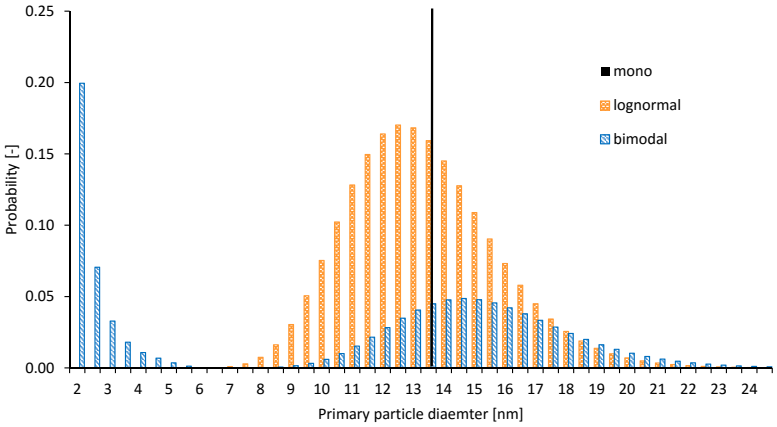

Figure 4.9: *Lognormal and bimodal PPSD*

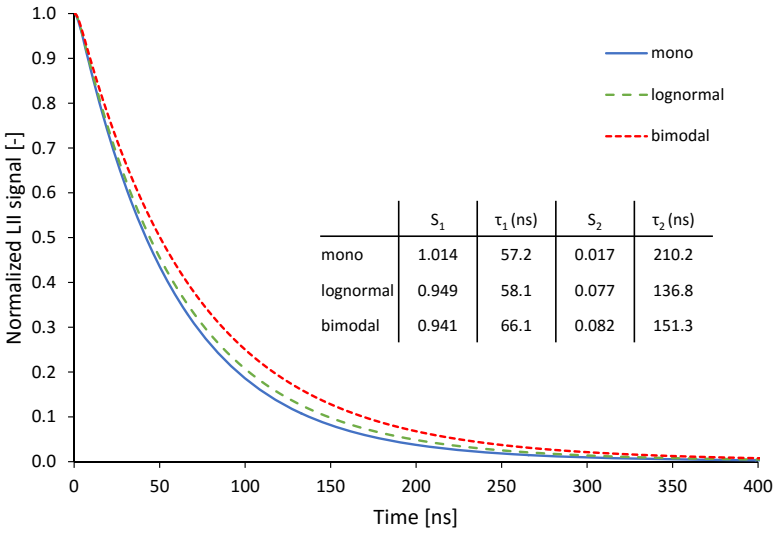

Figure 4.10: *Resultant LII signals for the PPSDs of Figure 4.9 with the double exponential fit pre-exponential factors and decay times*

Similarly, the S_2 value of the bimodal distribution is not negligible, and τ_2 further increases compared to its value in the lognormal case. Despite the huge amount of very small particles, the bimodal distribution provides the slowest LII signal. The incandescence from first mode particles is negligible compared to the one of the second mode and the relative importance of large particles ($d_{\mathrm{pp}} > 18nm$) compared to medium size particles ($12 < d_{\mathrm{pp}} < 18nm$) is higher. Therefore, the signal seems to be originated from a larger d_{pp}. The LII signal decay from the monodisperse population is slower compared to the lognormal (see Figure 4.10) in agreement with the observations of Sun et al. [234]. This

means that deriving the characteristic diameter with monodisperse distribution assumption does not provide the monodisperse equivalent mean particle diameter of a lognormal or a bimodal distribution, as discussed before regarding the *PPSD shape*.

This demonstrates that when comparing the d_{mono} derived from the numerical PPSD to the experimental one, very different numerical PPSDs may potentially be incorrectly give a good agreement. Furthermore, a well captured PPSD shape might be mistakenly not validated, when the calculated d_{mono} is compared to the one derived from the TiRe-LII. The LII signal can be synthesized from the numerical PPSD and compared to the experimental one, additionally validating or disproving the numerical results.

CHAPTER 5

Premixed Laminar Flame

In this chapter the first investigated flame will be presented, which is a laminar premixed ethylene flame produced by a McKenna burner. These flames are generally considered to be flat, therefore, the numerical simulation problem is simplified into one dimension. This is advantageous due to the low simulation costs. However, it has been shown that these flat flames might not be completely flat, i.e. one-dimensional [252, 253]. In order to not fear the error introduced by improper modeling of the flow field, flow-flame interaction or especially the heat absorbed by the burner, it is a common approach to impose the temperature profile [116, 254]. This way the performance of the new extended chemical model and validation method can be put under the focus. The 3^{rd} laminar target flame of the 4^{th} ISF Workshop [123] (ISF-premixed-laminar-3) was chosen for validation, as it is the target flame for Laser Induced Incandescence (LII) measurements. The test rig was originally designed at the Lund Institute of Technology by Axelsson et al. [183].

5.1 Flame configuration

The measurement rig of the target flame used by several research groups [85, 88, 183, 255] is a water-cooled porous plug burner, the so-called McKenna burner, producing a premixed flat ethylene/air flame. Various equivalence ratios (Φ) were investigated experimentally, in a range from 2.0 to 2.5. In this work, the one with the most available primary particle size measurement data, Φ = 2.1, was chosen.

The material of the 60 mm diameter porous plug may differ between experiments. Stainless-steel was used in [183,244,255,256] and bronze in [85,88,178]. Migliorini et al. [252] pointed out that the choice of the plug material can signif-

Table 5.1: *Variation of integrated soot volume fraction at 14 mm HAB in ppm cm^2 [252]*

Φ	Stainless steel plug	Bronze plug
2.76	1.9551	6.457
2.1	0.632	1.868

icantly influence the soot volume fraction (f_v) distribution in the radial direction and also the total integrated f_v. The integrated f_v values obtained in [252] are summarized in Table 5.1.

The porous disk emitting the fuel/air mixture is surrounded with a wide, sintered ring to provide an outer co-flow of nitrogen which eliminates the peripheral diffusion. The total flow rate is 10 l/min (at 0 °C and 1 atm), equivalent to 6.44 cm/s cold flow inlet velocity. In the referred measurements the flame is stabilized with a stainless steel sheet 21 mm above burner outlet. The common practice is to simplify the flame to a one-dimensional problem.

5.2 Numerical setup

The numerical simulations were performed with the OpenSMOKE++ framework [177]. The inlet velocity and the species mass fractions were prescribed according to the experimental setup. The temperature profile was first imposed as suggested by the ISF Workshop [123] ("ISF"), then a simulation was performed with a modified temperature profile, in the region where experimental values from Bladh et al. [88] ("Bladh 2011") were available. The temperature profiles are plotted in Figure 5.1.

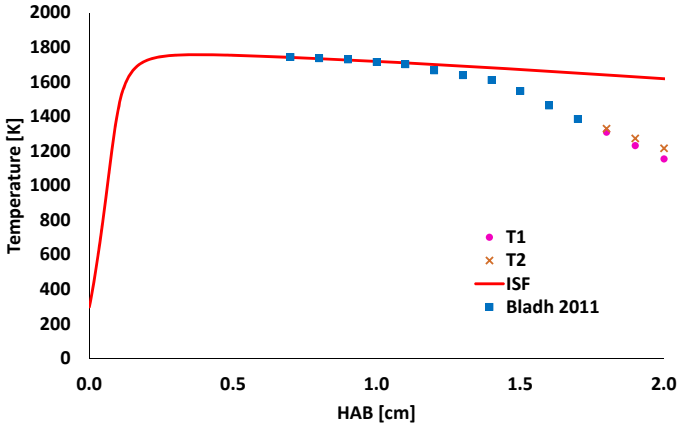

Figure 5.1: *Premixed laminar flame temperature distribution*

The numerical length of the domain was 4 cm for the "ISF" case, in order to minimize the effect of outlet boundary condition. However, for the "Bladh 2011" case the experimental temperature data was available only up to 1.7 cm and extrapolation is required to simulate a longer domain with an imposed temperature. In Figure 5.1 the two tested extrapolations, "T1" and "T2", are presented. No upstream effect was observed by changing the imposed temperature from "T1" to "T2", despite their significant effect on the results above 1.7 cm. Even without

the domain extension, the simulation result up to 1.7 cm HAB was identical to the former two cases. In the following, the results without the extended domain will be presented.

The primary particle size is determined by the combined model of CRECK Modeling Group's kinetic mechanism and the PPT described in Section 3. The LII signal was reconstructed by the code solving the equations presented in the Section 4.3. The differential equation was solved with 4th order Runge-Kutta method using the characteristics of the laser at the measurement of Bladh et al. [85]: laser wavelength = 1064 nm, fluence = 0.13 J/cm^2, shot duration = 11 ns, bandpass filter = 575$\pm$16 nm. Due to the low fluence, the vaporization was neglected.

While in the first study of Bladh et al. [85] a varying α_{T} (within the range of 0.5-0.61) has been retained, the second study [88] was performed with a constant value of α_{T} (0.37). Most of the works on TiRe-LII signal evaluations are based on a constant value of α_{T} [184, 217], though α_{T} may depend on the maturity of the soot particle [85, 245]. In the following, the constant value indicated by Bladh et al. [88] is retained since no reliable connection between hydrogenation level and α_{T} have been established yet [205]. In the study of Maffi et al. [257], the same burner construction, but a higher equivalence ratio (Φ = 2.3), was investigated and thermal accommodation coefficients and soot absorption coefficients were sought for different HABs to reach good agreement between the simulated and the measured signals. The retrained values for α_{T} and $E(m)$ varied from 0.22 to 0.34 and 0.29 to 0.31, respectively, with increasing HAB. As a comprehensive expression is not available to assign varying α_{T} and $E(m)$ for the different particle sizes and hydrogenation levels, the values used in the experimental investigation of Bladh et al. [88] will be used, i.e. α_{T} = 0.37 and $E(m)$ = 0.32.

5.3 Simulation results

Experimentally measured soot volume fractions [183, 255, 256] are compared to the numerical results using $d_{\mathrm{pp},N_{\mathrm{min}}} = 2\ nm$ (BIN$_5$) in Figure 5.2. The wavelengths used for the extinction-scattering measurements are indicated in the brackets in the plot. The deviations among the experimental results reach up to a factor of $\sim$6 in the upper flame region. In Section 4.4, it was highlighted that the refractive index may depend on the maturity andor the size of the soot particle, which may result in a different extinction-scattering response of the same particle population for a different wavelength. This explains the decreasing retained volume fraction with the increment of the laser beam wavelength, as the younger particles are not absorbing for the higher wavelengths. However, the volume fraction of the experimental investigations performed with the same laser wavelength are still not in agreement, this may be explained by the various soot absorption coefficients used by the researches. In the work of Axelsson et al. [183] and Zerbs et al. [256] the same refractive index is used, n = 1.56-0.46 provides $E(m)$ = 0.22. However, Hadef et al. [255] used a wavelength dependent absorption coefficient, resulting in $E(m)$ = 0.3 for 532 nm, which explains the lower volume fraction prediction. The difference between the results in [183, 256] was explained by

Zerbs et al. [256] by the different methods in calculating the optical path length, deviation in the ambient pressure or temperature, and the different burner quality and flame homogeneity.

The simulation result is in reasonably good agreement with the measurements and follows the general trend, i.e. the soot volume fraction increases with the height above the burner (HAB). The best agreement is found with the results of Axelsson et al. [183], where in the upper flame region (disregarding the last point at 1.7 cm HAB) a decreasing soot formation intensity is observed both numerically and experimentally. In the lower flame region, the simulation results may predict a too early start of soot formation. However, regarding the measurements uncertainties, this can not be properly judged.

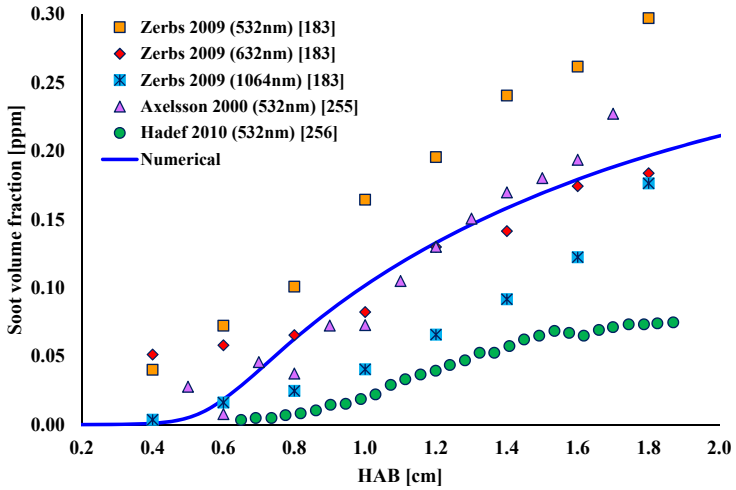

Figure 5.2: *Soot volume fraction comparison between experimental (marks) and numerical (solid line) results for the ISF-premixed-laminar-3 flame*

The three mean diameters defined in Eqs. 3.13-3.15 have been extracted from the numerical PPSD using two low cut-off sizes $d_{\mathrm{pp},N_{\mathrm{min}}} = 2\ nm$ and $d_{\mathrm{pp},N_{\mathrm{min}}} = 5\ nm$. Results are plotted in Figure 5.3 with both $d_{\mathrm{pp},N_{\mathrm{min}}}$ values[1].

[1]The choice of $d_{pp,N_{min}}$ has a marginal impact on the soot volume fraction compared to the experimental uncertainties since the maximum deviation between the two profiles was below 15 ppb.

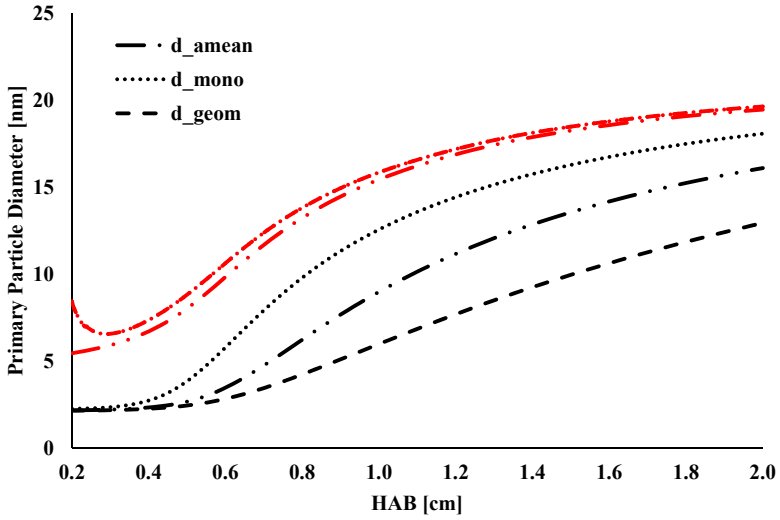

Figure 5.3: *Simulated d_{amean}, d_{mono} and d_{geom} with low cut-off size ∼2 nm (black) and ∼5 nm (red) for the ISF-premixed-laminar-3 flame*

The three type of mean diameters are very similar for $d_{\mathrm{pp},N_{\mathrm{min}}}$ = 5 nm. In Figure 5.4, the numerical PPSD is presented, and ρ^*_{pp} is the primary particle number per unit volume ($rho^*_{\mathrm{pp}} = rho_{\mathrm{pp}} \cdot \rho$). In the current flame, the numerically obtained distribution of particles above 5 nm is narrow. It has to be noticed, that this might be caused by the homogenizing effect of aggregation described in Section 3.

On the contrary, for $d_{\mathrm{pp},N_{\mathrm{min}}}$ = 2 nm the three characteristic diameters differ significantly, monodisperse assumption gives higher values than the arithmetic and the count mean diameter. This has to be kept in mind while performing validation with different measurement techniques, which may provide different characteristic diameters.

Close to the burner exit (between 0.2-0.3 cm HAB), the d_{mono} with the larger cut-off size shows a decreasing profile. In this region, the soot volume fraction is below 0.2 ppb and the second mode of the PPSD (particles above 5 nm) just starts to evolve. As d_{mono} is calculated based on the particle volume, which is proportional to the 3^{rd} power of the diameter, large particles have a huge impact resulting in an unexpectedly large d_{mono} for this region.

Due to the significant amount of very small soot particles (2-5 nm), which is classically observed for a wide range of conditions [38,74,103,251], the choice of the correct $d_{\mathrm{pp},N_{\mathrm{min}}}$ value may impact the mean d_{pp}. However, it should be noticed that this parameter is not introduced by the proposed tracking procedure, but it is related to the experimental sensitivity, i.e. the capability of the experimental setup to capture small soot particles. In the current flame, soot inception is present from 0.4 to 1.6 cm leading to significant small particle formation. Therefore, though the soot volume fraction only slightly differs by modifying the low cut-off size, the impact on the mean diameters is significant. This is important to recall when validation with experimental results is attempted in the traditional way.

Before investigating the model performance, the sensitivity to the model parameters (surface rounding and $d_{\mathrm{pp},N_{\mathrm{s}}}$) and the imposed temperature profile are explored.

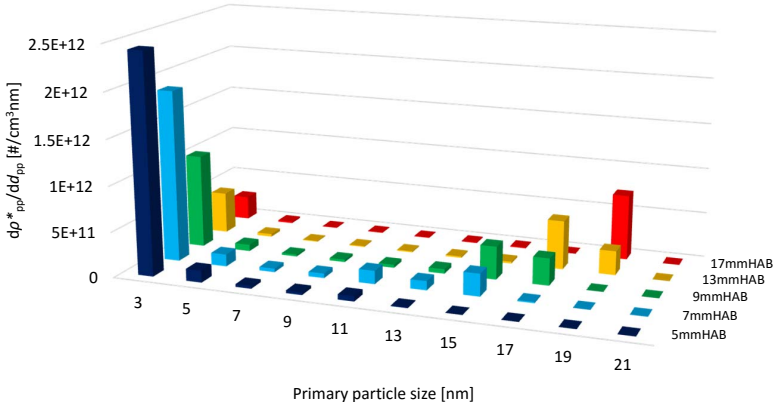

Figure 5.4: *Premixed laminar flame numerical PPSD at 5 different HABs*

5.3.1 Sensitivity to model parameters

Figure 5.5 shows the deviance of the calculated mean diameters determined when neglecting the surface rounding. The effect of the correction term is negligible (below 3%) for most of the diameters at all HABs, it plays an important role for d_{mono} in the lower flame region (∼0.3-0.7 mm, $f_{\text{v}} < 20\ ppb$).

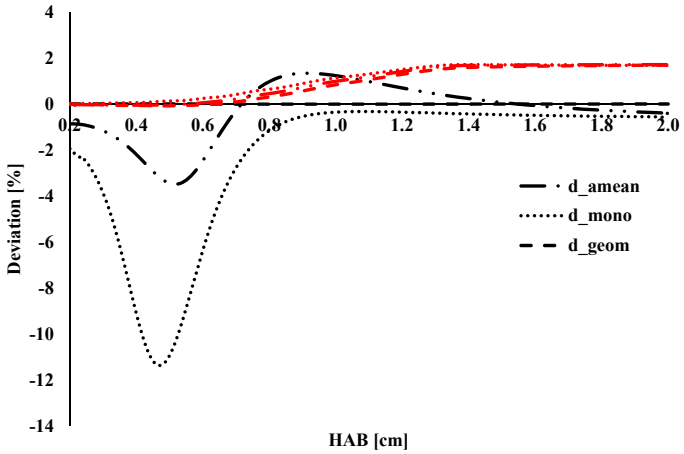

Figure 5.5: *Deviation of the calculated mean diameters determined by neglecting the surface rounding from the case accounting for this phenomenon for the ISF-premixed-laminar-3 flame*

The smallest aggregating particle might differ from the one originally assumed ($d_{\text{pp},N_{\text{s}}} \approx 10$ nm). The sensitivity to this parameter was investigated by modifying N_{s} to 10 and 14, resulting in $d_{\text{pp},N_{\text{s}}}$ = 6.4 and 16 nm respectively. A range of possible diameters (green shaded area) are determined and represented in Figure 5.6[2]. A deviation of ±15% can be observed compared to the baseline (solid line), however, the profile of the distribution remains qualitatively the same.

[2] $d_{pp,N_{min}} = 2\ nm$ was considered

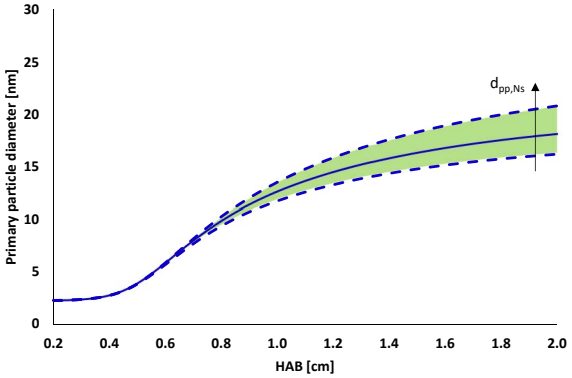

Figure 5.6: *Numerical d_{mono} with varied d_{pp,N_s} for the ISF-premixed-laminar-3 flame*

5.3.2 Sensitivity to the imposed temperature profile

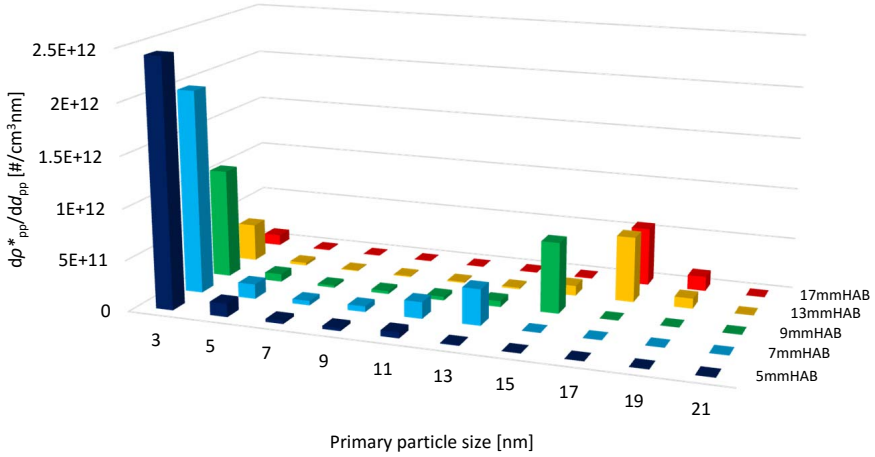

Figure 5.7: *Numerical results for a premixed laminar flame: PPSD at 5 different HABs of premixed flame using the "Bladh 2011" temperature profile*

In Figure 5.7, the PPSD is presented at five HABs for the "Bladh 2011" case. It can be observed that compared to the PPSDs of the "ISF" case (See Figure 5.4) the second mode is slightly shifted towards lover d_{pp} values and with the increasing HAB the first mode becomes less significant. This is due to the reduced nucleation caused by the lower temperatures of the "Bladh 2011" case, which leads on the one side to less small particle formation, on the other side to their reduced condensation on the large particles.

Figure 5.8 shows the d_{mono} results with the two different imposed temperatures presented in Figure 5.1. The shaded areas represent the possible mean diameters choosing $d_{\mathrm{pp},N_{\mathrm{min}}}$ from the range of 2 to 5 nm. The profiles of d_{mono} do not differ significantly in the lower flame region (from 0.2 to $\sim$1.3 cm HAB). This is due to the very close agreement between the two simulations in terms of the soot volume fraction, and the total number of primary particles (see Figure 5.10). In the upper flame region, where the TEM results of Bladh et al. [88] showed a stagnating particle size, the "Bladh 2011" case shows no further mean diameter increment.

On the contrary, the mean d_{pp} is slightly increasing when the "ISF" temperature profile is imposed.

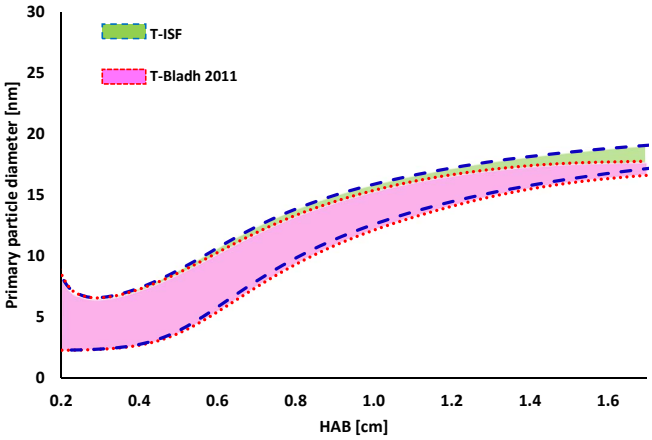

Figure 5.8: *Numerical results for a premixed laminar flame: numerical d_{mono} by imposing "ISF" (T-ISF) and "Bladh 2011" (T-Bladh 2011) temperature profiles*

In order to understand this phenomenon, the soot formation process rates are depicted along the simulation domain in Figure 5.9. Despite the very small deviation in the temperature profiles in the range of 0.7 to 1.1 cm HAB the difference in the surface growth rate is not negligible. This explains the slightly larger primary particle size of the "ISF" case. In the upper region, an even larger difference between the two cases in terms of surface growth rate can be observed. Furthermore, the inception rate also shows a faster decrement with the HAB for the "Bladh-T" case. The former explains the shift of the second mode towards smaller values and the latter the smaller relevance of the first mode in the "Bladh-T" case, as the lower inception provides less supply for the first mode and the lack of surface growth prevents the further growth of the second mode. Nevertheless, both cases resulted in persistent soot inception along the flame, which is in agreement with the observations of Stirn et al. [244].

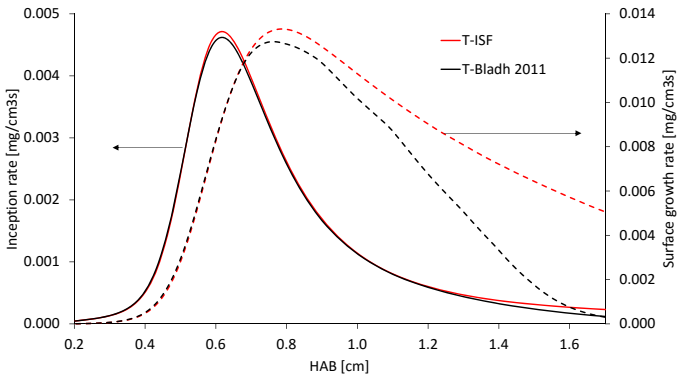

Figure 5.9: *Soot formation process rates for the "ISF-T" and the "Bladh-T" cases*

In conclusion, the slight difference in the trend (lack of further increment in the upper flame region) indicates that despite the marginal deviation in terms of soot volume fraction and mean d_{pp}, the change in the PPSD is not negligible.

Nevertheless, as the deviation in terms of mean d_{pp} is not significant, the validation will be performed with the results obtained using the original temperature profile.

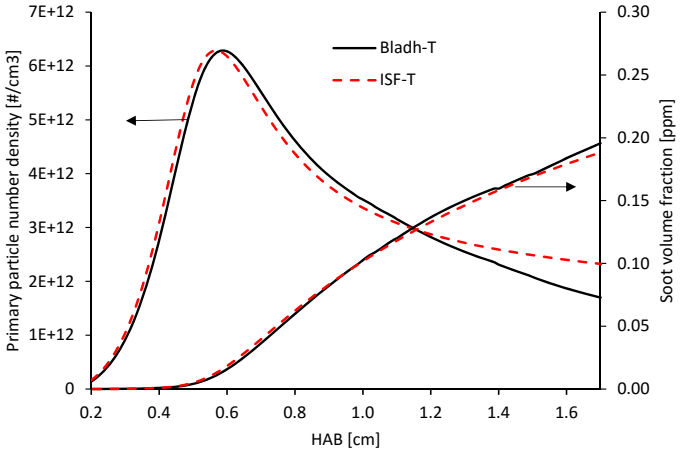

Figure 5.10: *Numerical results for a premixed laminar flame: primary particle density and soot volume fraction for case "ISF-T" and "Bladh-T"*

5.3.3 Sensitivity to the primary particle size assumed in the kinetic scheme

The primary particle size influences the collision diameter through Eq. 1.2, and consequently the reaction rate, as it was described in Section 2.2.2. d_c was not recalculated based on the d_{pp} obtained by the new model, but by the original d_{pp} = 10.14 nm assumption for the aggregates. In order to see the possible effect of a modified d_{pp} the simulation was performed with two different d_{pp} assumptions, 6.4 nm (BIN_{10}) and 16.04 nm (BIN_{14}). These simulations represent only a rough estimation of the possible impact of accounting for the primary particle size variation, i.e. coupling the model and the kinetic mechanism, as the coupling would result in a location and BIN dependent d_{pp}, not a constant one. The resultant soot volume fractions are presented in Figure 5.11 along with the original simulation results and the experimental data from [183, 255, 256].

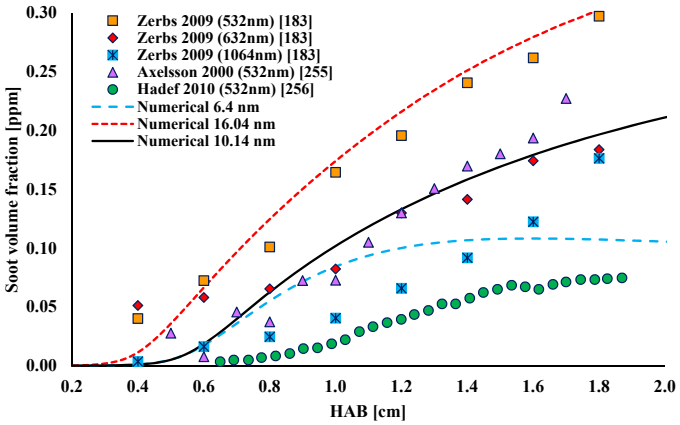

Figure 5.11: *Experimental [183, 255, 256] (marks) and numerical (line) soot volume fraction. Numerical results were obtained by three different constant d_{pp} assumption for the aggregates (6.4 nm, 10.14 nm and 16.04 nm)*

Imposing smaller d_{pp} results in smaller soot volume fraction all along the flame, on the contrary, the simulation with larger d_{pp} for the aggregate BINs lead to larger soot volume fraction. The soot volume fractions significantly differ from the baseline, however, the results are still within the experimental uncertainties.

5.4 Traditional validation of mean primary particle diameter

In the following, the traditional way of validation is performed, i.e. the mean diameter derived from the numerical simulation is compared to the mean diameter determined from the experiments, both TEM and TiRe-LII.

Such a comparison is affected by uncertainties. The definition of mean diameter varies depending on the experimental method, the smallest diameter to consider is usually not obvious and the possible errors introduced in deriving PPSD from TiRe-LII were described in Section 4.4.

In Figure 5.12, the numerical d_{amean} is compared to the TEM experimental results of Bladh et al. [85, 88]. The most recent measurements (red circles) were performed on a wider HAB range and indicate an intense growth of primary particle size between 0.6 to 1.1 cm HAB. In the upper region (1.1 to 1.7 cm HAB), after the intense growth, the d_{amean} does not vary significantly. The former measurements [85] (purple symbols) predicted larger values at the three measurement locations.

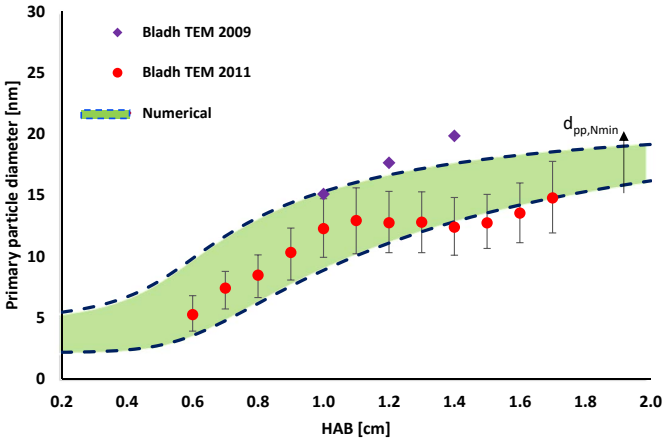

Figure 5.12: *Experimentally [85, 88] and numerically obtained arithmetic mean primary particle diameter in a premixed laminar flame*

It should be noticed that in the earlier article of Bladh et al. [85], the particles below 5 nm are not present in the PPSD, however, in the later paper [88] the diameter of the smallest captured particle is not indicated. Therefore, the numerically determined d_{amean} was calculated both with a low cut-off size of $d_{\mathrm{pp},N_{\mathrm{min}}} = 2$ nm and $d_{\mathrm{pp},N_{\mathrm{min}}} = 5$ nm (bottom and top blue dashed lines respectively) providing a range of possible solutions (green area). The overall agreement between the numerical simulation and the experimental results can be considered satisfactory (within the uncertainty limits).

Alternatively, the experimental d_{mono} was obtained with TiRe-LII by Bladh et al. [88] (brown squares), by Stirn et al. [244] (yellow "+") and by Axelsson et al. [183] (purple triangles) by assuming constant α_{T}, monodispersity and self-standing primary particles. As the pictures taken by TEM [88] showed aggregate structures appearing already at HAB = 1 cm, and at HAB = 1.6 cm fractal particles with numerous primary particles were observed, Bladh and coworkers performed a reevaluation of the LII signal by assuming aggregate structures con-

sisting of 100 primary particles at HAB = 1.7 cm, labeled "np = 100" (pink rhombus). The reevaluation with n_p = 100 by Bladh et al. [88] resulted in a drop of d_{mono} from 28 to 18.5 nm, which gave a closer agreement with the values obtained by TEM. These experimental results are presented in Figure 5.13 along with the d_{mono} derived from the TEM experiment [88] (blue circle) and the numerical d_{mono} values.

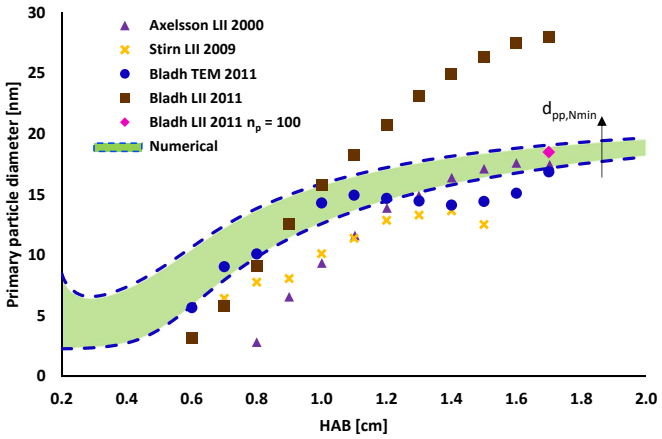

Figure 5.13: *Experimentally [85, 88, 183, 244] and numerically obtained primary particle diameter with monodisperse assumption*

While TiRe-LII determined profiles in [88, 183] show a constant increment of the primary particle diameter with the HAB, d_{mono} obtained in the TEM experiment and by the TiRe-LII of Stirn et al. [244] does not change monotonically with the HAB. The difference between the three LII measurement results is significant, which can be related either to differences in the measurement setup or to the different post-processing technique.

As mentioned in Section 5.1, Migliorini et al. [252] observed that the material used for the porous plug stabilizing the flame can affect the soot volume fraction yield. This may possibly explain the significant difference between the two TiRe-LII derived d_{mono} values by Bladh et al. [88] and Axelsson et al. [183]. However, the same porous plug material was used by Stirn et al. [244] and Bladh et. al. [88], therefore the deviation cannot be explained by this difference. Furthermore, differences may also be due to different LII models used by the groups, especially concerning the condensation description.

To extract d_{mono} from the numerical results it is important to identify the smallest diameter to consider. As discussed in Section 4.4, small particles absorb laser energy and emit LII signal, but with the appearance of large particles, their contribution becomes negligible so that it is not possible to determine a general $d_{det,min}$. Further proof for this will be presented in the next Section. Therefore, d_{mono} was calculated both with $d_{pp,N_{min}}$ = 2 nm and $d_{pp,N_{min}}$ = 5 nm (bottom and top red dashed lines respectively) to identify a range of possible diameters (green area) as done in Figure 5.13.

The numerical results tend to slightly overestimate the experimental values in the lower flame region (0.6-0.9 cm HAB). From 0.9 to 1.2 cm HAB the simulation is in good agreement with the experiments within the experimental uncertainties.

In the upper flame region, above 1.2 cm HAB, evaluating the simulation performance is not obvious. The numerical values are very close or just slightly higher than most of the experimental values. However, the "Bladh 2011" results with n_p = 1 predict much higher values.

Even though the agreement with TEM measurements is promising, the validation of the numerical model by comparing the results with the TiRe-LII derived d_{mono} is not straightforward. The over-prediction of mean d_{pp} in the early nucleating region or the later surface growth region would lead to very different conclusions and consequent modifications of the model. The reevaluation with $n_{\text{p}} = 100$ indicates that the difference between the numerical and "Bladh 2011 n_p = 1" results may be caused mainly by the neglect of the shielding effect when processing the experimental data. Depending on the choice of the low cut-off size the conclusions change again. Whereas with $d_{\text{pp},N_{\text{min}}} = 2$ nm the model seems to be correct, the use of $d_{\text{pp},N_{\text{min}}}$ = 5 nm would mean that slower growth of particles or more intense nucleation is required.

In conclusion, the traditional comparison with TiRe-LII does not allow an advanced analysis of the accuracy of the model. In addition, the definition of mean diameter depends on the retained experimental method and the smallest diameter to be considered is difficult to establish.

In order to draw firm conclusions on the validity and/or to identify the potential paths of the chemical model improvement, a more reliable evaluation is needed. In particular, to identify the reactions that may need an update, it is crucial to accurately locate the region of the d_{pp} mismatch. Therefore, in the following section, the LII signal decay reconstructed from the numerical results is compared to the experimental signal in order to understand if additional indications on the accuracy of the model can be obtained.

5.5 LII signal comparison

In this section, the measured and the synthesized LII signals are compared to test the novel validation approach and potentially improve the validation procedure. Four HABs (7, 9, 13 and 17 mm) were selected for the LII signal reconstruction and comparison to the experimental data [88].

From the numerical PPSD, the LII signal was synthesized for the various HABs and the decay times and pre-exponential factors were extracted for both by considering the PPSD above $d_{\text{pp},N_{\text{min}}}$ = 2 nm and above $d_{\text{pp},N_{\text{min}}}$ = 5 nm. The dependence of the fitting parameters on the HAB is presented in Figure 5.14.

With growing HAB the decay times increase for both $d_{\text{pp},N_{\text{min}}}$ values, as expected from the particle size increment. The difference between τ_1 and τ_2, as well as S_1 and S_2 increases with the HAB for both low cut-off sizes. The constantly decreasing S_1 means that the first component of the double-exponential fit becomes less relevant with HAB.

At small HABs (5 and 7 mm), both the decay times and the pre-exponential factors differ significantly for the two low cut-off sizes. At 5 mm the pre-exponential factors, S_1 and S_2, for $d_{\text{pp},N_{\text{min}}}$ = 2 nm are reversed compared to the other results. This may be related to the PPSD transition from a characteristically

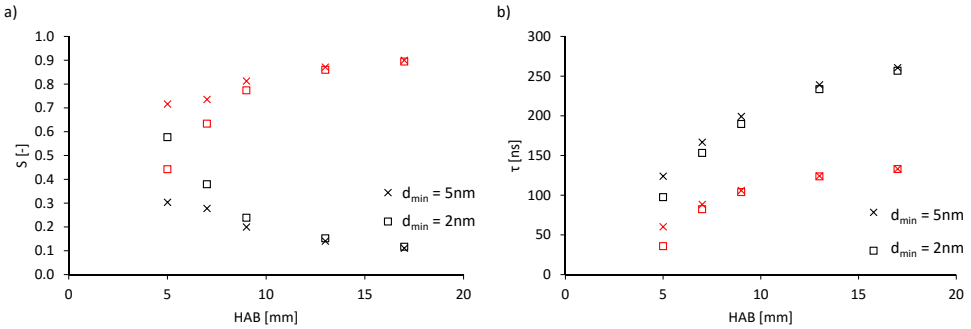

Figure 5.14: *a) Pre-exponential factors S_1 (black) and S_2 (red) b) decay times τ_1 (black) and τ_2 (red). Premixed flame simulation results.*

unimodal to a bimodal shape that takes place between 5 and 7 mm HAB (see Figure 5.4). At 7 mm the second mode of PPSD becomes more relevant. However, a mismatch between the decay times derived with the different low cut-off sizes is still present. This observation indicates that at the change of PPSD shape from unimodal to bimodal there is no sharp transition regarding the relevance of the contribution of the small particles to the total LII signal.

The decay times and pre-exponential factors are sensitive only close to the burner exit to the low cut-off limit where the PPSD has only a moderate amount of large particles. These results are in agreement with earlier observations about the detectability of small particles when a bimodal PPSD is observed.

In Figure 5.15, the normalized LII signals (Eq. 4.33) synthesized from the numerical PPSDs are compared to the experimental ones [88]. The d_{mono} for these locations are summarized in Table 5.2, both for the experimental and the numerical investigations.

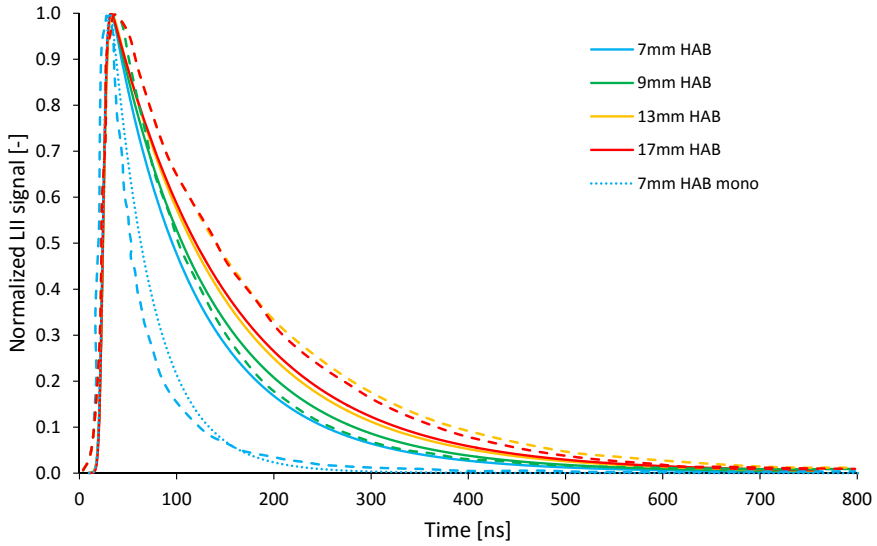

Figure 5.15: *Comparison of synthesized and measured [88] LII signal at four HABs (7, 9, 13 and 17 mm)*

Despite the good agreement with the TEM results on the mean d_{pp}, the LII signals indicate that there are significant mismatches in the PPSDs. The simu-

HAB [mm]	Bladh et al. [88]	Numerical "ISF-T	Numerical "Bladh-T"
7	5.8	8.2	7.8
9	12.6	11.4	10.8
13	23	15.1	14.8
17	28	16.87	14.3

Table 5.2: *d_{mono} [nm] at different HABs derived from TiRe-LII by Bladh [88] and from numerical simulations with $d_{pp,N_{min}}$ = 2 nm*

lation under-predicts the decay speed at 7 mm HAB. As it was shown in Figure 4.10, the presence of few larger particles (10 to 16 nm) "hide" the presence of the small particles. Therefore, the τ over-prediction may originate not just from the larger mean diameter, but from the "hiding" effect caused by the large particles. A lower number of large particles would be required to obtain a better match with the measured LII signal. The LII signal at 7 mm HAB was reconstructed also with a monodisperse distribution assumption matching the d_{mono} derived from the PPSD. This is marked by "7 mm HAB mono" in Figure 5.15 providing a significantly closer agreement with the experimental signal. Therefore, it can be inferred that the experimental PPSD at 7 mm HAB is probably more similar to an almost unimodal PPSD with even less primary particles above 5 nm diameter and the numerical PPSD shape is therefore incorrect.

The intense change in the decay time from 7 to 9 mm in the experiment is probably caused not only by an increasing mean diameter but also by the transition from unimodal to bimodal PPSD. By comparing experimental and synthesized LII signals, it can then be deduced that the location of the transition from unimodal to bimodal PPSD is mistaken by the numerical simulation. This important information can be accessed only by the LII signal analysis.

On the contrary, at high HABs, the signal decay is slower compared to the experimental signal, which means the underestimation either of the primary particle size or the n_{p}. However, it has to be noticed that this comparison was done using the PPSD of the numerical simulation obtained in the "ISF-T" case, which deviates in the upper flame region in terms of temperature respect to the experiments [88].

In Figure 5.16 the synthesized LII signal reconstructed from the PPSD in the "Bladh-T" case is shown. The related d_{mono} diameters are summarized in Table 5.2. Both the lower primary particle size and the lower temperature results in a faster signal decay. The deviation from the experimental signals is even more significant, however, it is important to notice that the signal belonging to 17 mm HAB is slower than the one of 13 and even of 9 mm HAB. To capture the experimental signal decay at 17 mm HAB, a higher number and size of large particles would be required. Therefore, even if the total number of primary particles are in good agreement, which was proven by comparing the d_{mono} with the TEM measurements, the PPSD was not captured.

The numerical LII signal decay speed does not vary as much as the measured one for neither cases in the range between 7 to 13 mm HAB. Alternatively, this may be related to the fixed α_{T} used at the LII signal reconstructions, as the soot particles are expected to mature over residence time, consequently with HAB,

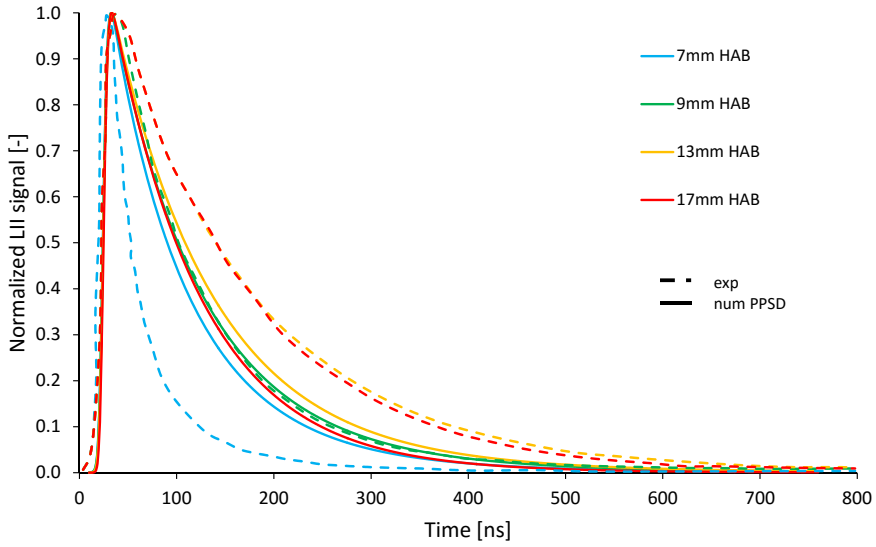

Figure 5.16: *Comparison of synthesized and measured [88] LII signal at four HABs (7, 9, 13 and 17 mm). Numerical simulation performed by imposing the Bladh-T temperature profile.*

which may result smaller α_{T} and therefore even larger decay times. As mentioned before, in the study of Bladh et al. [85] a change with the HAB from 0.61 to 0.5 in the α_{T}, for 1 and 1.2 cm HAB respectively, was observed. The sensitivity study showed that very small variation of α_{T} may results in very different decay times. Unfortunately, the uncertainty in α_{T} cannot be suppressed as long as the relation between H/C ratio and α_T is not known. Nevertheless, once the relation is available, the synthesized signal from simulations with CDSM can easily account for this parameter.

5.6 Conclusions

The soot volume fraction was well predicted (within the uncertainty limits) for the premixed flame compared to the experimental results found in the literature. The primary particle tracking model parameters, as the surface rounding and the smallest aggregating particle size, had only a moderate impact on the mean primary particle diameter. The originally imposed temperature, which was suggested by the ISF workshop, was modified with the experimental results of Bladh et al. [88] (where available). The effect of the imposed temperature change was relevant only in the upper flame region, where the measurement temperatures were significantly lower. Here, the result of the changed imposed temperature was a slightly lower mean primary particle size, lower importance of the first mode of the PPSD and a slight shift of its second mode towards the smaller diameters compared to the original case. This altogether was a result of the lower precursor formation rate in this region, which provides a lower supply, on the one hand, for the first mode (through inception) and, on the other hand, for the growth of large particles (through surface growth). In order to roughly estimate the possible impact of coupling the kinetic mechanism and the PPT model, simulations were performed by using a modified kinetic mechanism once with d_{pp} =

6.4 nm, and another time with d_{pp} = 16.04 nm, for all aggregates. The resultant soot volume fractions significantly deviated from the baseline simulation (d_{pp} = 10.14 nm), however, they were still within the measurement uncertainties.

The numerically obtained mean primary particle size showed good agreement with the TEM experimental results [88] within the uncertainty limits. The agreement of the numerical d_{mono} with TiRe-LII results in [88, 244] was satisfying in the lower flame region (up to $\sim$1 cm HAB), but deviated for the results found in [183]. In the upper flame region the experimental values of [183, 244] were well captured, and at HAB = 1.7 cm when n_{p} = 100 was considered at the LII signal evaluation in [88]. On the contrary, a significant mismatch was observed in the upper flame region (above $\sim$1 cm HAB) when n_{p} = 1 was considered at the LII signal evaluation in [88]. Therefore, the validity in this region based on the TiRe-LII results cannot be properly judged.

The forward validation approach was used to gain further knowledge about the PPT model validity by using the incandescence signals of the TiRe-LII measurements [88]. The reconstructed incandescence signal was in the same range as the experimentally captured one, however, the change of its decay time with the HAB was not in good agreement with the measurement. This difference might originate from two phenomena. First, the transition of the PPSD from unimodal to bimodal is probably mistaken by the numerical simulation. Second, the analysis indicates that at high HABs the presence of larger particles might be required, so that larger decay times are achieved. Unfortunately, as long as the dependence of α_{T} on soot properties is not known and considered, the conclusions still remain somewhat speculative. However, the potential in the forward validation approach is proven.

CHAPTER 6

Coflow Laminar Flame

Motivated by the performance of the PPT model in the 1D flame, a more challenging flame was targeted. In this chapter, the investigation of the chosen laminar coflow diffusion flame series is discussed. These flames are still easy to model since due to the axisymmetric flow field the simulation domain simplifies to two dimensions.

Despite the increased use of TiRe-LII for experimental d_{pp} determination, a limited number of measurement results can be found for laminar diffusion flames. One of the flames measured by several research groups [77, 84, 144, 188, 241] is among the target laminar coflow flames of the International Sooting Flame (ISF) Workshop [123], in the following, this is referred to as ISF-coflow-laminar-3. The ISF Workshop suggests four different dilutions for the fuel stream: 32% (F32), 40% (F40), 60% (F60) and 80% (F80) ethylene content respect to the volume, moving from a lightly sooting towards a heavily sooting condition. The advantage of choosing such flame series is to have a large variety of soot particles in terms of maturity and size. In specific, primary particles in the range from 5 to 60 nm diameter [77] were observed with TEM.

It is important to notice that the good behavior of a soot description on the dilution effects regarding the location of the peak values of both f_{v} and d_{pp} is rarely reported in the literature. Recent models may provide a good agreement for one specific coflow flame, but obtain a mismatch for other flames [26,166,199, 258]. Eventually, they may capture the peak value for several coflow flames, but without providing the spatial distribution for the varying dilution [167], so that the agreement with experiment cannot be definitely assessed. Furthermore, there are only a few models tested both on premixed flames and coflow flames [26,47].

To ensure that the model is predictive, it has to be validated in various condi-

tions without optimizing the model parameters for the targeted flame. The herein used kinetic scheme was validated on various premixed flames [27,124,259–261] and no model parameter adjustment was carried out for the current cases.

6.1 Flame configuration

The burner was originally designed at the Yale University [262] and shared with other laboratories. Ethylene-nitrogen mixture and air are injected through two co-axial tubes with an internal diameter of 4.0 mm (0.38 mm wall thickness) and of 74 mm, or in case of [84] 50 mm, respectively. The inlet diameter of the fuel side tube slightly differs (3.9 mm) in case of the experiment performed by Franzelli et al. [84]. It was shown that this might have a measurable impact on the flame length, as a modification of the flow rate with 4% led to nearly 6 mm change in the flame length for F80 [84]. Electronic mass flow controllers long term accuracy is within 5% [166], which means differences in flame lengths might occur even with the same nominal flow rates. The bulk velocity for the nominal conditions is 35 cm/s for both inlets. A uniform inlet profile is usually ensured with a honeycomb mesh at the airflow side. The fuel side is usually assumed to have a fully developed, parabolic velocity profile generally developed in tubes.

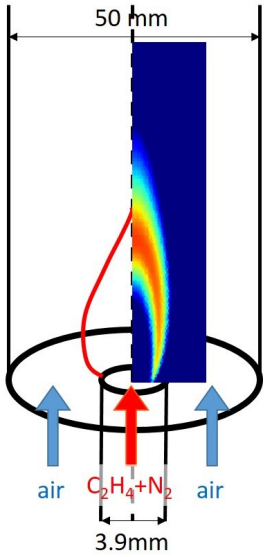

Figure 6.1: *Flame configuration of Yale Diffusion Burner*

The LII measurement in [84] was carried out with an Nd:YAG laser (1064 nm) focused on a 0.35 mm thick and 10 cm wide plane on the burner axis, with a fluence of 0.45 J/cm2 (shot duration $\approx$ 9 ns). Such a high fluence ensure an intense sublimation of the particles [120]. Camera gate was set to zero with a 25 ns exposure time and the signal was collected for 6 different delay times for each dilution. The bandpass filter was centered at 425 nm with a width of 50 nm. Further details are available in the paper of Franzelli et al. [84].

Simulations were performed also with a harmonically modulated inlet velocity. As the mesh independence was not achieved and only preliminary results are available, the analysis of these results were not performed in depth. The preliminary results are provided in Appendix B.

6.2 Numerical model

The simulations are performed with the laminarSMOKE code [174], which operates in the OpenFOAM framework and it is specifically designed to solve multidimensional laminar reacting flows with detailed kinetic mechanisms. The classical transport equations - mass, momentum, species, and energy - for continuous, multicomponent, compressible, thermally-perfect mixtures of gases (including the chemical source terms) are solved. The thermophoresis [263] and Soret effects [264] are accounted for in the simulation and the buoyancy effect is consid-

ered. The flow field is calculated with a SIMPLE solver [90, 265] and a second order centered spacial discretization scheme is applied. Further details on the numerical model are provided in the Appendix A.

The simulation domain is simplified to 2 dimensions as a result of the axial symmetry of the problem. Two structured meshes with different resolution are adapted to the 15x7 cm (height x radial extent) simulation domain, both with an increased resolution in the flame region. The coarser mesh is constituted of 3600 cells (80x45, $\Delta x \approx$0.3 mm and $\Delta y \approx$1 mm in the flame region) similar to the numerical meshes used for coflow flames in [174, 266–269]. The fine mesh has 41600 cells (400x104, $\Delta x \approx$0.15mm and $\Delta y \approx$0.2 mm in the flame region) similar to finer meshes used for coflow flames in [174, 269]. The extent of the mesh ensures that the boundary conditions do not affect the flame region. Due to the intense computational demand of the high-resolution mesh, the simulations with the finer mesh are carried out only for F32 and F80.

Dirichlet conditions are imposed to fix the velocity, the temperature and the composition on the inlet. At the fuel inlet (inner stream), a fully developed, parabolic velocity profile is assumed. A uniform flow profile is imposed for the oxidizer (outer) stream. The streams are injected with a bulk velocity of 35 cm/s, atmospheric pressure and 293 K temperature. Neumann conditions are adopted to model the outflow at the top of the computational domain. At the centerline, symmetry conditions are imposed.

The primary particle size is determined by the combined model of the CRECK Modeling Group's kinetic mechanism [27] and the PPT described in Section 3. For the LII signal reconstruction the previously described model was used, and α_{T} = 0.37 was considered as no clarified dependence of α_{T} on H/C is established yet.. However, an investigation of a laminar coflow diffusion flame provided the same value [200]. Regarding $E(m)$, 0.32 was used during the signal synthesis.

6.3 Temperature and soot volume fraction

First, the soot volume fraction prediction of the model for the full flame series is presented and compared to experimental results, then the two extreme cases, F32 and F80, are further discussed. In Figure 6.2 the soot volume fraction profiles are compared between the experimental results obtained by Smooke et al. [144] and the numerical results. In Table 6.1 the peak f_{v} values are summarized with the value ranges in brackets representing the experimental uncertainty. Peak f_{v} values found in other studies for the investigated flame series [144, 166, 167] are also presented in Table 6.1. Despite the under-prediction in terms of f_{v} for all dilutions and the smaller length of centerline sooty region for F60 and F80, the numerical results are sufficiently in line with the state-of-the-art models (the transition of the high soot volume fraction due to dilution is captured, and the factor compared to experimental peak f_{v} value is consistent for all 4 flames). Thus a qualitative analysis can be performed.

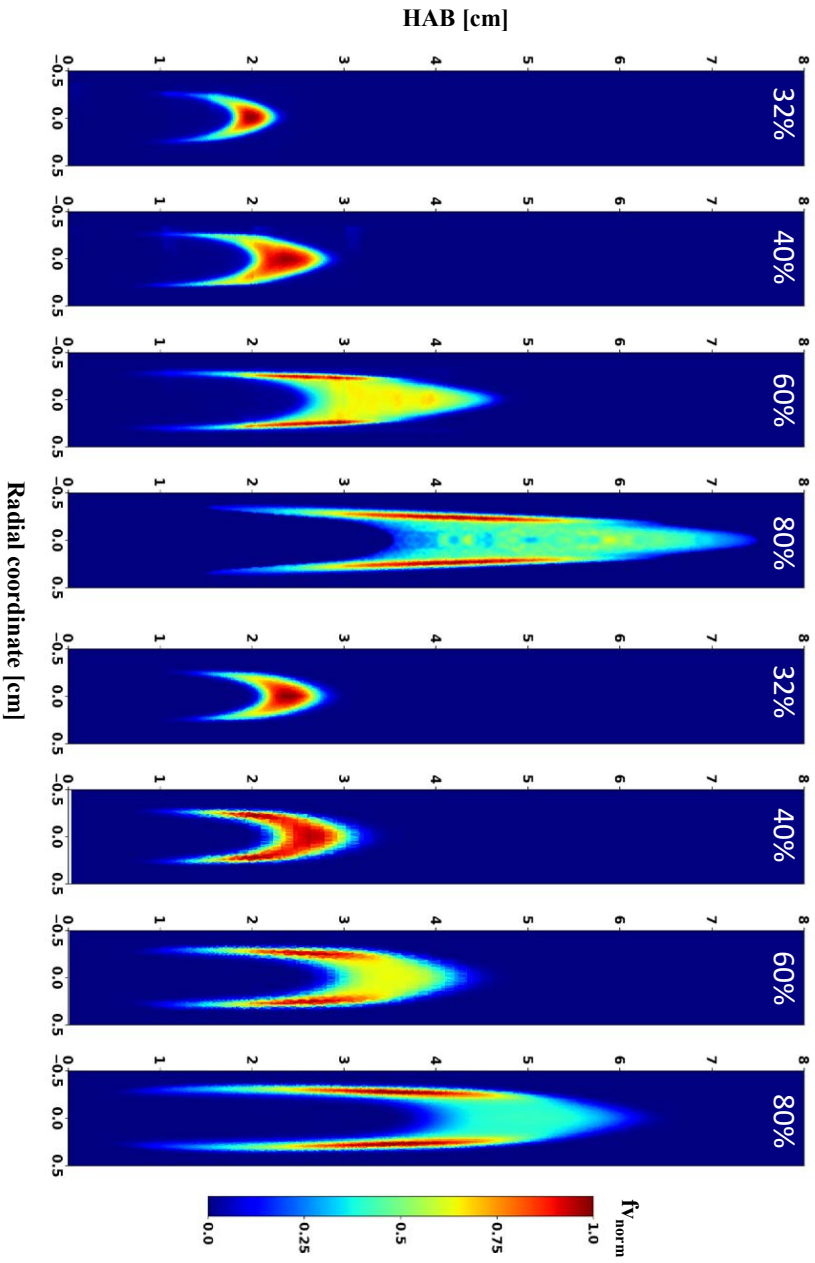

Figure 6.2: *Experimental and numerical normalized soot volume fraction for all four dilutions of the ISF-coflow-laminar-3 flame*

Case	F32	F40	F60	F80
Experimental [144]	[0.1,0.3]	[0.3,0.6]	[1.1,2.1]	[2.4,4.4]
Numerical [144]	∼0.88	∼1.3	∼3.0	∼4.4
Numerical [166]	∼0.26	∼0.5	∼1.1	∼1.6
Numerical [167]	0.2	0.4	1.2	3.3
Numerical	0.08	0.13	0.5	1.67

Table 6.1: *Soot volume fraction peak values in ppm for all ISF-coflow-laminar-3 flames*

In the following, the temperature and soot volume fraction results of the two extreme cases are compared to further experimental data found in the literature [84, 188, 241]. Then the simulation results will be used first to apply the new procedure (the PPT) and evaluate its interest, secondly, to perform the new validation method and finally to investigate the effect of dilution.

6.3.1 80% ethylene flame

In Figure 6.3, the numerical temperature field is compared to the experimental results obtained by pyrometry at Yale University [262] and the EM2C laboratory [84]. The temperature field of the numerical simulation deviates from the experimental results in the upper region. The simulation predicts a shorter flame without the inner cooler region. The possible explanation of the discrepancy will be discussed later in Section 6.6.1.

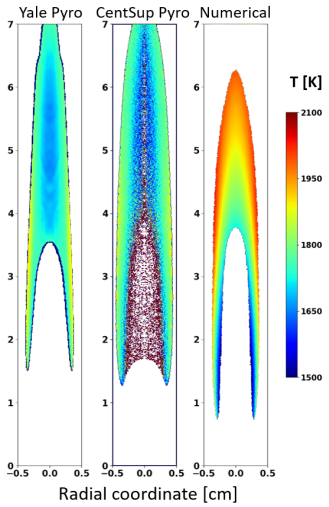

Figure 6.3: *Temperature profile experimental (left) and numerical (right) results for F80*

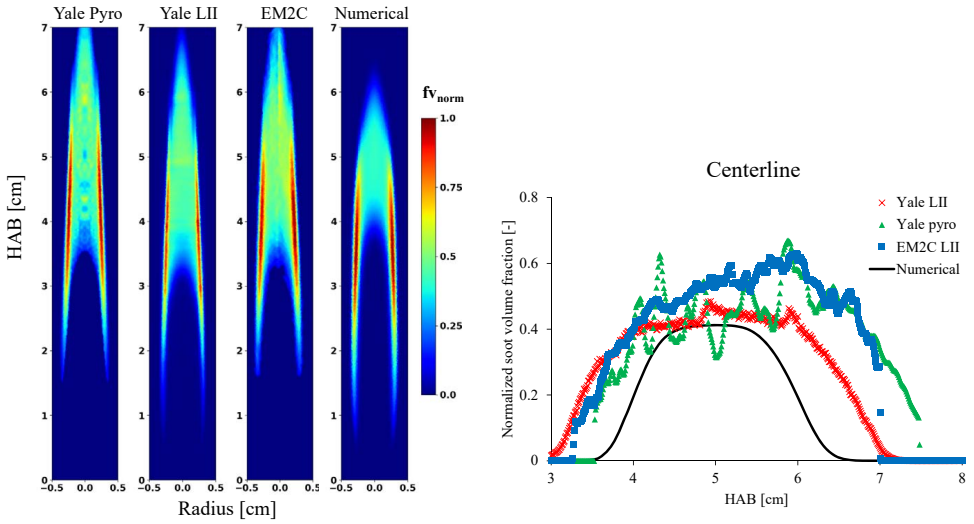

Figure 6.4: *Comparison of normalized soot volume fraction in the full flame cross-section (left) and the along centerline (right) between measurements [84, 144, 241] and simulation for F80*

Case	Yale Pyro [241]	Yale LII [144]	EM2C LII [84]	Numerical
Max f_v	4.0	4.3	4.65	1.67

Table 6.2: *Soot volume fraction peak values in ppm for F80*

In Figure 6.4 the experimental [84, 144, 241] and the numerical soot volume fractions normalized by their peak value (values provided in Table 6.2 for each case) are presented in the flame cross section and along the centerline. The numerical determination of soot volume fraction was performed using $d_{\mathrm{pp},N_{\mathrm{min}}} = 2$ nm. However the difference observed when assuming $d_{\mathrm{pp},N_{\mathrm{min}}} = 5$ nm is marginal (less than 1%). The peak value of the experimental soot volume fraction is $\sim$3 times higher than the numerical simulation. The width of the flame is well captured.

6.3.2 32% ethylene flame

For the 32% ethylene volumetric content fuel stream case (F32), the simulation captured the temperature profile well as shown in Figure 6.5. A slight discrepancy is visible in the flame height (∼1.5 mm). However, as the velocity inlet profile was not validated, this may be explained by the high sensitivity of flame lengths on the inlet conditions pointed out by Franzelli et al. [84].

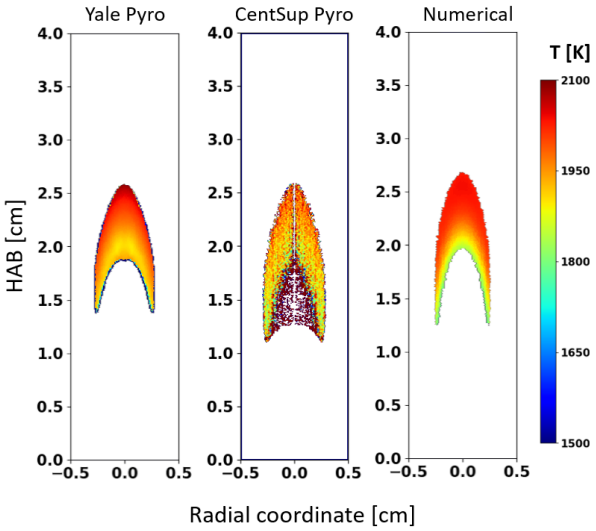

Figure 6.5: *Temperature profile comparison of experimental and numerical results for F32*

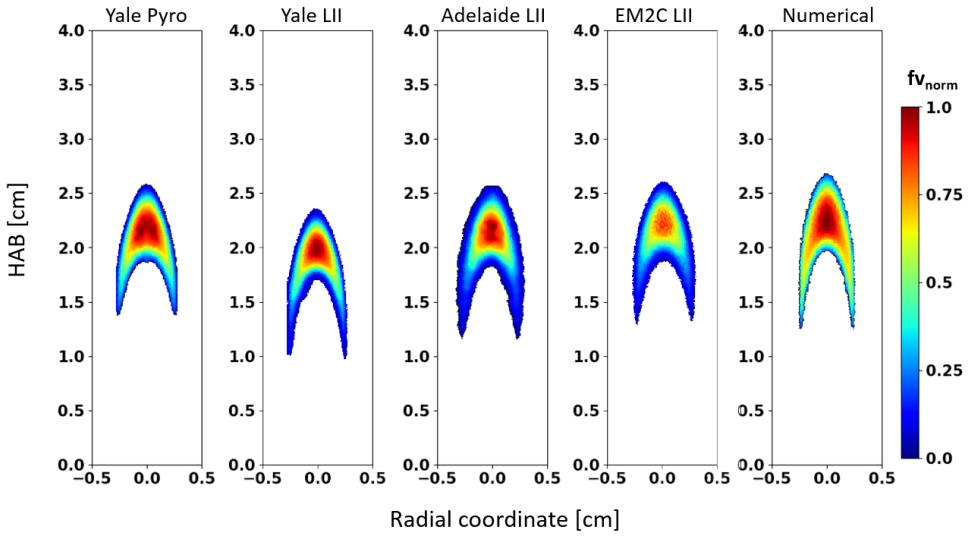

Figure 6.6: *Normalized soot volume fraction comparison of experimental and numerical results for F32*

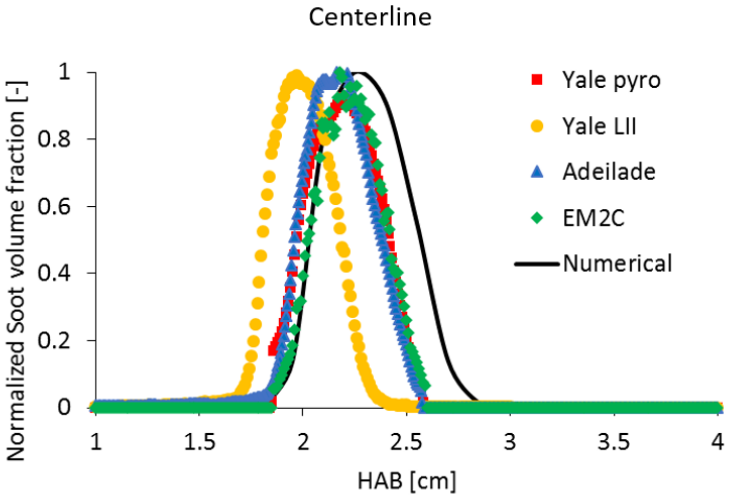

Figure 6.7: *Experimental [84, 144, 188, 241] and numerical normalized soot volume fraction along centerline for F32*

Case	Yale Pyro [241]	Yale LII [144]	Adel. LII [188]	EM2C LII [84]	Num.
Max f_v	0.27	0.27	0.24	0.34	0.057

Table 6.3: *Soot volume fraction peak values in ppm for F32*

In Figure 6.6, the experimental and numerical soot volume fractions normalized by their peak value are presented and the peak values are summarized in Table 6.3. The profile along the centerline is shown in Figure 6.7.

Although the maximum value is numerically under-predicted by a factor of ∼4-6, the numerical profile is in a qualitatively good agreement with the experiments, both in terms of height and width of the sooty region.

6.4 Primary particle size analysis

In the following section, the numerical mean primary particle size for the F80 and F32 is analyzed. F80 simulation is first investigated in terms of the evaluation parameters (type of characteristic mean diameter and $d_{\mathrm{pp},N_{\mathrm{min}}}$), secondly the numerical results are evaluated with respect to the experimental results and the typical assumptions of CDSMs, i.e. assuming spherical aggregates or constant primary particle size for all aggregates. Then, the sensitivity to the model parameters is investigated. Simulation results of F32 are compared to the measurement results found in the literature.

6.4.1 80% ethylene flame

The different cases considered to estimate the primary particle size for F80 are summarized in Table 6.4, with the indication of the case name, the low cut-off size ($d_{\mathrm{pp},N_{\mathrm{min}}}$), the method to obtain the PPSD (Prim.Part. model), if the surface rounding (Surf.R.) was considered or neglected, the type of characteristic diameter calculated (Mean) and the smallest aggregating particle BIN and its diameter ($d_{\mathrm{pp},N_{\mathrm{s}}}$).

Case	$d_{\mathrm{pp},N_{\mathrm{min}}}$	Prim. Part. model	Surf.R.	Mean	$d_{\mathrm{pp},N_{\mathrm{s}}}$
a	BIN_8 (5nm)	PPT	considered	geom	BIN_{12} (10 nm)
b	BIN_8 (5nm)	PPT	considered	mono	BIN_{12} (10 nm)
c	BIN_8 (5nm)	PPT	considered	amean	BIN_{12} (10 nm)
d	BIN_5 (2nm)	PPT	considered	geom	BIN_{12} (10 nm)
e	BIN_8 (5nm)	$d_{\mathrm{ag,pp}}$ =10 nm	-	geom	BIN_{12} (10 nm)
f	BIN_8 (5nm)	Vol. equiv. sphere	-	geom	BIN_{12} (10 nm)
g	BIN_8 (5nm)	PPT	neglected	geom	BIN_{12} (10 nm)
h	BIN_8 (5nm)	PPT	considered	geom	BIN_{10} (6.4 nm)
i	BIN_8 (5nm)	PPT	considered	geom	BIN_{14} (16 nm)

Table 6.4: *Numerical simulation cases for F80 according to the case name, the low cut-off size ($d_{pp,N_{min}}$), the method to obtain the PPSD (Prim.Part. model), if the surface rounding (Surf.R.) was considered or neglected, the type of characteristic diameter calculated (Mean) and the smallest aggregating particle BIN and its diameter (d_{pp,N_s})*

First, the impact of the retained definition for the mean d_{pp} is evaluated in cases a-b-c. In addition, the effect of the low cut-off size on the d_{pp} results can also be evaluated by comparing case d to case a. It should be noticed that the variability introduced by definition of mean diameter and the choice of $d_{\mathrm{pp},N_{\mathrm{min}}}$ is not due to the proposed procedure, but it is related to the general issue of correctly comparing experimental and numerical results. Results for these four cases are presented in Fig. 6.8 and it can be observed that the variability can be important and it has to be taken into account to perform a consistent validation of the numerical results.

Similarly to the 1D case, the monodisperse diameter (case b) is the largest, followed by the arithmetic mean diameter (case c) and by the count mean diameter (case a). The characteristics of the spatial distribution are very similar: the highest values are located on the wings, rapidly increasing between $\sim$1 and $\sim$2.5

cm HAB, and decreasing from ∼4 to ∼5 cm HAB. Along the centerline, after a rapid increase, a plateau of mean d_{pp} appears before the particles oxidation.

By comparing case a) to case d) it is possible to verify that the choice of the cut-off size may introduce a significant variability for the mean primary particle size, similarly to the 1D case investigated in Chapter 5. By choosing a smaller $d_{pp,N_{min}}$, the maximum diameter dropped from 22 nm to 17 nm and the whole spatial distribution is modified. In addition, in the inner region the d_{geom} shifted to lower values when considering $d_{pp,N_{min}}$ = 2 nm. As already stated, the choice of this parameter is mainly governed by the sensitivity of the experimental setup to capture the presence of the small particles. In this case, no information is provided by the authors in [84]. However, where large particles are present, small particles (below 5nm) are generally not expected to be detected by LII, especially for high delay times, as discussed in the literature [89, 186], and indicated by the analysis of Figure 5.14 in Section 5.5. As the ISF-coflow-laminar-3 series is characterized mainly by mean primary particle sizes significantly larger than 5 nm, it may be reasonable to assume that the contribution of small particles to the LII signal is negligible and then to consider $d_{pp,N_{min}}$ = 5 nm. Nevertheless, it is important for future validations to dispose of an indication of the experimental low cut-off size as the whole comparison can be biased by this choice.

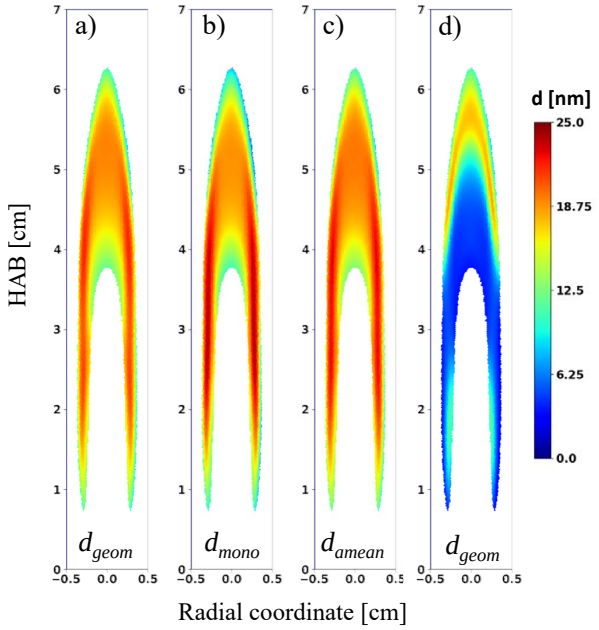

Figure 6.8: *Numerically determined d_{geom}, d_{mono} and d_{amean} for F80 (cases specified in Table 6.4)*

In order to evaluate the performances of the newly developed method for tracking the mean d_{pp}, numerical results are compared to the experimental data from Franzelli et al. [84] in Figure 6.9. Results obtained using the original mechanisms' description of d_{pp} [27] (case e) and assuming a spherical assumption (case f) are also provided in Figure 6.9 to highlight the interest of the proposed technique.

It can be observed that the implemented model (case a and b) gives a better es-

timation of d_{pp} than the previously applied assumptions, correctly localizing the maximum d_{pp} value in the flame wings, and providing a lower, almost constant, value along the flame centerline. On the contrary, for case d the distribution is homogeneously 10 nm, showing that in this case the contribution of small spherical particles to the mean d_{pp} is negligible compared to the aggregates. Though the spherical particle assumption (case e) provides larger maximal d_{geom}, as expected, the spatial distribution of d_{geom} is clearly unsatisfactory.

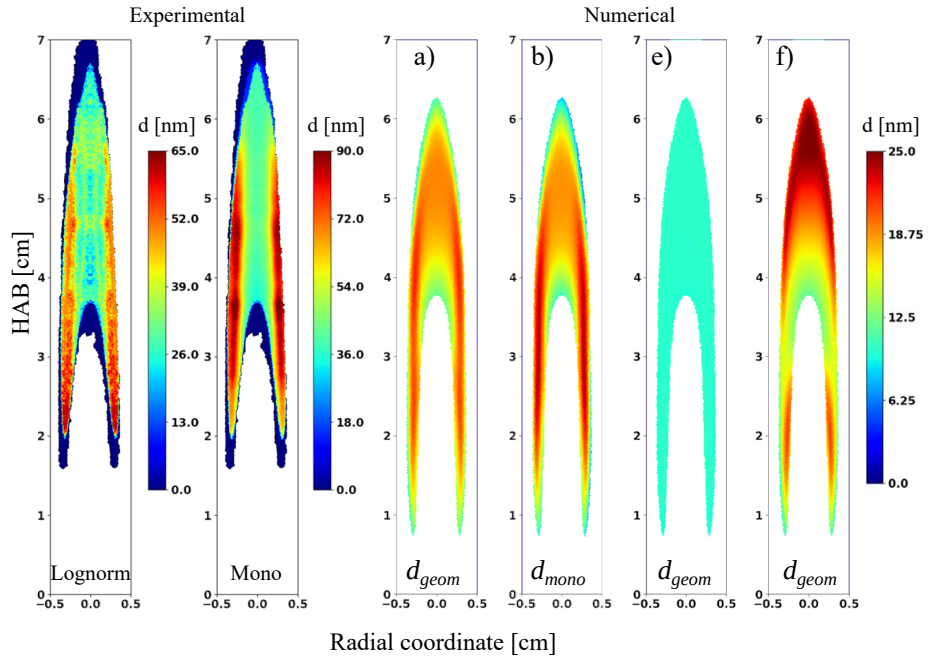

Figure 6.9: *Experimental results [84] on d_{pp} compared to the numerical results using the new strategy (cases a and b), assuming aggregates with constant d_{pp} (case e) and spherical particles (case f) for F80*

With the new model, the plateau of the d_{pp} value between ∼4.5 to ∼6.5 cm HAB along the centerline is observed in agreement with the measurements. The d_{pp} on the wings slightly decreases between ∼3.5 and ∼5 cm HAB both in the experiments and in the numerical simulation. The maximum value of d_{pp} is underestimated by a factor of ∼3 compared to the experimental values obtained by LII [84]. In addition, the contrast between the centerline and the wings is not that significant in the numerical results as in the experiments, both in terms of soot volume fraction and primary particle size. However, the dominance of the large particles on the wings is correctly captured, leading to a relevant improvement compared to the results with the original CDSM assumption and the spherical particle assumption. Furthermore, it has to be noticed that the TiRe-LII signal evaluation was performed with constant temperature assumption (1700 K) which may lead to an overestimation of the d_{pp} along the centerline where lower temperature values were detected by the pyrometry.

In addition to the LII measurement data [84], mean diameters obtained with TEM by Kempema et al. [77] are available at 3 locations on the centerline and 3

locations on the wings. In Figure 6.11, the numerical and the experimental mean d_{pp} is compared along the centerline and at the three TEM measurement heights on the wings. As the radial coordinates of the TEM probe locations were not provided, the values were extracted at maximum d_{pp} location of a given height. The numerical results show a quite good agreement with the TEM data both along the centerline and the wings. It should be reminded that it is well known that TEM and LII techniques do not strictly measure the same quantity and that some discrepancies can be observed among these two approaches [80, 84]. Consequently, it is not possible to discriminate what is the correct experimental database to be used to validate the model. However, it is possible to conclude that the numerical results are in a reasonable agreement compared to the experimental uncertainties.

The sensitivity to the choice of the smallest aggregating particle size was also tested. The variation of the d_{geom} is depicted in Figure 6.10. By modifying d_{pp,N_s} to 6.4 nm (case h) and 16 nm (case i), from the baseline 10 nm (case a), the values of d_{geom} are slightly modified. However, the characteristics of the spatial profile are unchanged.

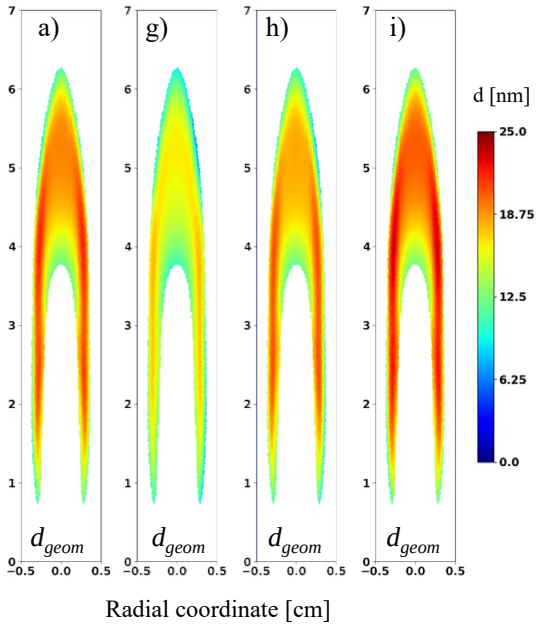

Figure 6.10: *Numerical d_{pp} results using the new strategy with different model parameters for F80*

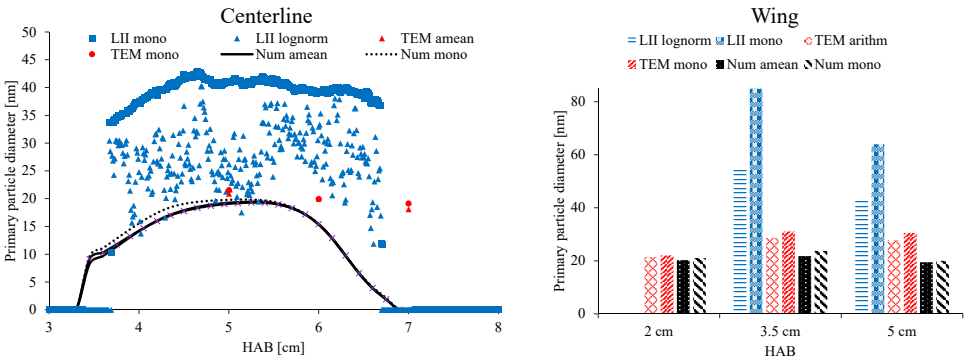

Figure 6.11: *d_{pp} along the centerline and at three HAB on the wing for F80. Comparison of numerical results to the LII results [84] and the TEM data [77]*

Sensitivity to model parameters

In order to clarify the relevance of the PPT procedure, it is important to discuss the sensitivity to its parameters. Therefore, as done for the premixed case, the effect of the surface rounding and the value of $d_{\mathrm{pp},N_\mathrm{s}}$ on the results is investigated here.

The role of the correction parameter for surface rounding can be determined by comparing case a) (considered) to case g) (neglected) in Figure 6.10. Due to the high contribution of condensation and surface growth processes, the correction for surface rounding significantly impacts the primary particle diameter, contrary to the premixed case shown in Section 5.3. When neglecting the surface rounding correction the maximum d_{geom} changes from ∼22 to ∼18.2 nm. This highlights the different nature of laminar coflow diffusion and premixed flames and the importance of introducing the C_r factor into the model.

6.4.2 32% ethylene flame

The evaluation of the Time-Resolved LII signal for F32 was performed by Foo et al. [188] (Adeilede) with assuming monodisperse PPSD and by Franzelli et al. [84] (EM2C) with both lognormal and monodisperse PPSD assumption (labeled with "lognorm" and "mono" respectively). The experimentally determined mean primary particle diameter of the two research groups deviates significantly (see Figure 6.12). There is almost a factor of ∼2 between the outcome of the two research groups' d_{mono}, which corroborate the larger error bars of the experimental approach. The experimental results show a quite rapid change in the diameter ∼2 mm downstream from the lower end of the sooty region, followed by a quite homogeneous distribution until close to the upper end of the sooty region. The experimental results of Franzelli et al. [84] have a region with a decreasing diameter of around 2.5 cm HAB near the centerline.

The numerical mean diameters with $d_{\mathrm{pp},N_{\mathrm{min}}}$ = 5 nm show a homogeneous spatial distribution similar to both measurements, however, the simulation without doubt underestimates the primary particle size. This may be explained by the fact that the soot volume fraction was under-predicted with a factor of ∼3-4. However, such a difference might not be fully originating from the f_v underestimation. A significant difference between the numerical d_{geom} predicted with

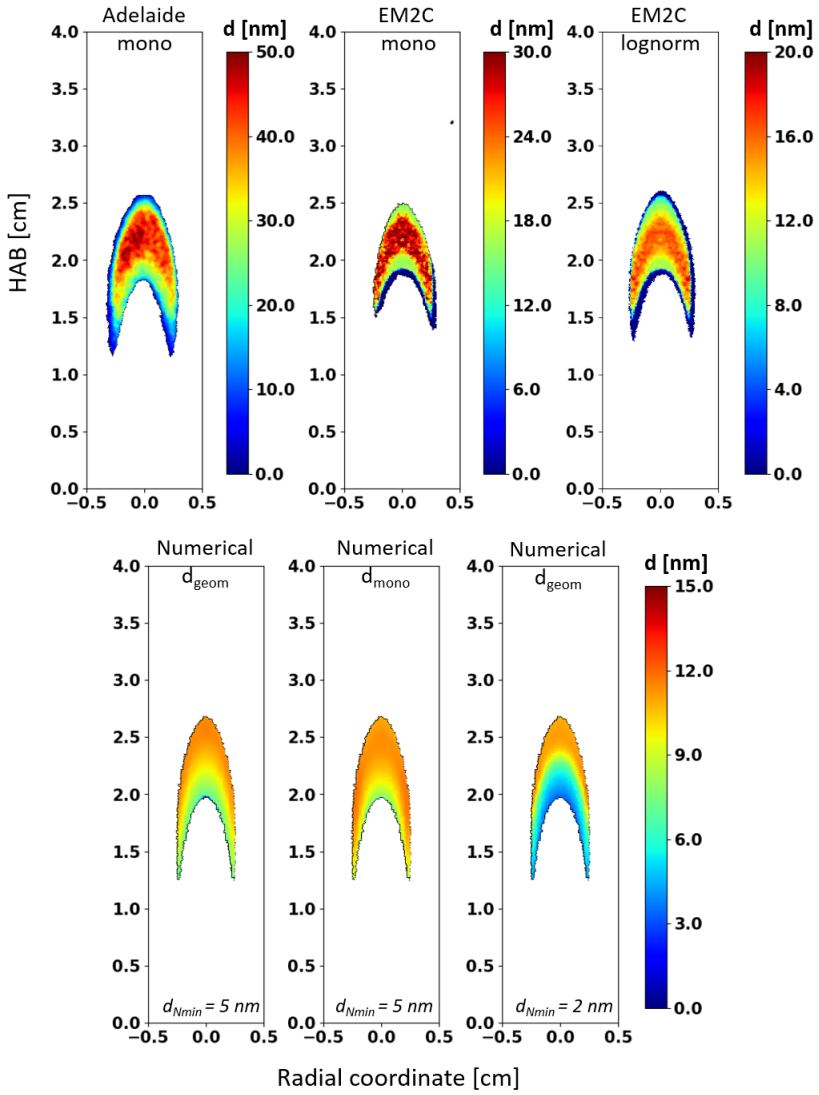

Figure 6.12: *Experimental [84, 188] and numerical primary particle size simulation for F32*

different lower cut-off sizes is present again in the lower sooty region (the first and the third numerical plot in Figure 6.12). The primary particle size observed at the experiments might indicate to use $d_{\mathrm{pp},N_{\mathrm{min}}}$ = 5 nm similarly to the F80 case, however in the lower sooty region the value of $d_{\mathrm{pp},N_{\mathrm{min}}}$ might not be obvious, due low amount of large particles. The novel method proposed in Section 4.2 can potentially help to overcome this issue.

Overall, it can be concluded that even if the quantitative d_{pp} values may depend on the model parameters and improvements of the CSDM description are still needed, the interest of the proposed tracking procedure is clearly proven since it allows to recover the spatial trend of d_{pp}, greatly improving the original description.

6.5 LII signal comparison

In this section, the measured and the synthesized LII signals are compared to reduce the uncertainties of the post-processing technique and potentially improve the consistency of the validation procedure for F80 and F32. The LII signal is reconstructed with the model presented in Section 2 using the characteristics of the laser at the measurement of Franzelli et al. [84]: laser wavelength = 1064 nm, fluence = 0.45 J/cm2, shot duration = 9 ns, camera gate = 0, exposure time = 25 ns, bandpass filter = 425$\pm$25 nm.

It is important to notice that due to the high fluence used in [84] the evaporation has to be accounted for when reconstructing the incandescence signal. This phenomenon is still not well understood. Therefore, the various vaporisation models can provide very different results [212] and the model parameters, which introduce further uncertainties, are numerous (see Table 4.2). As a result, the mismatch in signal decay at low delay times, where sublimation plays an important role in case of high fluence, can originate from the improper modeling of sublimation and/or the incorrect primary particle size distribution. On the contrary, the decay at larger delay times is driven only by the conduction and the radiation. These, on the one hand, result in the loss of information on the small particles due to considering only large decay times, as discussed in [89], on the other hand, provide a possibility to validate (or not) the PPSD on the larger diameter range.

The pictures of the LII signal were taken by a camera with an exposure time of 25 ns in [84]. Therefore, the pictures reconstructed from the numerical simulations were created by integrating the LII signal over the exposure time at each delay time. In the plots presented in Figure 6.13, the values are point wise normalized by the values of the picture belonging to the 0 ns delay.

6.5.1 80% ethylene flame

The experimental and numerically reconstructed fields are presented in Figure 6.13 for F80. The LII signal reconstruction was performed both with (Figure 6.13b) and without (Figure 6.13c) considering the shielding effect related to the number of particles in the aggregate (n_p) and by considering the PPSD only above 5 nm (Figure 6.13d), i.e. $d_{\mathrm{pp},N_\mathrm{min}}$ = 5 nm, and accounting for the shielding effect. The latter provided a marginal difference in terms of signal decay after 50 ns compared to accounting for the full PPSD, which confirms the expectation that the small particles do not contribute significantly to the LII signal when larger particles are present, especially for large decay times. Therefore, the choice of $d_{\mathrm{pp},N_\mathrm{min}}$ = 5 nm in Section 6.4.1 is justified.

The synthesized signal accounting for n_p provides a slower decay. However, there is still a notable discrepancy compared to the measured signal, confirming the underestimation of d_pp. Furthermore, it has to be noticed that the maximum value at 50 ns of the numerical and the experimental signals differs by a factor of $\sim$5. Due to the uncertainties related to evaporation modeling, the slower decay until 50 ns cannot be evaluated.

It is important to remind that the temperature profile was not well captured

for F80. Therefore, the reconstructed LII signal is characterized by large error bars. However, in the lower flame region and the wings, the signal is expected to be in good agreement with the measured value if the PPSD is well captured. As the numerical decay time is too short this confirms, the underestimation of the primary particle size in these regions.

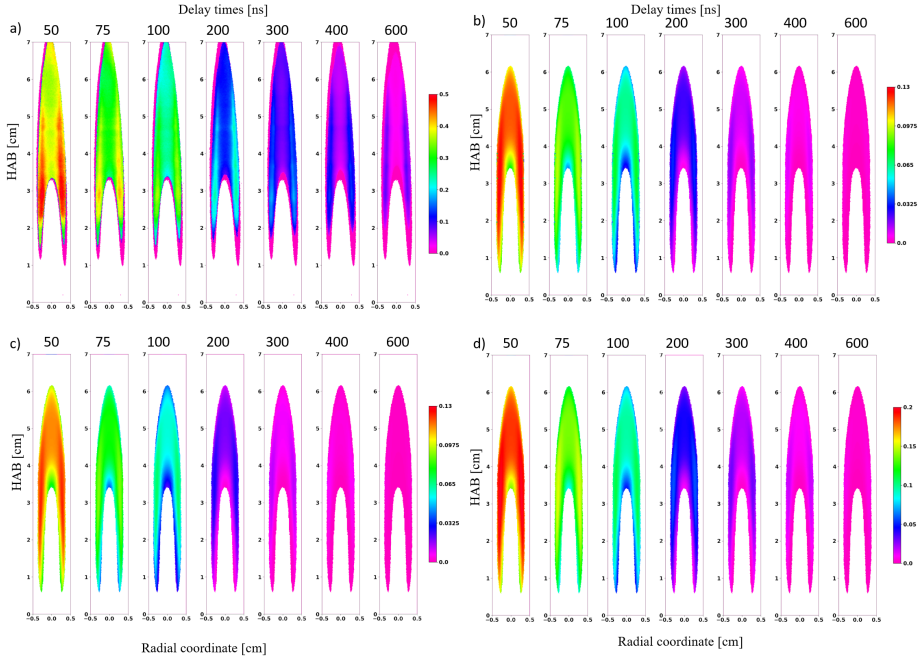

Figure 6.13: *Pictures of the LII signal for F80 at various decay times obtained by measurement [84] (a) and by synthesizing from the numerical PPSD with $d_{pp,N_{min}}$ = 2 nm considering (b) and neglecting (c) the shielding effect and by accounting for PPSD only above 5 nm and considering shielding (d)*

6.5.2 32% ethylene flame

The experimental [84] and numerical LII signals for F32 are presented in Figure 6.14a and b, respectively. The comparison confirms the under-prediction of large particle numerosity and/or size, as the measured signal is still observable at 200 ns delay time, contrary to the synthesized one. However, similarly to the F80 case, the variation of the low cut-off size did not influence significantly the signal at the presented delay times coinciding to the ones used in [84] to obtain the primary particle diameters. Therefore, once again the choice of $d_{\mathrm{pp},N_{\mathrm{min}}}$ = 5 nm is appropriate to perform the validation with the experimental d_{pp} of TiRe-LII. The homogeneous profile of the signal was well captured.

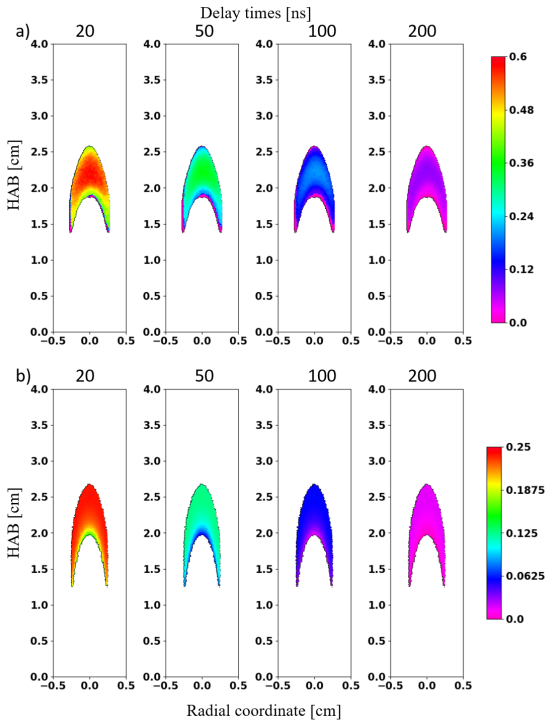

Figure 6.14: *Pictures of the LII signal for F32 at various decay times obtained by measurement [84] (a) and by synthesizing from the numerical PPSD with considering (b) the shielding effect*

6.6 Effect of dilution on the primary particle size

The effect of the dilution in the investigated flame on the soot volume fraction and temperature was studied by several researchers [84, 144, 241]. Here, in order to understand the effect of dilution on the primary particle size based on the obtained numerical results, first the flow-flame interaction is investigated. In the following, the variance of the flame structure, chemical processes and primary particle size with the decreasing dilution is analyzed with the help of the numerical simulation, furthermore, a possible explanation of the flame length underestimation is given. In specific, it is shown that the radial component plays an important role despite the dominant flow direction being parallel to the axis. Furthermore, with the help of analyzing the soot formation processes and the chemical heat release, the reason for the missing inner cooler core of F80 is revealed, which might be the explanation for the insufficient length of the flame. Finally, by analyzing the spatial intensity of the formation processes and the residence time in the various regions, the primary particle size change due to dilution is better understood.

6.6.1 Flow flame interaction

In Figure 6.15a the streamlines are showed overlapping the temperature profile for F32 and F80, and in Figure 6.15b the temperature and the radial velocity fields are reported for all the flames. The streamlines demonstrate that, though the radial velocity is not negligible compared to the inlet velocity (0.35 m/s), the flow direction is closely parallel to the axis in most of the domain.

In Figure 6.15b the contours are overlapped with the isoline where the ethylene mass fraction (W_{C2H4}) equals 1 ppm (W_1 white) to indicate the region where the fuel is still present in a significant amount. Also two temperature isolines, T = 1980 K and T = 2080 K, are sown (T black) to indicate the *cupola* discussed below. The flame region with high temperature (*region II*: $T > 1980K$) is surrounding the positive radial velocity region (*region I*: $U_{\mathrm{r}} > 0.001$) at F32 like a *cupola*. The location of *Region I* and *II* are demonstrated in Figure 6.15b F32.

With elevated ethylene content, the *cupola* becomes higher and initiates closer to the burner (F40). At F60 and F80 the *cupola* reaches the inlet and becomes detached from *region I* downstream, i.e. the volume embraced by *region II* does not posses everywhere a positive radial velocity component. At F80, the highest temperature region of the flame shifts from the centerline to the periphery, the *cupola* shape is no longer characteristic.

The downward extension of the *cupola* is the result of the advanced ignition due to elevated ethylene content, the start of the combustion region shifts closer to the inlet. The temperature increase of the gas parcel moving towards the combustion region leads to its intense expansion. This appears as a counterforce for the fuel stream. The higher the ethylene content, the higher the temperature increment and, therefore, the larger the expansion and counterforce against the fuel stream. At F60 and F80, the *cupola* reaches the inlet, and the combustion driven expansion overcomes the radial fuel flow at all heights.

At F32 and F40 the total amount of the ethylene is burned till the border of *region I*. However, at F60 the fuel cannot be burned on the circumference of *region I*, the excess of fuel leads to the upward shift of the top. *Region III* ($-0.001 \leq U_{\mathrm{r}} \leq 0.001$ and $W_{\mathrm{C2H4}} > 1$ ppm) appears, where the positive radial velocity is zero or almost zero, but ethylene is still available. The flame develops a flow parallel domain, usually referred to as the "wings", which is defined here as *Region IV*: $U_{\mathrm{r}} \leq -0.001$ and $W_{\mathrm{C2H4}} > 1$ ppm. These two new regions are even more extent at F80, therefore, they are clearly visible in Figure 6.15b F80.

The appearance of *Region III*, where the temperature is already elevated, but there is a lack of oxygen, provides the conditions required for pyrolysis [270]. Such an endothermic process might contribute to the presence of the cooler region along the centerline observed at the experiments [84, 144, 241]. The flux analysis of ethylene performed in the lower centerline region of F80 flame confirms the presence of intense pyrolysis (Figure 6.16). At 4 cm HAB, while 44.3% of ethylene is converted into cyclobutadiene (C_4H_4), 45% is converted into ethenyl and thereafter acetylene, and 10.4% directly to acetylene. The cyclobutadiene is then converted partly to 1,3-Butadienyl (C_4H_3) and partly to acetylene. At 5 cm HAB in F80 flame only 13.5% of ethylene is converted into cyclobutadiene and a significant 73.6% is converted into ethenyl and thereafter to acetylene, showing the decreasing intensity of pyrolysis.

In Figure 6.17 the chemical heat release rate is compared between F32 and F80 flames along the centerline. The significant difference in terms of chemical heat release profile in the sooty regions (indicated by the scattered lines in Figure 6.17) of F32 and F80 cases indicates a very different balance of endothermic and exothermic processes of the two flames. In F32 flame, the chemical heat release

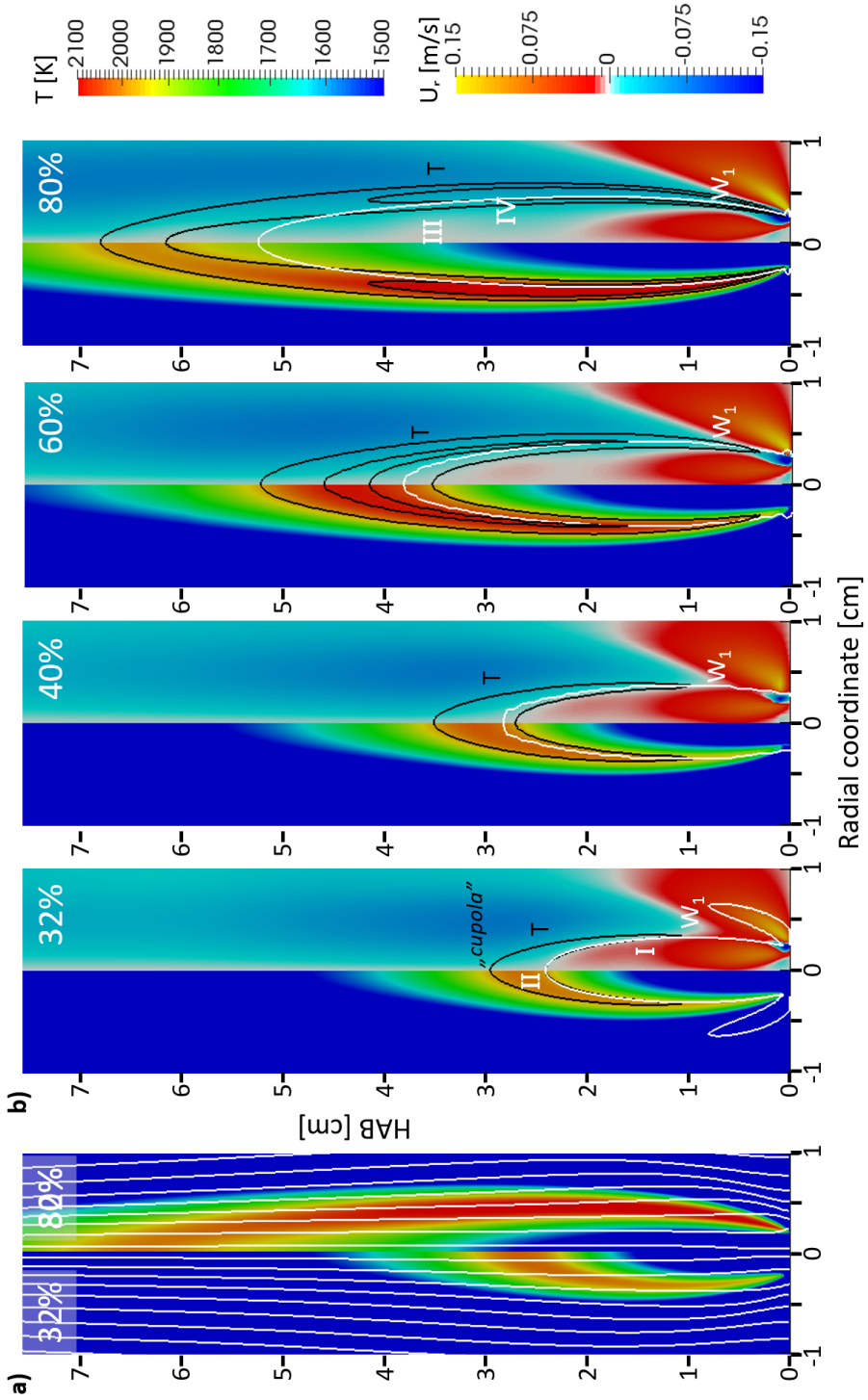

Figure 6.15: *a) explanation of regions b) Temperature and radial velocity profile with W_{C2H4} = 1ppm (W_1), Φ = 1 (Φ_1) isolines and streamlines with various inlet ethylene volumetric content (%) for ISF-coflow-laminar-3*

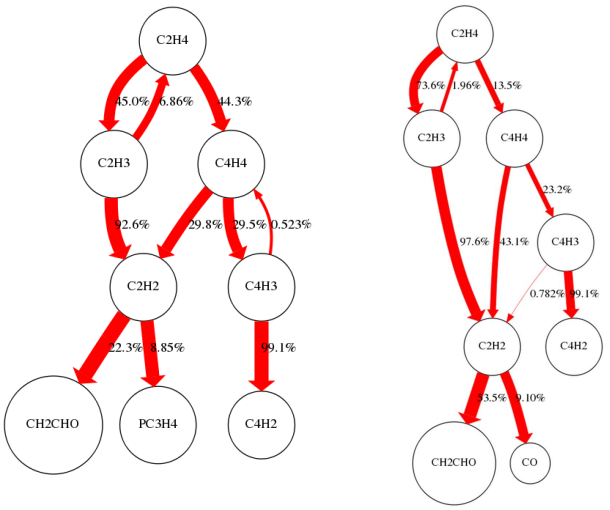

Figure 6.16: *Reaction flux analysis in F80 flame at HAB = 4 cm (left) and HAB = 5 cm (right) on the centerline*

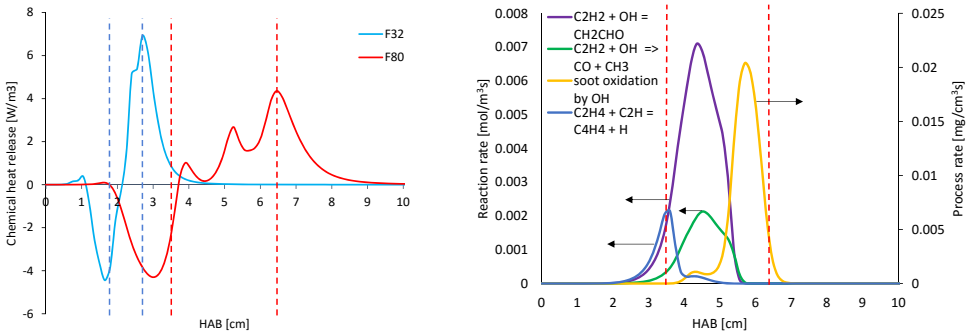

Figure 6.17: *Left panel: Chemical heat release rate in F80 and F32 flames along the centerline. Right panel: Reaction and process rates in F80 flame along the centerline. Dashed lines indicate the borders of the sooty region.*

shows a monotonic increase towards the peak temperature in the sooty region. On the contrary, in F80 flame, the chemical heat release reaches several local maxima and minima, i.e. the domination of exothermic or endothermic reactions is varying. As mentioned above pyrolysis is present at 4 cm HAB, however, the formation of cyclobutadiene from ethylene is significant only up to 5 cm HAB on the centerline (see Figure 6.17). The oxidation of acetylene by OH and most of the soot oxidation reactions by OH are endothermic too. The rate of these processes on the centerline in F80 flame are presented in Figure 6.17, where it can be observed that the peaks are coincident with the low heat release rate regions around 4.5 and 5.7 cm HAB. It has to be mentioned that the second drop of the heat release is present only if soot formation is accounted for, i.e. not only gas phase kinetics is considered, therefore, it is most probably connected to soot related processes. These are a few possible sources of a low heat release and consequently a moderate temperature. However, to draw further conclusions, a full heat balance analysis would be required, which is out of the scope of the current work.

Overall it can be concluded that the radial fuel stream velocity plays an important role close to the burner exit, and might strongly influence the evolution of the upper flame region. At low ethylene content, the ethylene is burned before the flow becomes fully parallel to the axis. With increasing the ethylene content the ignition advances. Consequently, the high-temperature region shifts towards the inlet rim, which hinders the radial flow of the fuel stream close to the inlet. With the increased fuel richness, the ethylene is not burned before the fuel stream becomes parallel to the axis, finally leading to the formation of *Region III* and *IV*. In *Region III* the conditions are suitable for pyrolysis which may contribute to the cooler inner region experimentally observed in F80.

It is interesting to recall that the transition of the soot peak from centerline to the wings was also observed by increased fuel jet velocity in the coflow flame study of Santoro et al. [163, 168]. The analogy of this case to the herein investigated flame series was already highlighted by Smooke et al. [144] and may be explained by the similarity in the radial velocity component change, despite that the changes are guided by different reasons for the two cases.

6.6.2 Effects on the mean primary particle diameter

The above-mentioned differences of the flame structure result in a significant variation between the spatial distribution and intensity of soot formation processes and consequently the d_{pp}. The four reference dilution values (32%, 40%, 60% and 80% of ethylene in the fuel mixture) are considered here. Experimental and numerical results of the d_{geom} are represented in Figure 6.18. Similarly to the F80 and F32, the quantitative values of d_{geom} are underestimated by a factor of 3-5 compared to the experiments for all the flames. Based on the difference between TEM and LII results, the important error bars (factor of 3 for F32) indicated by Franzelli et al. [84] and the numerical errors previously discussed, only a qualitative comparison is proposed here.

In terms of d_{pp} the trends of the experiment is correctly reproduced: a nearly homogeneous value of d_{geom} is retrieved for F32 and F40, whereas F60 and F80 cases are characterized by the presence of big particles localized in the flame wings. It should be noticed that a better agreement with experiments is expected by improving the kinetic mechanism prediction on f_{v} and by coupling the d_{pp} information to the reaction rates calculation. However, the main characteristics are well reproduced and the conclusions of the base evaluation are not expected to change significantly.

In the experimental work [84], it was inferred that the observed increase of f_{v} and d_{pp} levels in the flame wings with fuel present in the diluted mixture was due to two different phenomena: the increase of precursors concentrations and/or the change in the flame temperature. To validate (or not) the experimental conclusions, the temperature, the heavy PAH concentration, and the soot formation rate are compared for F32 and F80 in Figure 6.19. The flame temperature is presented in Figure 6.19a, together with isolines of 10% of the maximum rate for nucleation, mass growth[1], and oxidation to localize the different soot reaction zones. The field of heavy PAH (BIN_1-BIN_5) concentration is plotted in Figure 6.19b, whereas the soot inception rate and the total mass growth rate are presented in Figure 6.19c. The formation rates are one order smaller compared to the results obtained by Smooke et al. [144], which is reasonable considering the difference in the predicted soot volume fraction (up to a factor of $\sim$25)

By looking at the nucleation and growth regions in Figure 6.19a, it can be noticed that in both situations the soot mass production does not occur in the high-temperature region, so that the increase of the maximum temperature value does not seem to directly affect soot production and, consequently, the primary particle diameter size. On the contrary, soot production seems to be localized in a region where $T \approx 1800\ K$, whose extension increases with the ethylene content in the mixture as discussed in Section 6.6.1, leading to a higher total soot production, but not necessarily to a higher local peak of production in the flame wings.

By looking at Figure 6.19b, it can be observed that the concentration of soot precursors increases with the ethylene content. The formation rate increases downstream of the high heavy PAH concentration region, which may indicate the

[1] Sum of surface growth by condensation of PAH, heavy PAH and resonantly-stabilized radicals and the HACA-mechanism [27]

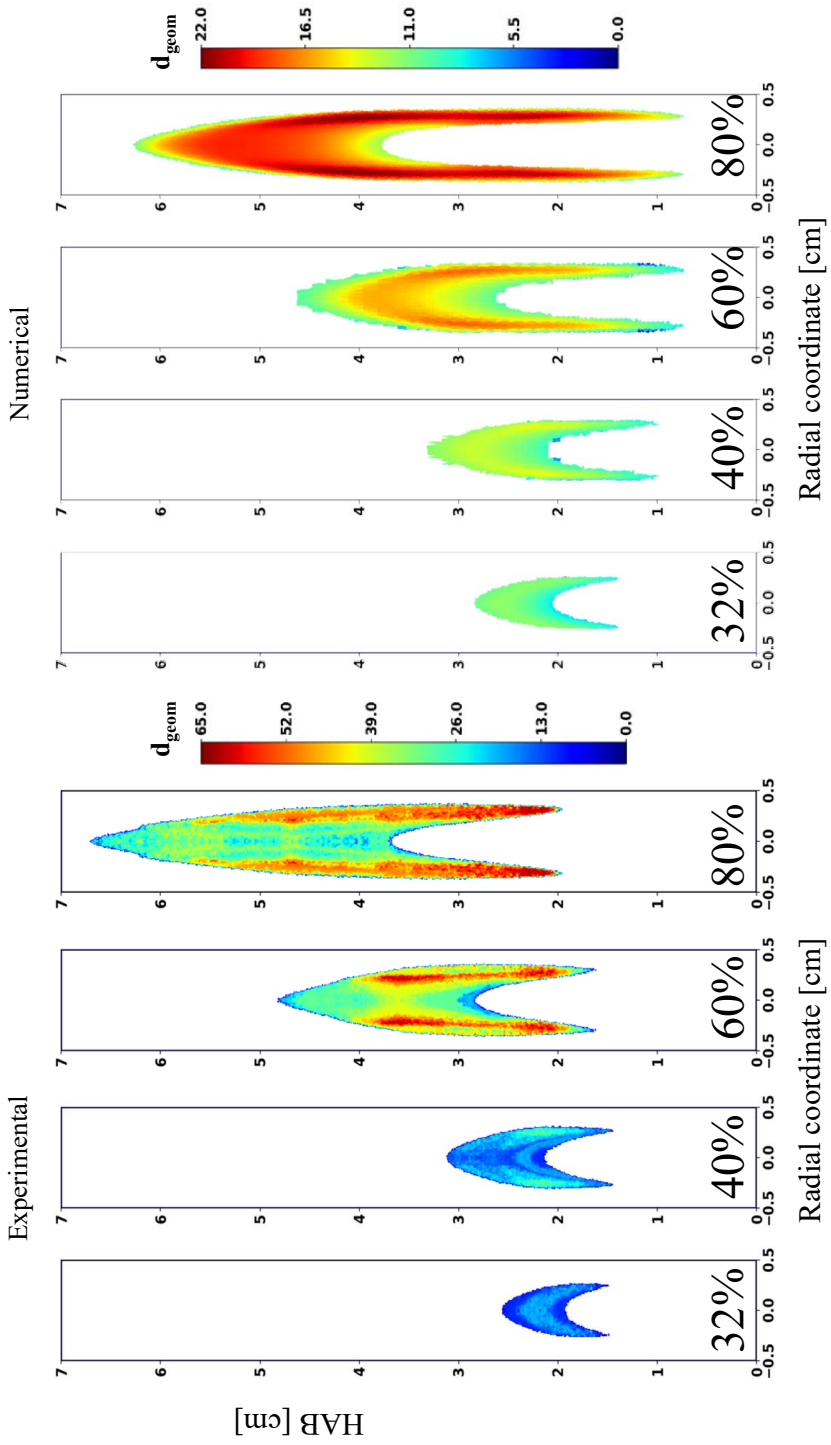

Figure 6.18: *Experimental [84] and numerical mean primary particle diameters (d_{geom}) for four dilutions.*

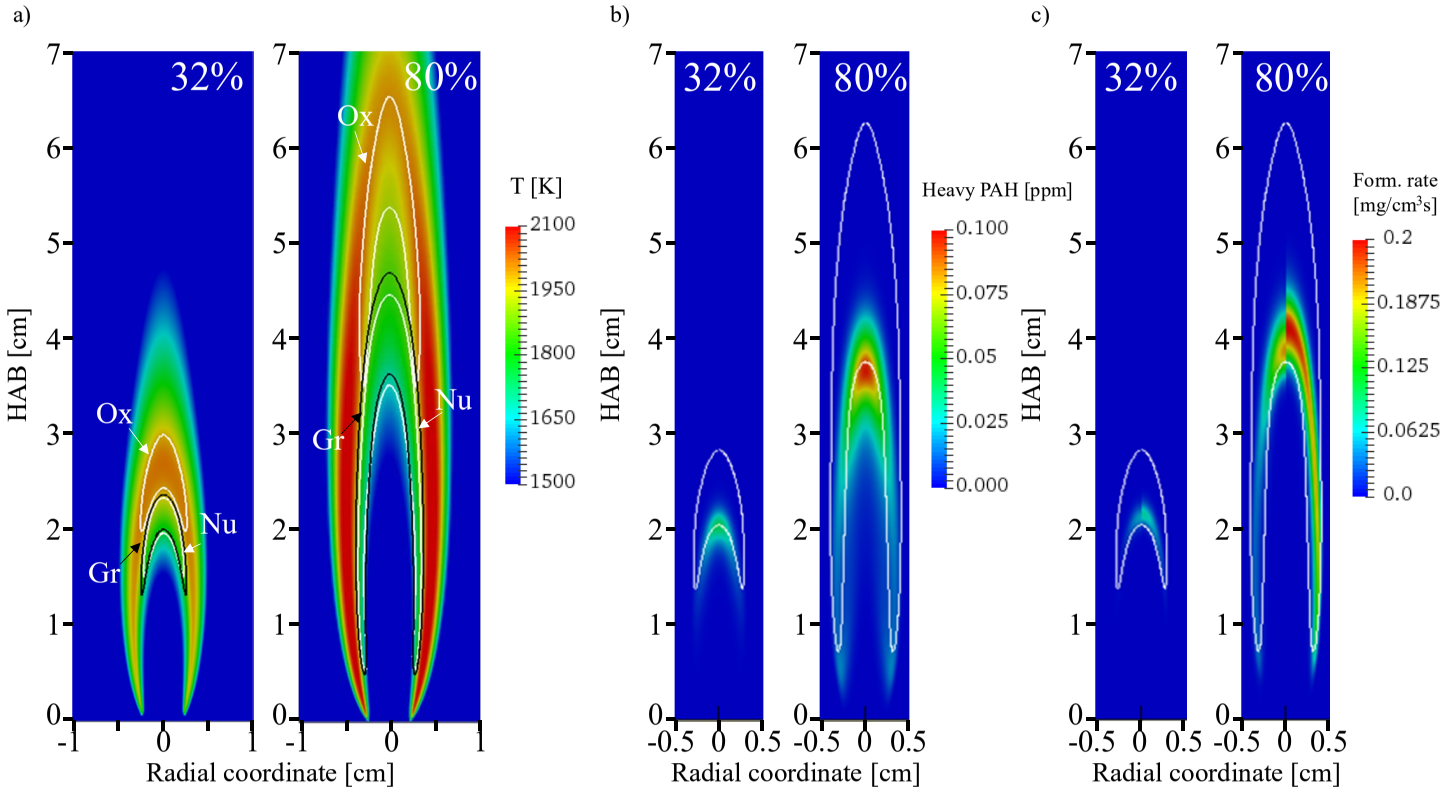

Figure 6.19: *ISF-coflow-laminar-3 F32 and F80: a) Isolines of nucleation (Nu-white), growth processes (Gr-black) and oxidation (Ox-white) intensity reaching 10% of maximum value with temperature distribution b) heavy PAH (BIN_1-BIN_5) concentrations with isoline $f_v = 0.01$ ppm c) soot inception (left) and growth process rates (right) with isoline $f_v = 0.01$ ppm*

connection between the increased ethylene content, the increased precursor concentration, the intensified growth process and finally the higher soot formation and d_{pp}. However, it should be noticed that the maximum of PAH concentration and growth rate is localized in the centerline also for F80, despite the maximum of d_{pp} is observed on the wings. Therefore, the increase of temperature and PAH concentration does not seem to be directly responsible for an increase of d_{pp} in the flame wings.

To understand the presence of the maximum mean d_{pp} value in the flame wings for the F80 case, it should be reminded that the d_{pp} depends not only on the local rates of the formation processes but also on the residence time of the fluid parcel in the growth and nucleation area. In analogy, the particle history will also affect the size of its primary particles. In Figure 6.20, the rate of growth processes and d_{geom} are plotted as a function of the residence time along the centerline for both the F32 (red) and the F80 (black). The link between HAB and residence time is indicated in Figure 6.20b. Along the centerline, both nucleation and growth show a profile consisting of a single peak. It can be observed that the formation of larger primary particles in the centerline for the F80 is on the one hand due to the increased intensity of growth process and on the other hand due to the increased time spent by the particles in the region of growth processes.

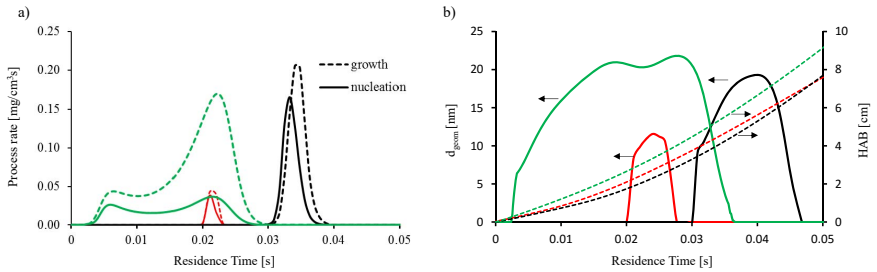

Figure 6.20: *ISF-coflow-laminar-3: a) nucleation and growth intensity b) d_{geom} and HAB along centerline for F32 (red) and F80 (black) and streamline crossing maximum d_{geom} location for F80 (green)*

In addition, to investigate the flame wings, a streamline has been chosen in a way that it passes through the location of the maximum d_{geom} for F80. The evaluation performed along the streamline is presented in Figure 6.20 in green. The scenario in the wings is more complex than the one from the centerline: nucleation and growth processes overlap for a wide time range and their shape deviates significantly from the trend along the centerline. Even if the peak of grow rate is similar along the centerline and the wings, the time spent by the particle in the wings is longer compared to the centerline so that bigger primary particles are formed.

By looking at results of Figure 6.20b., it is possible to observe that along the wings of F80 the d_{geom} strongly increases where the contribution of growth processes are significantly higher than soot inception. Then, between 20-25 ms residence time (2.8-3.5 cm HAB) the mean d_{pp} value slightly reduces with the HAB, before the intense oxidation of the soot begins. In this 'plateau' region the soot volume fraction is still increasing (Figure 6.4) but the mean d_{pp} value is al-

most constant due to the intense production of small particles that attenuates the effects of growth processes. The observed behavior is slightly in contradictions with the conclusions of Franzelli et al. [84], inferring a positive correlation between primary particle size and soot volume fraction. Even if this correlation is globally observed in the present simulations, this conclusion is not strictly verified everywhere in the flame.

6.7 Conclusions

The soot volume fraction of the investigated coflow laminar flame was underestimated by a factor of $\sim$3 for all four dilutions. However, the transition of the soot peak location from the centerline to the wings with the increasing ethylene content in the fuel stream was captured, and the extent of the sooty region was well predicted for F32 and F40 flames. For F60 and F80 flames the width of the sooty region was well predicted, however, the length of the region was underestimated.

The primary particle size was obtained by means of the PPT model proposed in Chapter 3. The sensitivity to the model and evaluation parameters, like the $d_{\mathrm{pp},N_\mathrm{s}}$, surface rounding and $d_{\mathrm{pp},N_\mathrm{min}}$, was investigated. While modifying $d_{\mathrm{pp},N_\mathrm{s}}$ had a moderate impact on the simulation results, the neglect of the surface rounding caused a significant drop in the resultant primary particle size. The choice of $d_{\mathrm{pp},N_\mathrm{min}}$, used to calculate the mean diameter, turned out to significantly influence the derived characteristic diameter. As the flame is generally characterized by large primary particles, the $d_{\mathrm{pp},N_\mathrm{min}}$ = 5 nm is a more appropriate choice when validating with the mean diameter derived from TiRe-LII, as it was confirmed by the LII signal comparison. The numerical mean diameter was $\sim$1.5-4.5 times smaller than the experimental results [77, 84, 188]. However, the measurement results obtained by the different research groups vary up to a factor of $\sim$2.

The effect of dilution on the flame structure and the primary particle size was analyzed. With the increased ethylene content the ignition time advances and the fuel cannot be burned close to the burner where the jet has a radial flow component, but reaches the region where the flow has negligible radial velocity component. This results in the development of a flow parallel combustion region. The effect on the primary particle size profile of the changing fuel stream dilution was captured qualitatively, however, the mean d_{pp} values were underestimated by a factor of $\sim$3 for all four dilutions.

From the discussed analysis, it can be concluded that the effect of dilution on the transition of d_{pp} peak values from the centerline to the flame wings cannot be linked in a straightforward manner to an increase of temperature and precursor concentration. The rate and location of the different soot formation and consumption processes change with the increase of ethylene content. This is not only due to differences in the flame structure but also in the streams' physical properties. In particular, the velocity field governing the trajectory of the particles and, consequently, their residence time in the growth regions.

CHAPTER 7

Conclusions

On the one hand, carbon black, the end product of the industrially controlled combustion of hydrocarbons is used in the production of several everyday objects, such as the car tires, mechanical rubber or as a color pigment in plastics, paints, and inks. On the other hand, soot, the undesired byproduct of combustion, is well known for its harmful effect on human health and environment. Inhaled soot particles penetrating into the respiratory system can cause several diseases and a positive correlation between their levels in the air and the cancer risks was found. Furthermore, soot particles emitted into the atmosphere can contribute to the accelerated snow melting and climate change.

Both at the utilization of these combustion generated particles and its negative effects on health and environment the surface of the particle plays an important role. As these particles tend to have a fractal like structure, consisting of numerous spherical shape building block, called primary particles, the information of the size of these primary particles can be used to determine their surface. Numerical simulations can help to better understand the evolution of the particle surface and the primary particle size distribution (PPSD), and they can help to design combustion systems with improved or decreased large surface particle formation, according to the needs. In the current work the main focus was on the soot formed from hydrocarbon fuels. The calculation of primary particle size by the numerical method provides a new aspect for the model validation. Furthermore, as both the surface related and the collisional processes, like the oxidation, the surface growth and the aggregation, depend on the primary particle size, the numerical model prediction may improve when the primary particle size is accounted for.

Soot formation is a very complex phenomenon as it is a combination of physical and chemical sub-processes (collision processes, nucleation, dehydrogena-

tion, surface growth, HACA mechanism and aggregation). On the one hand, this complexity must be reflected by the model adopted for numerical soot formation simulations. On the other hand, the model should not be computationally too expensive to be applicable in multidimensional laminar flames. The numerical investigation of such flames allows the analysis of the soot formation processes similar to those in the industrial applications on a lower computation cost. A possible approach, suitable for these requirements is the chemical discrete sectional model [27, 46, 104]. In this approach, the molecular mass range of heavy polycyclic aromatic hydrocarbons (PAHs) and soot is discretized into sections (BINs) represented by pseudo-species. Recent models may further subdivide these classes based on the hydrogenation level or to distinguish between molecules and radicals. However, they assume a spherical shape of the soot particles [47, 104, 154] or a spherical shape below a size limit and a constant primary particle size above this limit [124], whereas both were proven to be untrue by experimental investigations [24, 71–73, 77, 85, 88]. Therefore, the first objective of this work was to provide a numerical tool to estimate primary particle size by chemical discrete sectional models.

To obtain primary particle size by CDSMs, a new variable was introduced, the primary particle number density, and the related transport equation was derived. The chemical source term is based on the chemical reactions and the chemical reaction rates. The primary particle tracking (PPT) assumes point contact in between the primary particles in the aggregates. However, the proposed model takes into account the obliteration caused by surface growth and the similar effect of condensation by reducing the primary particle number in the aggregate when these processes take place. The PPT was incorporated into the CDSM developed by the CRECK Modeling Group [124] without the coupling between the kinetic mechanism and the results on the primary particle size. This means, the reaction rates were calculated based on the original assumption of the model on particle morphology (sphericity for the small particles and constant primary particle size for the aggregates).

For model validation, experimentally obtained mean primary particle size ($d_{\mathrm{pp,mean}}$) can be used as a reference. However, to validate $d_{\mathrm{pp,mean}}$ calculated from the numerical PPSD, the smallest considered diameter ($d_{\mathrm{pp},N_{\mathrm{min}}}$) should match the size of the smallest particle detected ($d_{\mathrm{pp},N_{\mathrm{min}}}$) by the experimental investigation. The latter quantity depends on the experimental approach and may differ even for the same methodology. In Transmission Electron Microscope (TEM) analysis of the thermophoretically samples soot particles the $d_{\mathrm{pp},N_{\mathrm{min}}}$ depends on the resolution of the microscope or may be biased by the liquid-like particles [98]. In Time-Resolved Laser-Induced Incandescence (TiRe-LII) $d_{\mathrm{pp},N_{\mathrm{min}}}$ may depend on the PPSD itself, as with the transition of the PPSD from unimodal to bimodal the influence of small particles on the signal slowly decreases and finally falls below the signal-to-noise ratio. Furthermore, particles of a few nanometer may not emit a signal detectable by the detection system [191] in one case but were found detectable in another case [186], which may be related to the varying optical properties of soot particles vary. This results that by TiRe-LII it is not possible to identify bimodality [244] and the exact value of the smallest detectable diameter

($d_{\text{det,min}}$) is still uncertain.

Validation with TiRe-LII, this nowadays popular laser diagnostic technique to determine primary particle size, is affected by further uncertainties as the primary particle size is not directly measured, but derived through post-processing operations from the incandescence signal (inverse method). The post-processing is done by comparing the numerically reconstructed incandescence signal of various possible PPSDs to the experimentally detected. The PPSD minimizing the error between the two signals, therefore, possibly identical with the PPSD emitting the detected signal, is sought. This approach requires several additional input parameters beside the incandescence signal, which leads either to the need of additional measurements or to the assumption of these parameters. Both might further increase the error bars. The related uncertainties were highlighted in this work by overviewing earlier studies and by performing additional sensitivity analysis. It was proven that, when primary particle number in the aggregate is not considered or the molecular weight of the gas phase is not properly assumed, correct PPSDs might be considered invalid. Or, when the numerical monodisperse equivalent mean diameter is compared to the experimental diameter derived with monodisperse PPSD assumption, the model might fail the validation test despite well predicting the total number of primary particles and consequently d_{mono}. One of the main drawbacks of this approach is that the shape of the PPSD has to be assumed in advance, which was proven to be not lognormal at all times, as often supposed.

Many of the input parameters to model the LII signal are generally available with good reliability from the numerical simulations where the primary particle size is accessible. To ensure a more comprehensive validation, an additional approach was proposed. This is based on directly comparing the detected incandescence signal to the one reconstructed from the numerical results (forward method). The uncertainty related to the smallest detected particle size ($d_{\text{pp},N_{\text{min}}}$) is circumvented, i.e. the low cut-off size ($d_{\text{pp},N_{\text{min}}}$) to calculate the mean diameter does not have to be defined. However, it has to be kept in mind, that, as the same LII signal decay might correspond to various PPSDs, the agreement between synthesized and measured signal does not ensure the validity of the PPSD. Nevertheless, the mismatch can be used to exclude the incorrect PPSDs and add further indication for the kinetic mechanism development.

The combined model of the CRECK Modeling Group's kinetic mechanism [124] and the PPT was tested on ISF target flames [123]: a premixed laminar ethylene flame and a coflow diffusion ethylene flame series with various dilutions (32% (F32), 40% (F40), 60% (F60), and 80% (F80) ethylene content respect to the volume in the fuel stream). The latter provides the possibility to investigate the primary particle size change for the transition from a lightly sooting to a heavily sooting flame.

The effect of changing $d_{\text{pp},N_{\text{min}}}$ was investigated for both the premixed flame, and the F32 and F80 coflow flames. The influence of the change from 2 nm to 5 nm was significant, resulting in a considerable uncertainty at the traditional validation method. The predicted d_{mean} showed moderate sensitivity to the smallest aggregating particle size ($d_{\text{pp},N_{\text{s}}}$) for both the premixed flame and F80. The results confirmed that, despite obtaining a general shift in the average diameter, the

overall trend in the spatial distribution does not change for a $\sim$50% modification of $d_{\mathrm{pp},N_\mathrm{s}}$. On the contrary, the surface rounding was found to play an important role at F80 coflow flame. However, its effect at the premixed flame remained moderate.

The soot volume fraction was well predicted for the premixed flame (within the uncertainty limits) and the numerically obtained mean primary particle size showed good agreement with the experimental results [85, 88, 183, 244]. The agreement with the TiRe-LII results of Bladh et al. [88] was less satisfying compared the ones with TEM. However, the source of disagreement could not be certainly identified due to the uncertainties of this validation approach. The novel validation approach allowed us to gain further knowledge about the PPT model validity. It was found that the transition of the PPSD from unimodal to bimodal is mistaken by the numerical simulation. Furthermore, the analysis confirmed that at high HABs the primary particle size is underestimated.

An additional simulation was performed by modifying the imposed temperature profile in the region where measurements by Bladh et al. [88] were available. The simulations with the updated profile resulted in a marginal change in terms of soot volume fraction and in minor differences in the mean primary particle diameter. Due to the lower inception rate in the upper flame region for the "Bladh 2011" case, on the one hand, the probability of the small particles became lower, on the other hand, the second peak of the PPSD was shifted to smaller values due to the lower condensation rate. Overall, the change resulted in a more flat mean d_{pp} profile in the upper flame region, which is in better agreement with the TEM results [88].

Regarding the ISF-coflow-laminar-3 flame, the soot volume fraction was under-predicted by a factor of $\sim$3-4 for all four dilutions. Similarly, the d_{pp} values are smaller than the LII experimental data [84, 188] by a factor of 2-4, and slightly smaller than the TEM results [77], indicating that improvements of the CDSM are needed. The comparison of the experimental and synthesized LII signal decays justified the usage of $d_{\mathrm{pp},N_\mathrm{min}}$ = 5 nm for both F80 and F32 flame validations.

Despite the under-prediction of the mean d_{pp}, it has been shown that the new method is providing a qualitative agreement for all dilutions contrary to the results obtained with the typical assumptions of CDSMs, i.e. assuming spherical aggregates or constant primary particle size for all aggregates.

To understand the effect of dilution on the d_{pp} first the flame-flow interaction of the four cases were put under the scope. Despite the common appellation, diffusion flame, the radial velocity component was proven to play an important role. In particular, it was shown that for low ethylene content flames the hight temperature region of the flame is "seated" on the positive radial velocity region. The increase of fuel stream richness leads to the advancement of ignition time resulting the high temperature region to initiate closer to the burner, specifically to the edge of the fuel outlet. This provides a counterforce to the radial flow of the fuel stream due to the thermal expansion and, consequently, the fuel stream is oriented more axially. The lack of radial velocity and the excess of fuel results in a flow parallel flame region and an inner cooler region with intense pyrolysis.

The modified dilution, consequently the modified flame structure, causes chan-

ges in both formation process rates and fuel parcel residence times in the various soot formation regions. Their combined effect on the primary particle size was explained by analyzing different pathlines in F32 and F80 flames. The analysis of the pathline crossing the wings in F80 revealed the reason of mean primary particle size decrement in the upper part of the wings where soot volume fraction is still increasing: the birth of small particles due to the intense inception. This also means that, despite the globally observed positive correlation between primary particle size and soot mass fraction, also inferred by Franzelli et al. [84], this rule is not strictly verified.

Overall it can be concluded that the PPT was shown to be a promising tool for evaluating primary particle size in numerical simulation of flames where CDSM is applied. A better understanding of the particle formation was possible by combining the knowledge gained about the soot formation processes by using the CDSM and the PPT. Furthermore, the new validation approach was proven to be useful at performing validation in the region of the transition from unimodal to bimodal PPSD.

As a future work, in order to improve the performance of the kinetic mechanism, the coupling between the predicted primary particle size and the chemical reaction coefficients should be implemented. Furthermore, to investigate the error introduced by not resolving the primary particle size distribution in a single mass section, either a multiple ρ_{pp} per mass section model or a second variable describing the variance in the mass section would be advantageous. Combining the proposed primary particle analysis with other kinetic mechanisms might be also a target of interest.

The potential improvement of the new validation approach is related to the thermal-accommodation coefficient, which remained one of the sources of uncertainty in the novel approach. The dependency of α_{T} on the maturity of soot is known [85, 245], but a general relation between hydrogenation and α_{T} is not established yet. Once the relation is found, the reconstruction can be done with a H/C dependent thermal-accommodation coefficient, providing accurate predictions even in the presence of a nascent and mature soot particle mixture.

Bibliography

[1] J. P. Putaud, R. Van Dingenen, A. Alastuey, H. Bauer, W. Birmili, J. Cyrys, H. Flentje, S. Fuzzi, R. Gehrig, H. C. Hansson, R. M. Harrison, H. Herrmann, R. Hitzenberger, C. Hüglin, A. M. Jones, A. Kasper-Giebl, G. Kiss, A. Kousa, T. A. Kuhlbusch, G. Löschau, W. Maenhaut, A. Molnar, T. Moreno, J. Pekkanen, C. Perrino, M. Pitz, H. Puxbaum, X. Querol, S. Rodriguez, I. Salma, J. Schwarz, J. Smolik, J. Schneider, G. Spindler, H. ten Brink, J. Tursic, M. Viana, A. Wiedensohler, and F. Raes, "A European aerosol phenomenology - 3: Physical and chemical characteristics of particulate matter from 60 rural, urban, and kerbside sites across Europe," *Atmospheric Environment*, vol. 44, pp. 1308–1320, mar 2010.

[2] G. Myhre, C. E. L. Myhre, B. H. Samset, and T. Storelvmo, "Aerosols and their Relation to Global Climate and Climate Sensitivity," *Nature Education*, no. May, pp. 1–11, 2015.

[3] T. C. Bond and R. W. Bergstrom, "Light Absorption by Carbonaceous Particles: An Investigative Review," *Aerosol Science and Technology*, vol. 40, pp. 27–67, jan 2006.

[4] M. O. Andreae, C. D. Jones, and P. M. Cox, "Strong present-day aerosol cooling implies a hot future," *Nature*, vol. 435, pp. 1187–1190, jun 2005.

[5] U. Pöschl, "Atmospheric aerosols: Composition, transformation, climate and health effects," *Angewandte Chemie - International Edition*, vol. 44, pp. 7520–7540, nov 2005.

[6] M. O. Andreae and D. Rosenfeld, "Aerosol-cloud-precipitation interactions. Part 1. The nature and sources of cloud-active aerosols," *Earth-Science Reviews*, vol. 89, pp. 13–41, jul 2008.

[7] P. Chýlek, V. Ramaswamy, and V. Srivastava, "Albedo of soot-contaminated snow," *Journal of Geophysical Research*, vol. 88, p. 10837, dec 1983.

[8] S. G. Warren, "Impurities in Snow: Effects on Albedo and Snowmelt (Review)," *Annals of Glaciology*, vol. 5, pp. 177–179, jan 1984.

[9] J. Hansen and L. Nazarenko, "Soot climate forcing via snow and ice albedos," *Proceedings of the National Academy of Sciences*, vol. 101, pp. 423–428, jan 2004.

[10] O. L. Hadley and T. W. Kirchstetter, "Black-carbon reduction of snow albedo," *Nature Climate Change*, vol. 2, pp. 437–440, jun 2012.

[11] C. Magono, T. Endoh, F. Ueno, S. Kubota, and M. Itasaka, "Direct observations of aerosols attached to falling snow crystals," *Tellus*, vol. 31, pp. 102–114, apr 1979.

[12] M. Kumai, "Identification of Nuclei and Concentrations of Chemical Species in Snow Crystals Sampled at the South Pole," *Journal of the Atmospheric Sciences*, vol. 33, pp. 833–841, may 1976.

[13] C. Sergent, E. Pougatch, M. Sudul, and B. Bourdelles, "Experimental investigation of optical snow properties," *Annals of Glaciology*, vol. 17, pp. 281–287, jan 1993.

[14] J. Hansen, R. Ruedy, M. Sato, M. Imhoff, W. Lawrence, D. Easterling, T. Peterson, and T. Karl, "A closer look at United States and global surface temperature change," *Journal of Geophysical Research: Atmospheres*, vol. 106, pp. 23947–23963, oct 2001.

[15] M. G. Flanner, C. S. Zender, J. T. Randerson, and P. J. Rasch, "Present-day climate forcing and response from black carbon in snow," *Journal of Geophysical Research*, vol. 112, p. D11202, jun 2007.

[16] M. A. Cole, R. J. Elliott, and K. Shimamoto, "Industrial characteristics, environmental regulations and air pollution: An analysis of the UK manufacturing sector," *Journal of Environmental Economics and Management*, vol. 50, pp. 121–143, jul 2005.

[17] D. D. Moore, G. D. G. D. Robson, and A. P. J. Trinci, "21st century guidebook to fungi," *Choice Reviews Online*, vol. 49, pp. 49–3854–49–3854, mar 2012.

[18] N. A. Janssen, M. E. Gerlofs-Nijland, T. Lanki, R. O. Salonen, F. Cassee, G. Hoek, P. Ischer, B. Brunekreef, and M. Krzyzanowski, *Health effects of black carbon*. 2012.

[19] M. Krzyzanowski, B. Kuna-Dibbert, and J. Schneider, *Health effects of transport-related air pollution*. World Health Organization Europe, 2005.

[20] M. Shiraiwa, K. Selzle, and U. Pöschl, "Hazardous components and health effects of atmospheric aerosol particles: Reactive oxygen species, soot, polycyclic aromatic compounds and allergenic proteins," *Free Radical Research*, vol. 46, pp. 927–939, aug 2012.

[21] A. Y. Watson and P. A. Valberg, "Carbon black and soot: Two different substances," *American Industrial Hygiene Association Journal*, vol. 62, no. 2, pp. 218–228, 2001.

[22] C. M. Long, M. A. Nascarella, and P. A. Valberg, "Carbon black vs. black carbon and other airborne materials containing elemental carbon: Physical and chemical distinctions," *Environmental Pollution*, vol. 181, pp. 271–286, 2013.

[23] R. J. McCunney, H. J. Muranko, C. M. Long, A. K. Hamade, P. A. Valberg, and P. Morfeld, "Carbon Black," in *Patty's Toxicology*, pp. 429–454, Hoboken, NJ, USA: John Wiley & Sons, Inc., aug 2012.

[24] J. Lahaye, "Particulate carbon from the gas phase," *Carbon*, vol. 30, no. 3, pp. 309–314, 1992.

[25] M. Kholghy, M. Saffaripour, C. Yip, and M. J. Thomson, "The evolution of soot morphology in a laminar coflow diffusion flame of a surrogate for Jet A-1," *Combustion and Flame*, vol. 160, no. 10, pp. 2119–2130, 2013.

[26] M. R. Kholghy, A. Veshkini, and M. J. Thomson, "The core-shell internal nanostructure of soot - A criterion to model soot maturity," *Carbon*, vol. 100, pp. 508–536, apr 2016.

[27] C. Saggese, S. Ferrario, J. Camacho, A. Cuoci, A. Frassoldati, E. Ranzi, H. Wang, and T. Faravelli, "Kinetic modeling of particle size distribution of soot in a premixed burner-stabilized stagnation ethylene flame," *Combustion and Flame*, vol. 162, no. 9, pp. 3356–3369, 2015.

[28] A. D'Alessio, A. D'Anna, G. Gambi, and P. Minutolo, "The spectroscopic characterisation of UV absorbing nanoparticles in fuel rich soot forming flames," *Journal of Aerosol Science*, vol. 29, no. 4, pp. 397–409, 1998.

[29] A. D'Anna, "Combustion-formed nanoparticles," *Proceedings of the Combustion Institute*, vol. 32 I, no. 1, pp. 593–613, 2009.

[30] A. D'Anna, M. Alfè, B. Apicella, A. Tregrossi, and A. Ciajolo, "Effect of fuel/air ratio and aromaticity on sooting behavior of premixed heptane flames," *Energy and Fuels*, vol. 21, no. 5, pp. 2655–2662, 2007.

[31] M. Commodo, L. A. Sgro, P. Minutolo, and A. D'Anna, "Characterization of combustion-generated carbonaceous nanoparticles by size-dependent ultraviolet laser photoionization," *Journal of Physical Chemistry A*, vol. 117, no. 19, pp. 3980–3989, 2013.

[32] R. A. Dobbins and C. M. Megaridis, "Morphology of Flame-Generated Soot As Determined by Thermophoretic Sampling," *Langmuir*, vol. 3, pp. 254–259, mar 1987.

[33] C. M. Megaridis and R. A. Dobbins, "Soot aerosol dynamics in a laminar ethylene diffusion flame," *Symposium (International) on Combustion*, vol. 22, pp. 353–362, jan 1989.

[34] R. A. Dobbins, "Hydrocarbon Nanoparticles Formed in Flames and Diesel Engines," *Aerosol Science and Technology*, vol. 41, pp. 485–496, apr 2007.

[35] M. Schenk, S. Lieb, H. Vieker, A. Beyer, A. Gölzhäuser, H. Wang, and K. Kohse-Höinghaus, "Morphology of nascent soot in ethylene flames," *Proceedings of the Combustion Institute*, vol. 35, pp. 1879–1886, jan 2015.

[36] H. Wang, "Formation of nascent soot and other condensed-phase materials in flames," *Proceedings of the Combustion Institute*, vol. 33, no. 1, pp. 41–67, 2011.

[37] J. P. Cain, P. L. Gassman, H. Wang, and A. Laskin, "Micro-FTIR study of soot chemical composition - Evidence of aliphatic hydrocarbons on nascent soot surfaces," *Physical Chemistry Chemical Physics*, vol. 12, pp. 5206–5218, may 2010.

[38] A. D. Abid, E. D. Tolmachoff, D. J. Phares, H. Wang, Y. Liu, and A. Laskin, "Size distribution and morphology of nascent soot in premixed ethylene flames with and without benzene doping," *Proceedings of the Combustion Institute*, vol. 32 I, no. 1, pp. 681–688, 2009.

[39] P. Desgroux, A. Faccinetto, X. Mercier, T. Mouton, D. Aubagnac Karkar, and A. El Bakali, "Comparative study of the soot formation process in a "nucleation" and a "sooting" low pressure premixed methane flame," *Combustion and Flame*, vol. 184, pp. 153–166, oct 2017.

[40] M. Wartel, J. F. Pauwels, P. Desgroux, and X. Mercier, "Pyrene measurements in sooting low pressure methane flames by jet-cooled laser-induced fluorescence," *Journal of Physical Chemistry A*, vol. 115, no. 49, pp. 14153–14162, 2011.

[41] S. Grimonprez, A. Faccinetto, S. Batut, J. Wu, P. Desgroux, and D. Petitprez, "Cloud condensation nuclei from the activation with ozone of soot particles sampled from a kerosene diffusion flame," *Aerosol Science and Technology*, vol. 52, no. 8, pp. 814–827, 2018.

[42] C. S. McEnally, L. D. Pfefferle, B. Atakan, and K. Kohse-Höinghaus, "Studies of aromatic hydrocarbon formation mechanisms in flames: Progress towards closing the fuel gap," *Progress in Energy and Combustion Science*, vol. 32, pp. 247–294, jan 2006.

[43] H. F. Calcote, "Mechanisms of soot nucleation in flames-A critical review," *Combustion and Flame*, vol. 42, pp. 215–242, jan 1981.

[44] H. Richter and J. B. Howard, "Formation of polycyclic aromatic hydrocarbons and their growth to soot-a review of chemical reaction pathways," *Progress in Energy and Combustion Science*, vol. 26, pp. 565–608, aug 2000.

[45] M. Frenklach, "Method of moments with interpolative closure," *Chemical Engineering Science*, vol. 57, pp. 2229–2239, jun 2002.

[46] A. D'Anna, "Detailed kinetic modeling of particulate formation in rich premixed flames of ethylene," *Energy and Fuels*, vol. 22, pp. 1610–1619, may 2008.

[47] M. Sirignano, J. Kent, and A. D'Anna, "Modeling Formation and Oxidation of Soot in Nonpremixed Flames," *Energy & Fuels*, vol. 27, no. 4, pp. 2303–2315, 2013.

[48] C. Russo, A. Tregrossi, and A. Ciajolo, "Dehydrogenation and growth of soot in premixed flames," *Proceedings of the Combustion Institute*, vol. 35, pp. 1803–1809, jan 2015.

[49] M. M. Maricq, "An examination of soot composition in premixed hydrocarbon flames via laser ablation particle mass spectrometry," *Journal of Aerosol Science*, vol. 40, pp. 844–857, oct 2009.

[50] T. C. Williams, C. R. Shaddix, K. A. Jensen, and J. M. Suo-Anttila, "Measurement of the dimensionless extinction coefficient of soot within laminar diffusion flames," *International Journal of Heat and Mass Transfer*, vol. 50, no. 7-8, pp. 1616–1630, 2007.

[51] J. Cain, A. Laskin, M. R. Kholghy, M. J. Thomson, and H. Wang, "Molecular characterization of organic content of soot along the centerline of a coflow diffusion flame," *Physical Chemistry Chemical Physics*, vol. 16, pp. 25862–25875, nov 2014.

[52] J. Mckinnon, E. Meyer, and J. B. Howard, "Infrared analysis of flame-generated PAH samples," *Combustion and Flame*, vol. 105, pp. 161–166, apr 1996.

[53] C. Russo, M. Alfe, J. N. Rouzaud, F. Stanzione, A. Tregrossi, and A. Ciajolo, "Probing structures of soot formed in premixed flames of methane, ethylene and benzene," *Proceedings of the Combustion Institute*, vol. 34, pp. 1885–1892, jan 2013.

[54] C. Russo, F. Stanzione, A. Tregrossi, M. Alfè, and A. Ciajolo, "The effect of temperature on the condensed phases formed in fuel-rich premixed benzene flames," *Combustion and Flame*, vol. 159, pp. 2233–2242, jul 2012.

[55] M. Alfè, B. Apicella, R. Barbella, J. N. Rouzaud, A. Tregrossi, and A. Ciajolo, "Structure-property relationship in nanostructures of young and mature soot in premixed flames," *Proceedings of the Combustion Institute*, vol. 32 I, no. 1, pp. 697–704, 2009.

[56] S. A. Skeen, H. A. Michelsen, K. R. Wilson, D. M. Popolan, A. Violi, and N. Hansen, "Near-threshold photoionization mass spectra of combustion-generated high-molecular-weight soot precursors," *Journal of Aerosol Science*, vol. 58, pp. 86–102, apr 2013.

[57] R. Puri, T. F. Richardson, R. J. Santoro, and R. A. Dobbins, "Aerosol dynamic processes of soot aggregates in a laminar ethene diffusion flame," *Combustion and Flame*, vol. 92, pp. 320–333, feb 1993.

[58] R. L. Vander Wal, V. M. Bryg, and C. H. Huang, "Aircraft engine particulate matter: Macro- micro- and nanostructure by HRTEM and chemistry by XPS," *Combustion and Flame*, vol. 161, pp. 602–611, feb 2014.

[59] P. Mitchell and M. Frenklach, "Particle aggregation with simultaneous surface growth," *Physical Review E - Statistical Physics, Plasmas, Fluids, and Related Interdisciplinary Topics*, vol. 67, p. 11, jun 2003.

[60] P. Mitchell and M. Frenklach, "Monte Carlo simulation of soot aggregation with simultaneous surface growth - Why primary particles appear spherical," *Symposium (International) on Combustion*, vol. 27, pp. 1507–1514, jan 1998.

[61] A. Kazakov and M. Frenklach, "On the relative contribution of acetylene and aromatics to soot particle surface growth," *Combustion and Flame*, vol. 112, pp. 270–274, jan 1998.

[62] J. A. Miller, S. J. Klippenstein, Y. Georgievskii, L. B. Harding, W. D. Allen, and A. C. Simmonett, "Reactions between Resonance-Stabilized Radicals: Propargyl + Allyl," *The Journal of Physical Chemistry A*, vol. 114, pp. 4881–4890, apr 2010.

[63] D. Wang, A. Violi, D. H. Kim, and J. A. Mullholland, "Formation of Naphthalene, Indene, and Benzene from Cyclopentadiene Pyrolysis: A DFT Study," *The Journal of Physical Chemistry A*, vol. 110, pp. 4719–4725, apr 2006.

[64] C. P. Fenimore, "Oxidation of soot by hydroxyl radicals," *Journal of Physical Chemistry*, vol. 71, no. 3, pp. 593–597, 1967.

[65] P. Roth, O. Brandt, and S. Von Gersum, "High temperature oxidation of suspended soot particles verified by CO and CO2 measurements," *Symposium (International) on Combustion*, vol. 23, pp. 1485–1491, jan 1991.

[66] C. A. Echavarria, I. C. Jaramillo, A. F. Sarofim, and J. S. Lighty, "Studies of soot oxidation and fragmentation in a two-stage burner under fuel-lean and fuel-rich conditions," *Proceedings of the Combustion Institute*, vol. 33, pp. 659–666, jan 2011.

[67] R. L. Vander Wal and A. J. Tomasek, "Soot oxidation: Dependence upon initial nanostructure," *Combustion and Flame*, vol. 134, pp. 1–9, jul 2003.

[68] B. R. Stanmore, J. F. Brilhac, and P. Gilot, "The oxidation of soot: A review of experiments, mechanisms and models," *Carbon*, vol. 39, pp. 2247–2268, dec 2001.

[69] K. G. Neoh, J. B. Howard, and A. F. Sarofim, "Effect of oxidation on the physical structure of soot," *Symposium (International) on Combustion*, vol. 20, no. 1, pp. 951–957, 1985.

[70] A. Garo, J. Lahaye, and G. Prado, "Mechanisms of formation and destruction of soot particles in a laminar methane-air diffusion flame," *Symposium (International) on Combustion*, vol. 21, pp. 1023–1031, jan 1988.

[71] C. M. Sorensen and G. D. Feke, "The Morphology of Macroscopic Soot," *Aerosol Science and Technology*, vol. 25, pp. 328–337, jan 1996.

[72] U. Koeylue, Y. Xing, and D. E. Rosner, "Fractal Morphology Analysis of Combustion-Generated Aggregates Using Angular Light Scattering and Electron Microscope Images," *Langmuir*, vol. 11, pp. 4848–4854, 1995.

[73] T. L. Barone, J. M. Storey, A. D. Youngquist, and J. P. Szybist, "An analysis of direct-injection spark-ignition (DISI) soot morphology," *Atmospheric Environment*, vol. 49, pp. 268–274, 2012.

[74] A. D. Abid, N. Heinz, E. D. Tolmachoff, D. J. Phares, C. S. Campbell, and H. Wang, "On evolution of particle size distribution functions of incipient soot in premixed ethylene-oxygen-argon flames," *Combustion and Flame*, vol. 154, no. 4, pp. 775–788, 2008.

[75] H. Lin, C. Gu, J. Camacho, B. Lin, C. Shao, R. Li, H. Gu, B. Guan, H. Wang, and Z. Huang, "Mobility size distributions of soot in premixed propene flames," *Combustion and Flame*, vol. 172, pp. 365–373, oct 2016.

[76] Ü. Ö. Köylü, G. M. Faeth, T. L. Farias, and M. G. Carvalho, "Fractal and projected structure properties of soot aggregates," *Combustion and Flame*, vol. 100, pp. 621–633, mar 1995.

[77] N. J. Kempema and M. B. Long, "Combined optical and TEM investigations for a detailed characterization of soot aggregate properties in a laminar coflow diffusion flame," *Combustion and Flame*, vol. 164, pp. 373–385, 2016.

[78] S. Schraml, S. Will, and A. Leipertz, "Simultaneous Measurement of Soot Mass Concentration and Primary Particle Size in the Exhaust of a DI Diesel Engine by Time-Resolved Laser-Induced Incandescence (TIRE-LII)," *SAE Technical Paper*, mar 1999.

[79] B. Hu and U. O. Koylu, "Size and morphology of soot particulates sampled from a turbulent nonpremixed acetylene flame," *Aerosol Science and Technology*, vol. 38, no. 10, pp. 1009–1018, 2004.

[80] E. Cenker, K. Kondo, G. Bruneaux, T. Dreier, T. Aizawa, and C. Schulz, "Assessment of soot particle-size imaging with LII at Diesel engine conditions," *Applied Physics B: Lasers and Optics*, vol. 119, pp. 765–776, jun 2015.

[81] M. Wentzel, H. Gorzawski, K.-H. Naumann, H. Saathoff, and S. Weinbruch, "Transmission electron microscopical and aerosol dynamical characterization of soot aerosols," *Journal of Aerosol Science*, vol. 34, pp. 1347–1370, oct 2003.

[82] R. L. Vander Wal, T. M. Ticich, and A. Brock Stephens, "Can soot primary particle size be determined using laser-induced incandescence?," *Combustion and Flame*, vol. 116, no. 1-2, pp. 291–296, 1999.

[83] Ü. Köylu, Y. Xing, and D. E. Rosner, "Fractal Morphology Analysis of Combustion-Generated Aggregates Using Angular Light Scattering and Electron Microscope Images," *Langmuir*, vol. 11, no. 12, pp. 4848–4854, 1995.

[84] B. Franzelli, M. Roussillo, P. Scouflaire, J. Bonnety, R. Jalain, T. Dormieux, S. Candel, and G. Legros, "Multi-diagnostic soot measurements in a laminar diffusion flame to assess the ISF database consistency," in *International Symposium on Combustion*, Elsevier, jun 2018.

[85] H. Bladh, J. Johnsson, and P. E. Bengtsson, "Influence of spatial laser energy distribution on evaluated soot particle sizes using two-colour laser-induced incandescence in a flat premixed ethylene/air flame," *Applied Physics B: Lasers and Optics*, vol. 96, no. 4, pp. 645–656, 2009.

[86] T. Lehre, B. Jungfleisch, R. Suntz, and H. Bockhorn, "Size distributions of nanoscaled particles and gas temperatures from time-resolved laser-induced-incandescence measurements," *Applied Optics*, vol. 42, no. 12, p. 2021, 2003.

[87] A. M. Vargas and Ö. L. Gülder, "Pressure dependence of primary soot particle size determined using thermophoretic sampling in laminar methane-air diffusion flames," *Proceedings of the Combustion Institute*, vol. 36, no. 1, pp. 975–984, 2017.

[88] H. Bladh, J. Johnsson, N. E. Olofsson, A. Bohlin, and P. E. Bengtsson, "Optical soot characterization using two-color laser-induced incandescence (2C-LII) in the soot growth region of a premixed flat flame," *Proceedings of the Combustion Institute*, vol. 33, pp. 641–648, jan 2011.

[89] E. Cenker, G. Bruneaux, T. Dreier, and C. Schulz, "Determination of small soot particles in the presence of large ones from time-resolved laser-induced incandescence," *Applied Physics B: Lasers and Optics*, vol. 118, pp. 169–183, feb 2015.

[90] F. Liu, H. Guo, G. J. Smallwood, and Ö. L. Gülder, "Effects of gas and soot radiation on soot formation in a coflow laminar ethylene diffusion flame," *Journal of Quantitative Spectroscopy and Radiative Transfer*, vol. 73, no. 2-5, pp. 409–421, 2002.

[91] M. E. Mueller, G. Blanquart, and H. Pitsch, "A joint volume-surface model of soot aggregation with the method of moments," *Proceedings of the Combustion Institute*, vol. 32 I, pp. 785–792, 2009.

[92] H. Oltmann, J. Reimann, and S. Will, "Wide-angle light scattering (WALS) for soot aggregate characterization," *Combustion and Flame*, vol. 157, pp. 516–522, mar 2010.

[93] C. Caumont-Prim, J. Ô. Yon, A. Coppalle, F. X. Ouf, and K. Fang Ren, "Measurement of aggregates' size distribution by angular light scattering," *Journal of Quantitative Spectroscopy and Radiative Transfer*, vol. 126, pp. 140–149, 2013.

[94] B. Ma and M. B. Long, "Combined soot optical characterization using 2-D multi-angle light scattering and spectrally resolved line-of-sight attenuation and its implication on soot color-ratio pyrometry," *Applied Physics B: Lasers and Optics*, vol. 117, pp. 287–303, oct 2014.

[95] H. Oltmann, J. Reimann, and S. Will, "Single-shot measurement of soot aggregate sizes by wide-angle light scattering (WALS)," *Applied Physics B: Lasers and Optics*, vol. 106, no. 1, pp. 171–183, 2012.

[96] E. Knutson and K. Whitby, "Aerosol classification by electric mobility: apparatus, theory, and applications," *Journal of Aerosol Science*, vol. 6, pp. 443–451, nov 1975.

[97] S. C. Wang and R. C. Flagan, "Scanning Electrical Mobility Spectrometer," *Aerosol Science and Technology*, vol. 13, pp. 230–240, jan 1990.

[98] B. Zhao, K. Uchikawa, and H. Wang, "A comparative study of nanoparticles in premixed flames by scanning mobility particle sizer, small angle neutron scattering, and transmission electron microscopy," *Proceedings of the Combustion Institute*, vol. 31 I, no. 1, pp. 851–860, 2007.

[99] J. Camacho, C. Liu, C. Gu, H. Lin, Z. Huang, Q. Tang, X. You, C. Saggese, Y. Li, H. Jung, L. Deng, I. Wlokas, and H. Wang, "Mobility size and mass of nascent soot particles in a benchmark premixed ethylene flame," *Combustion and Flame*, vol. 162, pp. 3810–3822, oct 2015.

[100] C. M. Sorensen, "The mobility of fractal aggregates: A review," *Aerosol Science and Technology*, vol. 45, no. 7, pp. 755–769, 2011.

[101] M. J. Hounslow, "A discretized population balance for continuous systems at steady state," *AIChE Journal*, vol. 36, pp. 106–116, 1990.

[102] J. D. Landgrebe and S. E. Pratsinis, "A discrete-sectional model for particulate production by gas-phase chemical reaction and aerosol coagulation in the free-molecular regime," *Journal of Colloid and Interface Science*, vol. 139, pp. 63–86, oct 1990.

[103] B. Zhao, Z. Yang, M. V. Johnston, H. Wang, A. S. Wexler, M. Balthasar, and M. Kraft, "Measurement and numerical simulation of soot particle size distribution functions in a laminar premixed ethylene-oxygen-argon flame," *Combustion and Flame*, vol. 133, pp. 173–188, 2003.

[104] H. Richter, S. Granata, W. H. Green, and J. B. Howard, "Detailed modeling of PAH and soot formation in a laminar premixed benzene/oxygen/argon low-pressure flame," *Proceedings of the Combustion Institute*, vol. 30, pp. 1397–1405, jan 2005.

[105] J. Z. Wen, M. J. Thomson, M. F. Lightstone, and S. N. Rogak, "Detailed Kinetic Modeling of Carbonaceous Nanoparticle Inception and Surface Growth during the Pyrolysis of C 6 H 6 behind Shock Waves," *Energy & Fuels*, vol. 20, pp. 547–559, 2006.

[106] M. Strumendo and H. Arastoopour, "Solution of PBE by MOM in finite size domains," *Chemical Engineering Science*, vol. 63, pp. 2624–2640, may 2008.

[107] M. Balthasar and M. Frenklach, "Monte-Carlo simulation of soot particle coagulation and aggregation: The effect of a realistic size distribution," *Proceedings of the Combustion Institute*, vol. 30, pp. 1467–1474, jan 2005.

[108] N. Morgan, M. Kraft, M. Balthasar, D. Wong, M. Frenklach, and P. Mitchell, "Numerical simulations of soot aggregation in premixed laminar flames," *Proceedings of the Combustion Institute*, vol. 31 I, pp. 693–700, jan 2007.

[109] J. Etheridge, S. Mosbach, M. Kraft, H. Wu, and N. Collings, "Modelling soot formation in a DISI engine," *Proceedings of the Combustion Institute*, vol. 33, pp. 3159–3167, jan 2011.

[110] M. Balthasar and M. Kraft, "A stochastic approach to calculate the particle size distribution function of soot particles in laminar premixed flames," *Combustion and Flame*, vol. 133, pp. 289–298, may 2003.

[111] M. E. Mueller, G. Blanquart, and H. Pitsch, "Hybrid Method of Moments for modeling soot formation and growth," *Combustion and Flame*, vol. 156, pp. 1143–1155, 2009.

[112] C. Yuan and R. O. Fox, "Conditional quadrature method of moments for kinetic equations," *Journal of Computational Physics*, vol. 230, no. 22, pp. 8216–8246, 2011.

[113] C. Yuan, F. Laurent, and R. O. Fox, "An extended quadrature method of moments for population balance equations," *Journal of Aerosol Science*, vol. 51, pp. 1–23, sep 2012.

[114] G. Blanquart and H. Pitsch, "Analyzing the effects of temperature on soot formation with a joint volume-surface-hydrogen model," *Combustion and Flame*, vol. 156, pp. 1614–1626, 2009.

[115] G. Blanquart and H. Pitsch, "A Joint Volume-Surface-Hydrogen Multi-variate Model for Soot Formation," *Combustion Generated Fine Carbonaceous Particles*, pp. 1–4, 2009.

[116] S. Salenbauch, A. Cuoci, A. Frassoldati, C. Saggese, T. Faravelli, and C. Hasse, "Modeling soot formation in premixed flames using an Extended Conditional Quadrature Method of Moments," *Combustion and Flame*, vol. 162, pp. 2529–2543, jun 2015.

[117] S. Salenbauch, M. Sirignano, D. L. Marchisio, M. Pollack, A. D'Anna, and C. Hasse, "Detailed particle nucleation modeling in a sooting ethylene flame using a Conditional Quadrature Method of Moments (CQMOM)," *Proceedings of the Combustion Institute*, vol. 36, pp. 771–779, jan 2017.

[118] D. L. Marchisio and A. A. Barresi, "Investigation of soot formation in turbulent flames with a pseudo-bivariate population balance model," *Chemical Engineering Science*, vol. 64, no. 2, pp. 294–303, 2009.

[119] M. L. Botero, N. Eaves, J. A. Dreyer, Y. Sheng, J. Akroyd, W. Yang, and M. Kraft, "Experimental and numerical study of the evolution of soot primary particles in a diffusion flame," *Proceedings of the Combustion Institute*, vol. 37, pp. 2047–2055, jan 2019.

[120] M. Hofmann, B. F. Kock, and C. Schulz, "A web-based interface for modeling laser-induced incandescence (LIISim)," *CEUR Workshop Proceedings*, vol. 211, p. 26, 2006.

[121] F. Liu, G. J. Smallwood, and D. R. Snelling, "Effects of primary particle diameter and aggregate size distribution on the temperature of soot particles heated by pulsed lasers," *Journal of Quantitative Spectroscopy and Radiative Transfer*, vol. 93, no. 1-3 SPEC. ISS., pp. 301–312, 2005.

[122] F. Liu, M. Yang, F. A. Hill, G. J. Smallwood, and D. R. Snelling, "Influence of polydisperse distributions of both primary particle and aggregate sizes on soot temperature in low-fluence laser-induced incandescence," *Applied Physics B*, vol. 83, pp. 383–395, jun 2006.

[123] "International Sooting Flame (ISF) Workshop," http://www.adelaide.edu.au/cet/isfworkshop/, Updated in 2016.

[124] C. Saggese, N. E. Sánchez, A. Frassoldati, A. Cuoci, T. Faravelli, M. U. Alzueta, and E. Ranzi, "Kinetic Modeling Study of Polycyclic Aromatic Hydrocarbons and Soot Formation in Acetylene Pyrolysis," *Energy & Fuels*, vol. 28, pp. 1489–1501, feb 2014.

[125] D. L. Marchisio and R. O. Fox, "Solution of population balance equations using the direct quadrature method of moments," *Journal of Aerosol Science*, vol. 36, pp. 43–73, jan 2005.

[126] D. L. Marchisio and R. O. Fox, *Computational Models for Polydisperse Particulate and Multiphase Systems (Cambridge Series in Chemical Engineering)*. 2013.

[127] M. Frenklach and S. J. Harris, "Aerosol dynamics modeling using the method of moments," *Journal of Colloid And Interface Science*, vol. 118, no. 1, pp. 252–261, 1987.

[128] M. Frenklach, "On surface growth mechanism of soot particles," *Symposium (International) on Combustion*, vol. 26, pp. 2285–2293, jan 1996.

[129] M. Frenklach and H. Wang, "Detailed modeling of soot particle nucleation and growth," *Symposium (International) on Combustion*, vol. 23, pp. 1559–1566, jan 1991.

[130] A. Kazakov and M. Frenklach, "Dynamic modeling of soot particle coagulation and aggregation: Implementation with the method of moments and application to high-pressure laminar premixed flames," *Combustion and Flame*, vol. 114, pp. 484–501, aug 1998.

[131] M. Balthasar and M. Frenklach, "Detailed kinetic modeling of soot aggregate formation in laminar premixed flames," *Combustion and Flame*, vol. 140, pp. 130–145, jan 2005.

[132] N. J. Brown, K. L. Revzan, and M. Frenklach, "Detailed kinetic modeling of soot formation in ethylene/air mixtures reacting in a perfectly stirred reactor," *Symposium (International) on Combustion*, vol. 27, pp. 1573–1580, jan 1998.

[133] D. L. Marchisio, J. T. Pikturna, R. O. Fox, R. D. Vigil, and A. A. Barresi, "Quadrature method of moments for population-balance equations," *AIChE Journal*, vol. 49, pp. 1266–1276, may 2003.

[134] E. Madadi-Kandjani and A. Passalacqua, "An extended quadrature-based moment method with log-normal kernel density functions," *Chemical Engineering Science*, vol. 131, pp. 323–339, 2015.

[135] S. P. Roy, P. G. Arias, V. R. Lecoustre, D. C. Haworth, H. G. Im, and A. Trouvé, "Development of High Fidelity Soot Aerosol Dynamics Models using Method of Moments with Interpolative Closure," *Aerosol Science and Technology*, vol. 48, pp. 379–391, apr 2014.

[136] M. E. Mueller, G. Blanquart, and H. Pitsch, "Modeling the oxidation-induced fragmentation of soot aggregates in laminar flames," *Proceedings of the Combustion Institute*, vol. 33, no. 1, pp. 667–674, 2011.

[137] S. Adhikari, A. Sayre, and A. J. Chandy, "A Hybrid Newton/Time Integration Approach Coupled to Soot Moment Methods for Modeling Soot Formation and Growth in Perfectly-Stirred Reactors," *Combustion Science and Technology*, vol. 188, no. 8, pp. 1262–1282, 2016.

[138] S. Deng, M. E. Mueller, Q. N. Chan, N. H. Qamar, B. B. Dally, Z. T. Alwahabi, and G. J. Nathan, "Hydrodynamic and chemical effects of hydrogen addition on soot evolution in turbulent nonpremixed bluff body ethylene flames," *Proceedings of the Combustion Institute*, vol. 36, pp. 807–814, jan 2017.

[139] S. T. Chong, V. Raman, M. E. Mueller, and H. G. Im, "The Role of Recirculation Zones in Soot Formation in Aircraft Combustors," in *Volume 4B: Combustion, Fuels, and Emissions*, p. V04BT04A008, ASME, jun 2018.

[140] A. Wick, F. Priesack, and H. Pitsch, "Large-Eddy simulation and detailed modeling of soot evolution in a model aero engine combustor," *Proceedings of the ASME Turbo Expo*, vol. 4A-2017, pp. 1–10, 2017.

[141] S. J. Harris and I. M. Kennedy, "The Coagulation of Soot Particles with van der Waals Forces," *Combustion Science and Technology*, vol. 59, pp. 443–454, jun 1988.

[142] S. J. Harris and A. M. Weiner, "A picture of soot particle inception," *Symposium (International) on Combustion*, vol. 22, pp. 333–342, jan 1989.

[143] S. H. Park and S. N. Rogak, "A novel fixed-sectional model for the formation and growth of aerosol agglomerates," *Journal of Aerosol Science*, vol. 35, pp. 1385–1404, nov 2004.

[144] M. D. Smooke, M. B. Long, B. C. Connelly, M. B. Colket, and R. J. Hall, "Soot formation in laminar diffusion flames," *Combustion and Flame*, vol. 143, no. 4, pp. 613–628, 2005.

[145] S. B. Dworkin, J. A. Cooke, B. A. Bennett, B. C. Connelly, M. B. Long, M. D. Smooke, R. J. Hall, and M. B. Colket, "Distributed-memory parallel computation of a forced, time-dependent, sooting, ethylene/air coflow diffusion flame," *Combustion Theory and Modelling*, vol. 13, pp. 795–822, dec 2009.

[146] S. Kumar and D. Ramkrishna, "On the solution of population balance equations by discretizationI. A fixed pivot technique," *Chemical Engineering Science*, vol. 51, pp. 1311–1332, 1996.

[147] Y. P. Kim and J. H. Seinfeld, "Simulation of multicomponent aerosol condensation by the moving sectional method," *Journal of Colloid And Interface Science*, vol. 135, pp. 185–199, mar 1990.

[148] S. H. Park, S. N. Rogak, W. K. Bushe, J. Z. Wen, and M. J. Thomson, "An aerosol model to predict size and structure of soot particles," *Combustion Theory and Modelling*, vol. 9, no. 3, pp. 499–513, 2005.

[149] R. I. Patterson and M. Kraft, "Models for the aggregate structure of soot particles," *Combustion and Flame*, vol. 151, pp. 160–172, oct 2007.

[150] Q. Zhang, H. Guo, F. Liu, G. J. Smallwood, and M. J. Thomson, "Implementation of an advanced fixed sectional aerosol dynamics model with soot aggregate formation in a laminar methane/air coflow diffusion flame," *Combustion Theory and Modelling*, vol. 12, pp. 621–641, jul 2008.

[151] K. Nakaso, T. Fujimoto, T. Seto, M. Shimada, K. Okuyama, and M. M. Lunden, "Size distribution change of titania nano-particle agglomerates generated by gas phase reaction, agglomeration, and sintering," *Aerosol Science and Technology*, vol. 35, pp. 929–947, 2001.

[152] P. Rodrigues, B. Franzelli, R. Vicquelin, O. Gicquel, and N. Darabiha, "Coupling an LES approach and a soot sectional model for the study of sooting turbulent non-premixed flames," *Combustion and Flame*, vol. 190, pp. 477–499, apr 2018.

[153] C. J. Pope and J. B. Howard, "Simultaneous Particle and Molecule Modeling (SPAMM): An Approach for Combining Sectional Aerosol Equations and Elementary Gas-Phase Reactions," *Aerosol Science and Technology*, vol. 27, pp. 73–94, jan 1997.

[154] T. Blacha, M. Di Domenico, P. Gerlinger, and M. Aigner, "Soot predictions in premixed and non-premixed laminar flames using a sectional approach for PAHs and soot," *Combustion and Flame*, vol. 159, no. 1, pp. 181–193, 2012.

[155] A. D'Anna and M. Sirignano, "An Advanced Multi-Sectional Method for Particulate Matter Modeling in Flames," *Green Energy and Technology*, pp. 363–388, 2013.

[156] M. Sirignano, J. Kent, and A. D'Anna, "Further experimental and modelling evidences of soot fragmentation in flames," *Proceedings of the Combustion Institute*, vol. 35, pp. 1779–1786, jan 2015.

[157] C. S. McEnally, A. M. Schaffer, M. B. Long, L. D. Pfefferle, M. D. Smooke, M. B. Colket, and R. J. Hall, "Computational and Experimental Study of Soot Formation in a Coflow, Laminar Diffusion Flame," in *Twenty-Seventh Symposium (International) on Combustion/The Combustion Institute*, vol. 117, pp. 1459–1505, 1998.

[158] M. D. Smooke, C. S. McEnally, L. D. Pfefferle, R. J. Hall, and M. B. Colket, "Computational and Experimental Study of Soot Formation in a Coflow, Laminar Diffusion Flame," *Combustion and Flame*, vol. 117, pp. 117–139, apr 1999.

[159] M. D. Smooke, R. J. Hall, M. B. Colket, J. Fielding, M. B. Long, C. S. McEnally, and L. D. Pfefferle, "Investigation of the transition from lightly sooting towards heavily sooting co-flow ethylene diffusion flames," *Combustion Theory and Modelling*, vol. 8, no. 3, pp. 593–606, 2004.

[160] S. B. Dworkin, M. D. Smooke, and V. Giovangigli, "The impact of detailed multicomponent transport and thermal diffusion effects on soot formation in ethylene/air flames," *Proceedings of the Combustion Institute*, vol. 32 I, pp. 1165–1172, jan 2009.

[161] B. C. Connelly, M. B. Long, M. D. Smooke, R. J. Hall, and M. B. Colket, "Computational and experimental investigation of the interaction of soot and NO in coflow diffusion flames," *Proceedings of the Combustion Institute*, vol. 32 I, no. 1, pp. 777–784, 2009.

[162] S. B. Dworkin, Q. Zhang, M. J. Thomson, N. A. Slavinskaya, and U. Riedel, "Application of an enhanced PAH growth model to soot formation in a laminar coflow ethylene/air diffusion flame," *Combustion and Flame*, vol. 158, no. 9, pp. 1682–1695, 2011.

[163] R. J. Santoro, T. T. Yeh, J. J. Horvath, and H. G. Semerjian, "The Transport and Growth of Soot Particles in Laminar Diffusion Flames," *Combustion Science and Technology*, vol. 53, pp. 89–115, jun 1987.

[164] Q. Zhang, M. J. Thomson, H. Guo, F. Liu, and G. J. Smallwood, "A numerical study of soot aggregate formation in a laminar coflow diffusion flame," *Combustion and Flame*, vol. 156, no. 3, pp. 697–705, 2009.

[165] Q. Zhang, H. Guo, F. Liu, G. J. Smallwood, and M. J. Thomson, "Modeling of soot aggregate formation and size distribution in a laminar ethylene/air coflow diffusion flame with detailed PAH chemistry and an advanced sectional aerosol dynamics model," *Proceedings of the Combustion Institute*, vol. 32 I, pp. 761–768, jan 2009.

[166] J. D. Herdman, B. C. Connelly, M. D. Smooke, M. B. Long, and J. H. Miller, "A comparison of Raman signatures and laser-induced incandescence with direct numerical simulation of soot growth in non-premixed ethylene/air flames," *Carbon*, vol. 49, no. 15, pp. 5298–5311, 2011.

[167] A. Khosousi and S. B. Dworkin, "Detailed modelling of soot oxidation by O2 and OH in laminar diffusion flames," *Proceedings of the Combustion Institute*, vol. 35, pp. 1903–1910, jan 2015.

[168] R. Santoro, H. Semerjian, and R. Dobbins, "Soot particle measurements in diffusion flames," *Combustion and Flame*, vol. 51, pp. 203–218, jan 1983.

[169] A. Veshkini, S. B. Dworkin, and M. J. Thomson, "A soot particle surface reactivity model applied to a wide range of laminar ethylene/air flames," *Combustion and Flame*, vol. 161, pp. 3191–3200, dec 2015.

[170] C. R. Shaddix and K. C. Smyth, "Laser-induced incandescence measurements of soot production in steady and flickering methane, propane, and ethylene diffusion flames," *Combustion and Flame*, vol. 107, pp. 418–452, dec 1996.

[171] A. Violi and A. Venkatnathan, "Combustion-generated nanoparticles produced in a benzene flame: A multiscale approach," *Journal of Chemical Physics*, vol. 125, no. 5, 2006.

[172] M. Celnik, R. Patterson, M. Kraft, and W. Wagner, "Coupling a stochastic soot population balance to gas-phase chemistry using operator splitting," *Combustion and Flame*, vol. 148, no. 3, pp. 158–176, 2007.

[173] A. L. Bodor, B. Franzelli, T. Faravelli, and A. Cuoci, "A post processing technique to predict primary particle size of sooting flames based on a chemical discrete sectional model : application to diluted coflow flames," *Submitted to Combustion and Flame*, pp. 1–45, 2019.

[174] A. Cuoci, A. Frassoldati, T. Faravelli, and E. Ranzi, "Numerical modeling of laminar flames with detailed kinetics based on the operator-splitting method," *Energy and Fuels*, vol. 27, no. 12, pp. 7730–7753, 2013.

[175] S. K. Friedlander and W. H. Marlow, "Smoke, Dust and Haze: Fundamentals of Aerosol Behavior," *Physics Today*, vol. 30, pp. 58–59, sep 1977.

[176] F. Bisetti, G. Blanquart, M. E. Mueller, and H. Pitsch, "On the formation and early evolution of soot in turbulent nonpremixed flames," *Combustion and Flame*, vol. 159, pp. 317–335, jan 2012.

[177] A. Cuoci, A. Frassoldati, T. Faravelli, and E. Ranzi, "OpenSMOKE++: An object-oriented framework for the numerical modeling of reactive systems with detailed kinetic mechanisms," *Computer Physics Communications*, vol. 192, pp. 237–264, jul 2015.

[178] S. De Iuliis, S. Maffi, F. Cignoli, and G. Zizak, "Three-angle scattering/extinction versus TEM measurements on soot in premixed ethylene/air flame," *Applied Physics B: Lasers and Optics*, vol. 102, pp. 891–903, 2011.

[179] S. De Iuliis, S. Maffi, F. Migliorini, F. Cignoli, and G. Zizak, "Effect of hydrogen addition on soot formation in an ethylene/air premixed flame," in *Applied Physics B: Lasers and Optics*, vol. 106, pp. 707–715, 2012.

[180] B. W. Ward, J. A. Notte, and N. P. Economou, "Helium ion microscope: A new tool for nanoscale microscopy and metrology," *Journal of Vacuum Science & Technology B: Microelectronics and Nanometer Structures*, vol. 24, p. 2871, nov 2006.

[181] M. Schenk, S. Lieb, H. Vieker, A. Beyer, A. Gölzhäuser, H. Wang, and K. Kohse-Höinghaus, "Imaging Nanocarbon Materials: Soot Particles in Flames are Not Structurally Homogeneous," *ChemPhysChem*, vol. 14, pp. 3248–3254, oct 2013.

[182] B. Kock, T. Eckhardt, and P. Roth, "In-cylinder sizing of diesel particles by time-resolved laser-induced incandescence (TR-LII)," *Proceedings of the Combustion Institute*, vol. 29, no. 2, pp. 2775–2782, 2002.

[183] B. Axelsson, R. Collin, and P.-E. Bengtsson, "Laser-induced incandescence for soot particle size measurements in premixed flat flames," *Applied Optics*, vol. 39, p. 3683, jul 2000.

[184] H. A. Michelsen, "Understanding and predicting the temporal response of laser-induced incandescence from carbonaceous particles," *Journal of Chemical Physics*, vol. 118, no. 15, pp. 7012–7045, 2003.

[185] K. J. Daun, B. J. Stagg, F. Liu, G. J. Smallwood, and D. R. Snelling, "Determining aerosol particle size distributions using time-resolved laser-induced incandescence," *Applied Physics B: Lasers and Optics*, vol. 87, no. 2, pp. 363–372, 2007.

[186] C. Betrancourt, F. Liu, P. Desgroux, X. Mercier, A. Faccinetto, M. Salamanca, L. Ruwe, K. Kohse-Höinghaus, D. Emmrich, A. Beyer, A. Gölzhäuser, and T. Tritscher, "Investigation of the size of the incandescent incipient soot particles in premixed sooting and nucleation flames of n-butane using LII, HIM, and 1 nm-SMPS," *Aerosol Science and Technology*, vol. 51, no. 8, pp. 916–935, 2017.

[187] S. Dankers and A. Leipertz, "Determination of primary particle size distributions from time-resolved laser-induced incandescence measurements," *Applied Optics*, vol. 43, no. 18, pp. 3726–3731, 2004.

[188] K. K. Foo, Z. Sun, P. R. Medwell, Z. T. Alwahabi, B. B. Dally, and G. J. Nathan, "Experimental investigation of acoustic forcing on temperature, soot volume fraction and primary particle diameter in non-premixed laminar flames," *Combustion and Flame*, vol. 181, pp. 270–282, 2017.

[189] H. Bockhorn, A. D'Anna, A. F. Sarofim, and H. Wang, "Combustion generated fine carbonaceous particles, year = 2007," *Proceedings of an International Workshop held in VIlla Orlandi, Anacapri*, no. January, p. 538.

[190] P. Desgroux, X. Mercier, and K. A. Thomson, "Study of the formation of soot and its precursors in flames using optical diagnostics," *Proceedings of the Combustion Institute*, vol. 34, pp. 1713–1738, jan 2013.

[191] M. Sirignano, D. Bartos, M. Conturso, M. Dunn, A. D'Anna, and A. R. Masri, "Detection of nanostructures and soot in laminar premixed flames," *Combustion and Flame*, vol. 176, pp. 299–308, 2017.

[192] H. Bladh, N. E. Olofsson, T. Mouton, J. Simonsson, X. Mercier, A. Faccinetto, P. E. Bengtsson, and P. Desgroux, "Probing the smallest soot particles in low-sooting premixed flames using laser-induced incandescence," *Proceedings of the Combustion Institute*, vol. 35, pp. 1843–1850, jan 2015.

[193] G. Cléon, T. Amodeo, A. Faccinetto, and P. Desgroux, "Laser induced incandescence determination of the ratio of the soot absorption functions at 532 nm and 1064 nm in the nucleation zone of a low pressure premixed sooting flame," *Applied Physics B: Lasers and Optics*, vol. 104, no. 2, pp. 297–305, 2011.

[194] A. D'Anna, M. Commodo, M. Sirignano, P. Minutolo, and R. Pagliara, "Particle formation in opposed-flow diffusion flames of ethylene: An experimental and numerical study," *Proceedings of the Combustion Institute*, vol. 32 I, pp. 793–801, jan 2009.

[195] M. Sirignano, A. Collina, M. Commodo, P. Minutolo, and A. D'Anna, "Detection of aromatic hydrocarbons and incipient particles in an opposed-flow flame of ethylene by spectral and time-resolved laser induced emission spectroscopy," *Combustion and Flame*, vol. 159, pp. 1663–1669, apr 2012.

[196] A. L. Bodor, A. Cuoci, and T. Faravelli, "Towards a more consistent validation of numerical modeling of primary particle diameters in sooting flames," *Submitted to Applied Physcs B*.

[197] R. Boyce, J. W. Morton, A. F. P. Houwing, C. Mundt, and D. J. Bone, "Computational fluid dynamics validation using multiple interferometric views of a hypersonic flowfield," *Journal of Spacecraft and Rockets*, vol. 33, pp. 319–325, may 1996.

[198] P. M. Danehy, P. C. Palma, R. R. Boyce, and A. F. P. Houwing, "Numerical Simulation of Laser-Induced Fluorescence Imaging in Shock-Layer Flows," *AIAA JOURNAL*, vol. 37, no. 6, 1999.

[199] B. C. Connelly, B. A. Bennett, M. D. Smooke, and M. B. Long, "A paradigm shift in the interaction of experiments and computations in combustion research," *Proceedings of the Combustion Institute*, vol. 32 I, pp. 879–886, 2009.

[200] D. R. Snelling, F. Liu, G. J. Smallwood, and Ö. L. Gülder, "Determination of the soot absorption function and thermal accommodation coefficient using low-fluence LII in a laminar coflow ethylene diffusion flame," *Combustion and Flame*, vol. 136, pp. 180–190, jan 2004.

[201] R. W. Weeks and W. W. Duley, "Aerosol-particle sizes from light emission during excitation by TEA CO2laser pulses," *Journal of Applied Physics*, vol. 45, no. 10, pp. 4661–4662, 1974.

[202] H. Bladh, J. Johnsson, and P. E. Bengtsson, "On the dependence of the laser-induced incandescence (LII) signal on soot volume fraction for variations in particle size," *Applied Physics B: Lasers and Optics*, vol. 90, pp. 109–125, jan 2008.

[203] B. J. McCoy and C. Y. Cha, "Transport phenomena in the rarefied gas transition regime," *Chemical Engineering Science*, vol. 29, no. 2, pp. 381–388, 1974.

[204] L. A. Melton, "Soot diagnostics based on laser heating," *Applied Optics*, vol. 23, p. 2201, jul 1984.

[205] H. Michelsen, C. Schulz, G. Smallwood, and S. Will, "Laser-induced incandescence: Particulate diagnostics for combustion, atmospheric, and industrial applications," *Progress in Energy and Combustion Science*, vol. 51, pp. 2–48, dec 2015.

[206] N. A. Fuchs, "On the stationary charge distribution on aerosol particles in a bipolar ionic atmosphere," *Geofisica Pura e Applicata*, vol. 56, pp. 185–193, sep 1963.

[207] M. Kerker, *The Scattering of Light and Other Electromagnetic Radiation*. 1 ed., 1969.

[208] A. V. Filippov and D. E. Rosner, "Energy transfer between an aerosol particle and gas at high temperature ratios in the Knudsen transition regime," *International Journal of Heat and Mass Transfer*, vol. 43, pp. 127–138, jan 2000.

[209] P. G. Wright, "On the discontinuity involved in diffusion across an interface (the delta of Fucks)," *Discussions of the Faraday Society*, vol. 30, pp. 100–112, 1960.

[210] M. I. Cotterell, B. J. Mason, A. E. Carruthers, J. S. Walker, A. J. Orr-Ewing, and J. P. Reid, *Measurements of the evaporation and hygroscopic response of single fine-mode aerosol particles using a Bessel beam optical trap*, vol. 16. Cambridge University Press, 2014.

[211] R. J. Kee, F. M. Rupley, E. Meeks, and J. A. Miller, "CHEMKIN-III: A Fortran Chemical Kinetics Package for the Analysis of Gas Phase Chemical and Plasma Kinetics," Sandia National Laboratories Report," 1996.

[212] H. A. Michelsen, F. Liu, B. F. Kock, H. Bladh, A. Boiarciuc, M. Charwath, T. Dreier, R. Hadef, M. Hofmann, J. Reimann, S. Will, P. E. Bengtsson, H. Bockhorn, F. Foucher, K. P. Geigle, C. Mounaïm-Rousselle, C. Schulz, R. Stirn, B. Tribalet, and R. Suntz, "Modeling laser-induced incandescence of soot: A summary and comparison of LII models," *Applied Physics B: Lasers and Optics*, vol. 87, pp. 503–521, may 2007.

[213] D. L. Hofeldt, "Real-Time Soot Concentration Measurement Technique for Engine Exhaust Streams," *SAE Technical Paper Series*, pp. 33–45, mar 1993.

[214] H. R. Leider, O. H. Krikorian, and D. A. Young, "Thermodynamic properties of carbon up to the critical point," *Carbon*, vol. 11, pp. 555–563, oct 1973.

[215] G. J. Smallwood, D. R. Snelling, F. Liu, and O. L. Gulder, "Clouds over soot evaporation: Errors in modeling laser-induced incandescence of soot," *J Heat Trans-T Asme*, vol. 123, pp. 814–818, aug 2001.

[216] L. Chen, J. Wu, M. Yan, X. Wu, G. Gréhan, and K. Cen, "Determination of soot particle size using time-gated laser-induced incandescence images," *Applied Physics B: Lasers and Optics*, vol. 123, p. 96, apr 2017.

[217] C. Schulz, B. Kock, M. Hofmann, H. Michelsen, S. Will, B. Bougie, R. Suntz, and G. Smallwood, "Laser-induced incandescence: recent trends and current questions," *Applied Physics B*, vol. 83, pp. 333–354, jun 2006.

[218] S. Bejaoui, R. Lemaire, P. Desgroux, and E. Therssen, "Experimental study of the E(m, λ)/E(m, 1064) ratio as a function of wavelength, fuel type, height above the burner and temperature," *Applied Physics B: Lasers and Optics*, vol. 116, no. 2, pp. 313–323, 2014.

[219] F. Migliorini, K. A. Thomson, and G. J. Smallwood, "Investigation of optical properties of aging soot," in *Applied Physics B: Lasers and Optics*, vol. 104, pp. 273–283, Springer-Verlag, aug 2011.

[220] S. S. Krishnan, K.-C. Lin, and G. M. Faeth, "Extinction and Scattering Properties of Soot Emitted From Buoyant Turbulent Diffusion Flames," *Journal of Heat Transfer*, vol. 123, no. 2, p. 331, 2001.

[221] D. R. Snelling, K. A. Thomson, G. J. Smallwood, Oslash, . L. G-uacute, Lder, E. J. Weckman, and R. A. Fraser, "Spectrally Resolved Measurement of Flame Radiation to Determine Soot Temperature and Concentration," *AIAA Journal*, vol. 40, pp. 1789–1795, sep 2002.

[222] D. R. Snelling, K. A. Thomson, F. Liu, and G. J. Smallwood, "Comparison of LII derived soot temperature measurements with LII model predictions for soot in a laminar diffusion flame," *Applied Physics B: Lasers and Optics*, vol. 96, pp. 657–669, sep 2009.

[223] B. F. Kock, B. Tribalet, C. Schulz, and P. Roth, "Two-color time-resolved LII applied to soot particle sizing in the cylinder of a Diesel engine," *Combustion and Flame*, vol. 147, pp. 79–92, oct 2006.

[224] J. Reimann, S. A. Kuhlmann, and S. Will, "2D aggregate sizing by combining laser-induced incandescence (LII) and elastic light scattering (ELS)," *Applied Physics B: Lasers and Optics*, vol. 96, pp. 583–592, sep 2009.

[225] T. Charalampopoulos and J. Felske, "Refractive indices of soot particles deduced from in-situ laser light scattering measurements," *Combustion and Flame*, vol. 68, pp. 283–294, jun 1987.

[226] D. C. E. E. A. S. T.L. Henriksen, T.A. Ring, "5th U.S. Combustion Meeting, March 25-28th," *AIAA Journal*, 2007.

[227] T. T. Charalampopoulos, "An automated light scattering system and a method for the i n s i t u measurement of the index of refraction of soot particles," *Review of Scientific Instruments*, vol. 58, pp. 1638–1646, sep 1987.

[228] A. D'Alessio, A. D'Anna, A. D'Orsi, P. Minutolo, R. Barbella, and A. Ciajolo, "Precursor formation and soot inception in premixed ethylene flames," *Symposium (International) on Combustion*, vol. 24, pp. 973–980, jan 1992.

[229] A. Borghese and S. S. Merola, "Detection of extremely fine carbonaceous particles in the exhausts of diesel and spark-ignited internal combustion engines, by means of broad-band extinction and scattering spectroscopy in the ultraviolet band 190-400 NM," *Symposium (International) on Combustion*, vol. 27, pp. 2101–2109, jan 1998.

[230] P. Minutolo, G. Gambi, A. D'Alessio, and S. Carlucci, "Spectroscopic characterisation of carbonaceous nanoparticles in premixed flames," *Atmospheric Environment*, vol. 33, pp. 2725–2732, aug 1999.

[231] G. W. Mulholland and R. D. Mountain, "Coupled dipole calculation of extinction coefficient and polarization ratio for smoke agglomerates," *Combustion and Flame*, vol. 119, pp. 56–68, oct 1999.

[232] D. Cecere, L. A. Sgro, G. Basile, A. D'Alessio, A. D'Anna, and P. Minutolo, "Evidence and characterization of nanoparticles produced in nonsooting premixed flames," *Combustion Science and Technology*, vol. 174, pp. 377–398, nov 2002.

[233] H. Chang and T. T. Charalampopoulos, "Determination of the Wavelength Dependence of Refractive Indices of Flame Soot," *Proceedings of the Royal Society A: Mathematical, Physical and Engineering Sciences*, vol. 430, pp. 577–591, sep 1990.

[234] Z. W. Sun, D. H. Gu, G. J. Nathan, Z. T. Alwahabi, and B. B. Dally, "Single-shot, Time-Resolved planar Laser-Induced Incandescence (TiRe-LII) for soot primary particle sizing in flames," *Proceedings of the Combustion Institute*, vol. 35, pp. 3673–3680, jan 2015.

[235] S. Will, S. Schraml, K. Bader, and A. Leipertz, "Performance characteristics of soot primary particle size measurements by time-resolved laser-induced incandescence," *Applied Optics*, vol. 37, no. 24, p. 5647, 1998.

[236] F. Liu, K. A. Thomson, and G. J. Smallwood, "Soot temperature and volume fraction retrieval from spectrally resolved flame emission measurement in laminar axisymmetric coflow diffusion flames: Effect of self-absorption," *Combustion and Flame*, vol. 160, pp. 1693–1705, sep 2013.

[237] F. Cignoli, S. De Iuliis, V. Manta, and G. Zizak, "Two-dimensional two-wavelength emission technique for soot diagnostics," *Applied Optics*, vol. 40, p. 5370, oct 2001.

[238] B. Ma and M. B. Long, "Absolute light calibration using S-type thermocouples," *Proceedings of the Combustion Institute*, vol. 34, pp. 3531–3539, jan 2013.

[239] H. Guo, J. A. Castillo, and P. B. Sunderland, "Digital camera measurements of soot temperature and soot volume fraction in axisymmetric flames," *Applied Optics*, vol. 52, p. 8040, nov 2013.

[240] S. Di Stasio and P. Massoli, "Influence of the soot property uncertainties in temperature and volume-fraction measurements by two-colour pyrometry," *Measurement Science and Technology*, vol. 5, pp. 1453–1465, dec 1994.

[241] P. B. Kuhn, B. Ma, B. C. Connelly, M. D. Smooke, and M. B. Long, "Soot and thin-filament pyrometry using a color digital camera," *Proceedings of the Combustion Institute*, vol. 33, no. 1, pp. 743–750, 2011.

[242] T. P. Jenkins and R. K. Hanson, "Soot pyrometry using modulated absorption/emission," *Combustion and Flame*, vol. 126, pp. 1669–1679, aug 2001.

[243] J. Wu, L. Chen, J. Zhou, X. Wu, X. Gao, G. Gréhan, and K. Cen, "Particle size distribution of soot from a laminar/diffusion flame," *Aerosol and Air Quality Research*, vol. 17, no. 8, pp. 2095–2109, 2017.

[244] R. Stirn, T. G. Baquet, S. Kanjarkar, W. Meier, K. P. Geigle, H. H. Grotheer, C. Wahl, and M. Aigner, "Comparison of particle size measurements with laser-induced incandescence, mass spectroscopy, and scanning mobility particle sizing in a laminar premixed ethylene-air flame," *Combustion Science and Technology*, vol. 181, no. 2, pp. 329–349, 2009.

[245] X. López-Yglesias, P. E. Schrader, and H. A. Michelsen, "Soot maturity and absorption cross sections," *Journal of Aerosol Science*, vol. 75, pp. 43–64, sep 2014.

[246] X. Sha, B. Jackson, D. Lemoine, and B. Lepetit, "Quantum studies of H atom trapping on a graphite surface," *Journal of Chemical Physics*, vol. 122, no. 1, 2005.

[247] C. T. Rettner, D. J. Auerbach, J. C. Tully, and A. W. Kleyn, "Chemical dynamics at the gas-surface interface," *Journal of Physical Chemistry*, vol. 100, no. 31, pp. 13021–13033, 1996.

[248] K. Daun, "Thermal accommodation coefficients between polyatomic gas molecules and soot in laser-induced incandescence experiments," *International Journal of Heat and Mass Transfer*, vol. 52, pp. 5081–5089, oct 2009.

[249] A. Güttler, T. Zecho, and J. Küppers, "A LEED and STM study of H(D) adsorption on C(0001) surfaces," *Chemical Physics Letters*, vol. 395, no. 1-3, pp. 171–176, 2004.

[250] T. Zecho, A. Güttler, X. Sha, B. Jackson, and J. Küppers, "Adsorption of hydrogen and deuterium atoms on the (0001) graphite surface," *Journal of Chemical Physics*, vol. 117, no. 18, pp. 8486–8492, 2002.

[251] B. Zhao, Z. Yang, Z. Li, M. V. Johnston, and H. Wang, "Particle size distribution function of incipient soot in laminar premixed ethylene flames: Effect of flame temperature," *Proceedings of the Combustion Institute*, vol. 30, no. 1, pp. 1441–1448, 2005.

[252] F. Migliorini, S. De Iuliis, F. Cignoli, and G. Zizak, "How "flat" is the rich premixed flame produced by your McKenna burner?," *Combustion and Flame*, vol. 153, pp. 384–393, may 2008.

[253] Y. Xuan and G. Blanquart, "Two-dimensional flow effects on soot formation in laminar premixed flames," *Combustion and Flame*, vol. 166, pp. 113–124, 2016.

[254] A. D'Anna, M. Sirignano, and J. Kent, "A model of particle nucleation in premixed ethylene flames," *Combustion and Flame*, vol. 157, pp. 2106–2115, nov 2010.

[255] R. Hadef, K. P. Geigle, W. Meier, and M. Aigner, "Soot characterization with laser-induced incandescence applied to a laminar premixed ethylene-air flame," *International Journal of Thermal Sciences*, vol. 49, pp. 1457–1467, 2010.

[256] J. Zerbs, K. P. Geigle, O. Lammel, J. Hader, R. Stirn, R. Hadef, and W. Meier, "The influence of wavelength in extinction measurements and beam steering in laser-induced incandescence measurements in sooting flames," *Applied Physics B: Lasers and Optics*, vol. 96, pp. 683–694, 2009.

[257] S. Maffi, S. De Iuliis, F. Cignoli, and G. Zizak, "Investigation on thermal accommodation coefficient and soot absorption function with two-color Tire-LII technique in rich premixed flames," *Applied Physics B: Lasers and Optics*, vol. 104, no. 2, pp. 357–366, 2011.

[258] E. K. Yapp, R. I. Patterson, J. Akroyd, S. Mosbach, E. M. Adkins, J. Houston Miller, and M. Kraft, "Numerical simulation and parametric sensitivity study of optical band gap in a laminar co-flow ethylene diffusion flame," *Combustion and Flame*, vol. 167, pp. 320–334, 2016.

[259] C. Saggese, A. Cuoci, A. Frassoldati, S. Ferrario, J. Camacho, H. Wang, and T. Faravelli, "Probe effects in soot sampling from a burner-stabilized stagnation flame," *Combustion and Flame*, vol. 167, pp. 184–197, may 2016.

[260] C. Saggese, A. Frassoldati, A. Cuoci, T. Faravelli, and E. Ranzi, "A wide range kinetic modeling study of pyrolysis and oxidation of benzene," *Combustion and Flame*, vol. 160, pp. 1168–1190, jul 2013.

[261] E. Ranzi, A. Frassoldati, R. Grana, A. Cuoci, T. Faravelli, A. Kelley, and C. Law, "Hierarchical and comparative kinetic modeling of laminar flame speeds of hydrocarbon and oxygenated fuels," *Progress in Energy and Combustion Science*, vol. 38, pp. 468–501, aug 2012.

[262] "Sooting Yale Coflow Diffusion Flames," url: http://guilford.eng.yale.edu/yalecoflowflam, Updated in 2016.

[263] R. Piazza, "Thermophoresis: Moving particles with thermal gradients," *Soft Matter*, vol. 4, no. 9, pp. 1740–1744, 2008.

[264] S. Chapman, T. G. Cowling, and D. Park, "The Mathematical Theory of Non-Uniform Gases," *American Journal of Physics*, vol. 30, no. 5, pp. 389–389, 1962.

[265] H. Guo, F. Liu, G. J. Smallwood, and Ö. L. Gülder, "The flame preheating effect on numerical modelling of soot formation in a two-dimensional laminar ethylene-air diffusion flame," *Combustion Theory and Modelling*, vol. 6, pp. 173–187, jun 2002.

[266] H. Jin, A. Cuoci, A. Frassoldati, T. Faravelli, Y. Wang, Y. Li, and F. Qi, "Experimental and kinetic modeling study of PAH formation in methane coflow diffusion flames doped with n-butanol," *Combustion and Flame*, vol. 161, pp. 657–670, mar 2014.

[267] H. Jin, W. Yuan, Y. Wang, Y. Li, F. Qi, A. Cuoci, A. Frassoldati, and T. Faravelli, "Experimental and kinetic modeling study of laminar coflow diffusion methane flames doped with 2-butanol," *Proceedings of the Combustion Institute*, vol. 35, pp. 863–871, jan 2015.

[268] H. Jin, A. Frassoldati, Y. Wang, X. Zhang, M. Zeng, Y. Li, F. Qi, A. Cuoci, and T. Faravelli, "Kinetic modeling study of benzene and PAH formation in laminar methane flames," *Combustion and Flame*, vol. 162, pp. 1692–1711, may 2015.

[269] A. Cuoci, A. Frassoldati, T. Faravelli, H. Jin, Y. Wang, K. Zhang, P. Glarborg, and F. Qi, "Experimental and detailed kinetic modeling study of PAH formation in laminar co-flow methane diffusion flames," *Proceedings of the Combustion Institute*, vol. 34, pp. 1811–1818, jan 2013.

[270] I. S. Jayaweera and P. D. Pacey, "The formation of hydrogen in ethylene pyrolysis at 900 K," *International Journal of Chemical Kinetics*, pp. 719–729, sep.

[271] R. J. Hall, "The radiative source term for plane-parallel layers of reacting combustion gases," *Journal of Quantitative Spectroscopy and Radiative Transfer*, vol. 49, pp. 517–523, may 1993.

[272] T. Poinsot and D. Veynante, *Theoretical and numerical combustion*. Edwards, 2005.

[273] L. Talbot, R. K. Cheng, R. W. Schefer, and D. R. Willis, "Thermophoresis of particles in a heated boundary layer," *Journal of Fluid Mechanics*, vol. 101, p. 737, dec 1980.

[274] M. Roussillo, *Thesis, Development of multiple optical diagnostics for soot and application to confined swirling premixed sooting flames under rich conditions*. PhD thesis, Université Paris-Saclay, 2009.

APPENDIX $\mathcal{A}$

Appendix: Conservation and transport equations solved at the numerical simulations

The following conservation equations solved by the laminarSMOKE code: mass (Eq. A.1), momentum (Eq. A.2), species mass (Eq. A.3) and energy (Eq. A.4) are presented with details on the specific terms.

$$\frac{\partial \rho}{\partial t} + \nabla(\rho \boldsymbol{v}) = 0 \tag{A.1}$$

$$\frac{\partial (\rho \boldsymbol{v})}{\partial t} + \nabla(\rho \boldsymbol{v}\boldsymbol{v} + p\boldsymbol{I}) = \nabla \boldsymbol{T} + \rho \boldsymbol{g} \tag{A.2}$$

$$\frac{\partial (\rho Y_k)}{\partial t} + \nabla(\rho Y_k \bar{v}) = -\nabla(\rho Y_k \bar{V}_k) + \dot{\Omega}_k \qquad k = 1, ..., N_c \tag{A.3}$$

$$\rho C_p \frac{\partial T}{\partial t} + \rho C_p \bar{v} \nabla T = -\nabla \bar{q} - \rho \nabla T \sum_{k=1}^{N_c} C_{P,k} Y_k \bar{V}_k - \sum_{k=1}^{N_c} h_k \dot{\Omega}_k \tag{A.4}$$

where t is the time, ρ is the mixture density, p is the pressure, $\bar{v}$ is the mixture velocity, $\bar{T}$ is the fluid stress tensor, g is the acceleration vector due to gravity, Y_k is the mass fraction of species k, V_k is the diffusion velocity of species k, $\dot{\Omega}_k$ is the formation rate of species k, T is the temperature, C_{p} and $C_{\mathrm{P},k}$ are the specific heat at constant pressure of the mixture and of species k, respectively, q is the heat flux vector, h_{k} is the individual-species enthalpy (i.e., the sum of the sensible and formation enthalpies), and N_{C} is the total number of species in the kinetic scheme.

The equation of state is determined by the ideal gas low:

$$p = \rho \frac{R}{M_{mix}} T \tag{A.5}$$

where M_{mix} is the molecular weight of the mixture and R is the universal gas constant.

In sooting flames, the radiation of soot is important to account for [90]. The radiation is included in the heat flux, both gas radiation and soot radiation, by using the optically thin approach.

$$\bar{q} = -\lambda \nabla T + \bar{q}_{rad} \tag{A.6}$$

where $\bar{q}_{\mathrm{rad}}$ is the radiative heat flux and λ is the mixture thermal conductivity. The gas radiation model considers the optically thin radiation hypothesis, in specific the only H_2O, CO, CO_2 and CH_4 are considered as significantly radiating species, so that the radiative heat contribution in the energy equation is given by:

$$\nabla q_{rad} = -4\sigma a_p (T^4 - T_{env}^4) \tag{A.7}$$

where T_{env} is the environment temperature and σ is the Stefan-Boltzman constant. The Planck mean absorption coefficient (a_{p}) is derived based on the partial pressure of the species (p_k for species k):

$$a_p = p_{H_2O} a_{p,H_2O} + p_{CO_2} a_{p,CO_2} + p_{CO} a_{p,CO} + p_{CH_4} a_{p,CH_4} \tag{A.8}$$

with $a_{\text{p},k}$ being the extinction coefficient of species k from calculations performed by the RADCAL software [271].

The model accounts for the Fick's diffusion and thermophoresis (Soret effect), represented by the $\bar{V}$ diffusion velocity in the transport equation. The Fick's diffusion related to the concentration gradient, can be determined by solving the system [272]:

$$\nabla X_P = \sum_{k=1}^{N_C} \frac{X_P X_k}{\Gamma_{pk}^m} (V_- V_p) + (Y_p - X_p) \frac{\nabla P}{P} + \frac{\rho}{p} \sum_{k=1}^{N_C} Y_p Y_k (f_p - f_k) \quad for\ p = 1...N_C \tag{A.9}$$

with Γ_{pk}^m the binary mass diffusion coefficient of the species k in species p and X_k the mole fraction of species k. However, as solving such a linear system can be computationally expensive, therefore, it is generally simplified, and the law of diffusion is written as:

$$\omega \bar{V}_k^m = -\Gamma_{k,mix}^m \nabla \omega_k \tag{A.10}$$

where $\Gamma_{k,mix}^m$ is the mass diffusion coefficient for the species k in the mixture. Finally resulting the molecular diffusive flux ($\bar{J}_k^m$):

$$\bar{J}_k^m = -\rho \Gamma_{k,mix}^m \nabla \omega_k \tag{A.11}$$

The expression of thermophoretic diffusion is given by assuming spherical particles in free molecular regime ($Kn_p >> 1$) [273]:

$$\bar{V}_k^{Th} = -0.538 \nu \frac{\nabla T}{T} \tag{A.12}$$

APPENDIX $\mathcal{B}$

Appendix: Harmonically forced F80 flame

Simulations of the harmonically forced F80 flame, with 20% modulation and a frequency of 10 and 30 Hz, were performed and numerical results are compared to experimental data [274] in terms of soot volume fraction in Figure B.3 and B.4, respectively. Furthermore, the steady flames with $\pm 20\%$ inlet velocity modulation were simulated and experimentally investigated ("Static flame" in Figure B.3 and B.4) in order to obtain the corresponding steady flames for the minimum ("M-20") and maximum ("M20") inlet velocity.

At the lower frequency the flame is passing through almost quasi steady state conditions, as the upper and the lower part of the flame follows the profiles predicted with the $\pm 20\%$ statically modulated flames. As the modulation of the inlet velocity is not instantaneously appearing at the different HABs, the harmonically modulated flame has a longer flame length around 50-60 ms, than the "M20" static flame, and a shorter one around 90-0 ms compared to "M-20". These characteristics were recovered by the numerical simulation.

However, the numerical and experimental phase shifts between the instantaneous total soot mass and velocity fluctuation differ. In Figure B.1 the integrated f_v (I_{f_v}) fluctuation relative to the M0 case is presented for both simulation and experiment. While the phase shift between experimental I_{f_v} and inlet velocity signals is $-\pi$, the numerical simulation is shifted by -1.1π. However, if a shift of 0.11π is applied ("Num Schifted" in Figure B.1) the numerical and experimental response is in good agreement. In the figure, the I_{f_v} level of the static flames, "M20" and "M-20", are highlighted (blue lines for experiments and green lines for simulations). Both experimental and numerical results show that the fluctuating flame's I_{f_v} remains in the scale of the static extremes of I_{f_v}. Furthermore, the I_{f_v} fluctuation is not exactly sinusoidal, the decrease from the maximum is more rapid than the increase from the minimum.

At the higher frequency, the measurement shows a profile different from the static cases, "M20" and "M-20". The upper sooty region becomes narrower between 20 and 26.6 ms. The numerical simulations do not capture this phenomenon, the flame barely responses to the excitation. This damping may be a result of not well predicted chemical characteristic times, or of an unsatisfying mesh resolution, as the possibility of latter was not yet excluded. To obtain further conclusions additional tests would be required, including mesh dependency investigations.

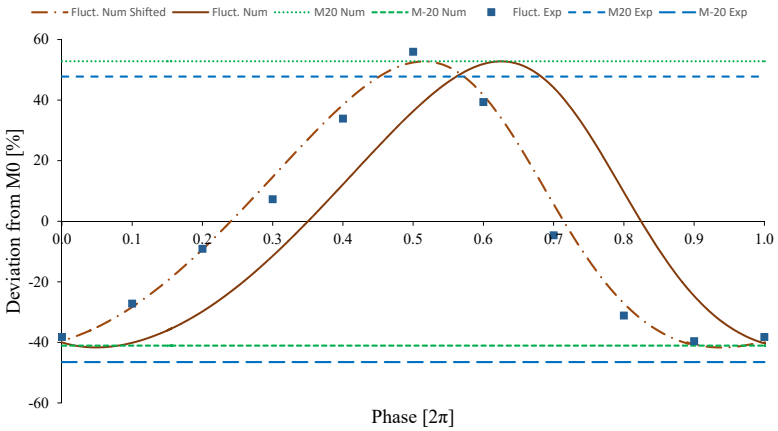

Figure B.1: *Soot integral response to harmonically modulated velocity inlet of F80, 20% modulation 10 Hz frequency*

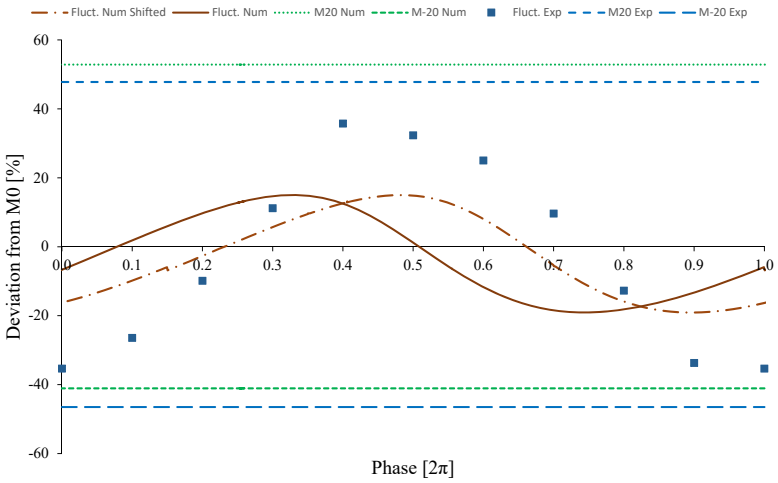

Figure B.2: *Soot integral response to harmonically modulated velocity inlet of F80, 20% modulation 30 Hz frequency.*

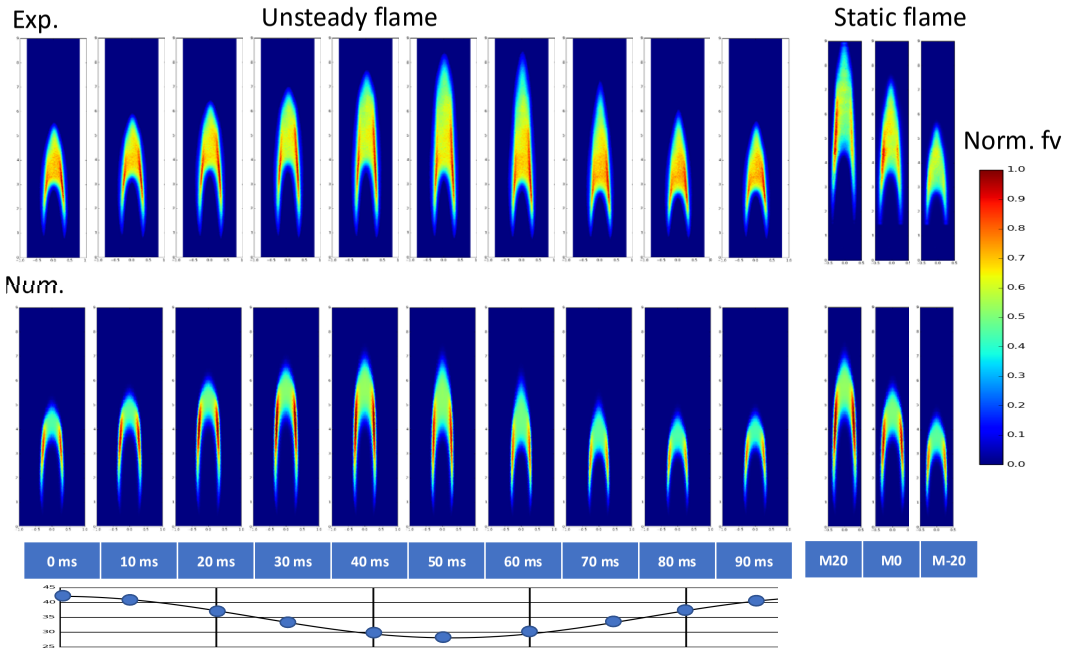

Figure B.3: *Experimental and numerical normalized soot volume fraction for F80 with a harmonically modulated inlet velocity at a frequency of 10 Hz and an amplitude of 20%. Lower plot: inlet bulk velocity.*

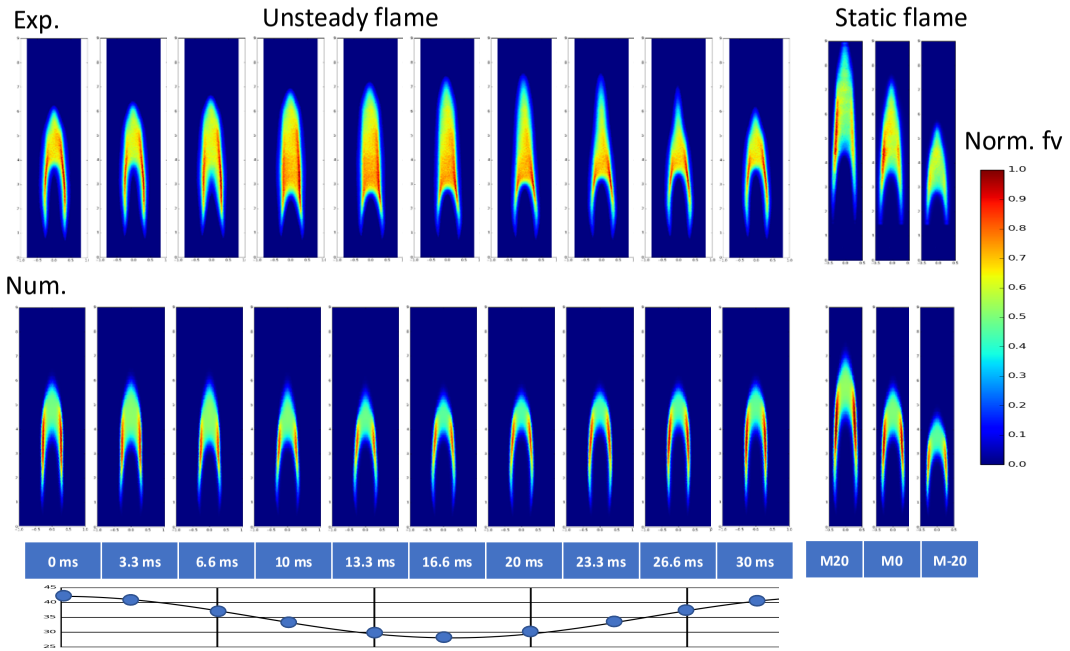

Figure B.4: *Experimental and numerical normalized soot volume fraction for F80 with a harmonically modulated inlet velocity at a frequency of 30 Hz and an amplitude of 20%. Lower plot: inlet bulk velocity.*

APPENDIX C

Extended french abstract

La combustion des carburants hydrocarbonés peut conduire à la formation de particules carbonées. D'une part, une combustion incomplète peut conduire à la formation de sous-produits non désirés: les suies. Les suies sont un polluant nocif, dangereux pour l'environnement et la santé humaine. Les particules de suie influencent le climat de façon directe et indirecte lorsqu'elles pénètrent dans l'atmosphère, du fait de leur capacité à absorber la lumière. Ces particules sont inhalées du fait de leur petite taille et peuvent pénétrer les régions les plus profondes du système respiratoire. Elles peuvent aggraver les maladies respiratoires, cardiovasculaires, infectieuses ou les réactions allergiques. Une corrélation entre leur concentration dans l'air et les risques de cancer a été établie.

D'autre part, le produit de base de beaucoup de produits quotidiens est le noir de carbone, produit final d'une combustion en conditions riches de carburants hydrocarbonés, contrôlée industriellement. Du fait de ses nombreuses propriétés avantageuses, il est utilisé pour renforcer les pneus automobiles, le caoutchouc, ou comme pigment dans les plastiques, peintures et encres. La surface et la morphologie jouent un rôle important dans l'utilisation et les effets négatifs de ces particules carbonées générées par la combustion. Il est donc crucial de posséder des informations sur leurs propriétés, telles que leur masse et leur volume.

La taille et la morphologie des particules de suies varient significativement du fait de la complexité des procédés de formation comme la nucléation, la croissance de surface, le mécanisme HACA, la déshydrogénation, la coalescence, l'agrégation et l'oxydation. Tous les procédés mentionnés ci-dessus, et par conséquent les caractéristiques de chaque particule, dépendent de nombreux paramètres tels que la température, la pression, la composition chimique des gaz lors de leur formation. Le temps de résidence d'une particule de suie dans différentes régions est également de grande importance. Par conséquent, le champ d'écoulement fluide joue un rôle significatif. Alors que la surface des particules sphériques, en général nouvellement formées, a une relation sans équivoque au volume, pour déterminer la surface des agrégats, en plus de connaissance du volume, des informations sur la morphologie et donc sur les particules primaires est nécessaire.

Cet intérêt croissant pour la prédiction de l'évolution des particules de suies en termes de surface et de morphologie nous pousse à étendre les modèles numériques pour prédire ces caractéristiques. De plus, du fait que la taille des particules primaires influence les procédés chimiques et de collision, les prédictions du model peuvent être améliorées par la prise en compte de ce paramètre. La modélisation de la formation des suies peut avoir comme but d'améliorer la compréhension de ce procédé extrêmement complexe, ou d'améliorer la production de noir de carbone. Les exigences et les attentes quant à la performance du modèle sont donc nombreux.

Les flames laminaires multidimensionnelles, comme la flame de diffusion laminaire en co-courant, sont moins complexes que les flammes des systèmes de combustion industriels. Les procédés de formation

des suies sont cependant analogues dans les deux cas, une investigation poussée de ces flammes se révèle donc être intéressante. Pour obtenir une description détaillée des procédés chimiques tout en gardant le coÃ»t numérique à un niveau acceptable, l'utilisation des modèles sectionnels chimiques discrets (CDSMs en anglais) est un choix approprié. Dans leur version actuelle ces modèles ne donnent pas d'information sur la distribution de taille des particules primaires, leur développement a donc un intérêt particulier.

Une stratégie numérique pour déterminer la taille des particules primaires utilisant les CDSMs est donc présentée. La stratégie proposée se base sur la résolution de l'équation de transport de la nouvelle variable, la densité du nombre de particules primaires, pour chaque section d'agrégat considérée. Par cette méthode, la taille moyenne des particules primaires pour chaque BIN peut être suivie. Le terme source chimique dans l'équation de transport est basé sur les réactions chimiques et les taux de réactions chimiques procurés par le CDSM. Il est supposé que les particules primaires sont en contact dans les agrégats. Cependant, le model proposé prend en compte l'oblitération causée par la croissance de surface and l'effet similaire de la coagulation en réduisant le nombre de particules primaires dans les agrégats. La stratégie proposée est ajoutée au CDSM développé par le groupe de modélisation CRECK, sans considérer de couplage entre le mécanisme cinétique et les résultats sur les tailles de particules.

Pour la validation du modèle, la taille moyenne des particules primaires obtenue de façon expérimentale peut être utilisée comme référence. L'analyse microscopique des particules échantillonnées par thermophorèse est une approche fréquemment utilisée. L'observation directe de la particule permet de gagner des informations sur la taille des particules également. La technique d'Incandescence Induite par Laser résolue temporellement (TiRe-LII en anglais) est de nos jours une méthode expérimentale populaire, du fait que, contrairement à l'approche mentionnée auparavant, elle est non-intrusive et peut donner une haute résolution spatio-temporelle. La comparaison des tailles de particules primaires obtenues numériquement et expérimentalement est cependant sujette à certaines incertitudes. The PPSD émettant le signal détecté est recherché dans l'expérience TiRe-LII en comparant le signal incandescent de nombreux possibles PPSD reconstruits numériquement avec le signal détecté expérimentalement. Cette approche requiert plusieurs autres paramètres en plus du signal d'incandescence ; des mesures supplémentaires sont donc nécessaires, ou certaines hypothèses doivent être faites concernant ces paramètres. Ces deux méthodes peuvent également accroître les incertitudes. La plupart des paramètres d'entrée pour modéliser le signal LII sont en général disponibles avec une bonne fiabilité, grÃ¢ce aux simulations numériques où la taille des particules primaires est investiguée. Afin d'assurer une validation plus compréhensive, une approche supplémentaire est proposée. Elle est basée sur la comparaison directe du signal d'incandescence détecté avec celui reconstruit à partir des résultats numériques (méthode directe). L'efficacité de cette méthode «directe» est démontrée a priori par la quantification des erreurs potentielles évitées par la nouvelle stratégie.

La sensibilité des paramètres du modèle, tels que la plus petite taille de particule s'agrégeant et l'utilisation d'un paramètre de correction représentant l'effet d'arrondi de surface, est explorée pour les flammes de prémélange et en co-courant. Pour comprendre l'effet de la dilution du courant de carburant sur la taille des particules and la flamme de co-courant, l'interaction flamme-écoulement et l'effet de la dilution sur la structure de la flamme sont d'abord étudiés. Ensuite, la corrélation entre la température, les concentrations en précurseurs, la fraction volumique de suies and le diamètre des particules primaires est examiné. Enfin, les taux de formation et le temps de résidence le long des trajectoires des particules sont étudiés afin de comprendre l'effet de la dilution sur la localisation spatiale des plus grosses particules le long de la flamme.

université PARIS-SACLAY
ÉCOLE DOCTORALE
Sciences mécaniques et énergétiques, matériaux et géosciences (SMEMAG)

Titre : Modélisation numérique de la formation et de l'évolution de la suie dans les flammes laminaires avec cinétique détaillée

Mots clés : suie, flammes laminaires, cinétique détaillée, particules primaires

Résumé : Les suies de combustion sont principalement connues pour leur caractère nocif, dans le cas des feux de forêt, de fumées de cheminées ou d'émissions polluantes d'un tuyau d'échappement. Cependant, le noir de carbone, un produit industriel de combustion d'hydrocarbures largement utilisé dans notre vie quotidienne.

La surface d'une particule de suies ou de noir de carbon joue un rôle important tant au niveau de son utilisation que de son effet nocif. Il est donc important de connaître la masse, le volume ainsi que la morphologie des suies. En particulier, la surface des particules est un paramètre important pour prédire leur utilisation ainsi que leur effet nocif. Les suies sont généralement des agrégats présentant une structure fractale constituée d'éléments de forme sphérique, appelés particules primaires. Il est possible de connaître la surface des agrégats à partir de la distribution en taille de particules primaires (PPSD-Primary particules size distribution). Compte tenu de l'intérêt grandissant pour la surface des particules et leurs évolutions, il est aujourd'hui nécessaire d'étendre les modèles numériques pour la prévision de la PPSD. De plus, comme la taille des la particules primaires influence les processus chimiques et les processus de collision, la prise en compte de ce paramètre peut améliorer les prévisions des modèles.

Les flammes multidimensionnelles laminaires, comme les flammes de diffusion, sont moins complexes que les flammes rencontrées dans les systèmes de combustion industriels. Cependant, les processus de formation de suies sont analogues dans les deux cas, ce qui rend l'étude de ces flammes intéressante. Afin d'obtenir une description détaillée des processus chimiques ayant lieu dans ces flammes tout en maintenant le coût de calcul à un niveau abordable, l'utilisation de modèles sectionnels discrets chimiques (CDS-chemical discret sectional methods) est un choix approprié. Le développement de modèles CDS est au coeur de cette thèse.

D'abord, une stratégie numérique pour déterminer la taille des particules primaires est présentée dans le contexte des modéles CDS. Elle repose sur la résolution d'une équation de transport pour la densité en nombre de particules primaires pour chaque section d'agrégats considérée. Pour valider la taille des particules primaires déterminée numériquement, les résultats doivent être comparés avec des données expérimentales obtenues via la technique d'Incandescence Induite par Laser résolue temporellement (TiRe-LII). Cette comparaison, dite inverse, est affectée par les incertitudes expérimentales et les hypothèses sous-jacentes au post-traitement du signal TiRe-LII pour obtenir la PSD. Pour améliorer la stratégie de validation, une nouvelle approche, dite directe, est proposée pour la validation de la PPSD à partir des données obtenues par TiRe-LII. Elle est basée sur la reconstruction numérique de l'évolution temporelle du signal d'incandescence à partir des résultats numériques et de sa comparaison avec le signal mesuré. L'efficacité de l'approche proposée est démontrée a priori en évaluant l'erreur potentiellement évitée par la nouvelle stratégie.

Le modèle proposé pour le suivi des particules primaires est ensuite validé en utilisant à la fois les approches 'directe' et 'inverse' sur les flammes cibles issues de l'International Sooting FlameWorkshop (ISF): une flamme pré-mélangée éthylèneair et une flamme de diffusion coflow avec deux dilutions différentes. Le caractère général du modèle est discuté en effectuant une étude de sensibilité des résultats aux paramètres du modèle même. Enfin, le modèle est utilisé pour comprendre l'effet de la dilution du combustible sur la taille des particules primaires dans les flammes de diffusion en examinant les corrélations possibles entre phase gazeuse et phase solide ainsi que l'évolution temporelle des particules le long de leur trajectoires.

Université Paris-Saclay
Espace Technologique / Immeuble Discovery
Route de l'Orme aux Merisiers RD 128 / 91190 Saint-Aubin, France 0

université PARIS-SACLAY
ÉCOLE DOCTORALE
Sciences mécaniques et énergétiques, matériaux et géosciences (SMEMAG)

Title : Numerical modeling of soot formation and evolution in laminar flames with detailed kinetics

Keywords : soot, laminar flames, detailed kinetics, primary particles

Abstract :
An image appearing when the phrase soot is heard is the smoke emitted by an exhaust pipe. The imperfect combustion of hydrocarbon fuels is a source of this harmful pollutant. The industrially controlled combustion of hydrocarbons can provide the carbon black, an industrial product widely used in our everyday life. For both its utilization and its harming effect, the surface of these combustion generated particles plays an important role, therefore, it is of interest to possess information on the particle morphology beside its mass or volume.
Soot particles were found, at various conditions, to have a fractal-like structure built up from spherical shape building blocks, so-called primary particles. This increased interest in the particle surface and its evolution gives the motivation to extend numerical models to provide related information, i.e. particle surface or primary particle size. Furthermore, as the primary particle size influences the chemical and collisional processes, accounting for this parameter can improve the model predictions.
The requirements for numerical models are various depending on the purpose of the simulation. Multidimensional laminar flames, like a laminar coflow diffusion flame, are less complex than flames of industrial combustion systems. However, the soot formation processes are analogous in the two cases, therefore, the investigation of these flames are of interest. In order to obtain a detailed description of the chemical processes, while keeping the computational cost in these flames at an affordable level, using chemical discrete sectional models is a suitable choice. As in their current version, these models do not provide information on the primary particle size their development in this direction is of interest.
Guided by the above motivation, a numerical strategy to determine the primary particle size is presented in the context of the chemical sectional models. The proposed strategy is based on solving the transport equation of the primary particle number density for each considered aggregate section.
In order to validate numerical primary particle size, the comparison to experimental data is required. Due to its numerous advantages, the Time-Resolved Laser-Induced Incandescence (TiRe-LII) technique is a nowadays popular experimental method. However, the comparison of the numerically and the experimentally obtained primary particle size may be charged with uncertainties introduced by the additional measurements or assumptions of the numerous parameters required to derive primary particle size from the detected signal.
In order to improve the validation strategy, an additional approach for primary particle size distribution validation with TiRe-LII is proposed. This is based on the reconstruction of the temporal evolution of incandescence from the numerical results and its comparison with the measured signal. The effectiveness of this 'forward' method is demonstrated a priori by quantifying the errors potentially avoided by the new strategy.
The validity of the proposed primary particle tracking model is tested by both the traditional 'inverse' and the 'forward' method on target flames of the International Sooting Flame (ISF) Workshop. In particular a laminar premixed ethylene flame is considered first. Then, two laminar coflow ethylene flames with different dilutions are put under the scope. The sensitivity to the model parameters, such as accounting for the surface rounding and the choice of smallest aggregating particle size, is explored in both the premixed flame and in the coflow flame with highest ethylene content.
To understand the effect of the fuel stream dilution on the primary particle size in the coflow flame, first, the flame-flow interaction and the effect of the dilution on the flame structure is investigated. Then, the correlation between the temperature, the precursor concentrations, the soot volume fraction, and the primary particle diameter is examined. Finally, the formation rates and the residence time along the particle trajectories are studied to understand the effect of dilution on the spatial localization of the biggest particles along the flame.

Université Paris-Saclay
Espace Technologique / Immeuble Discovery
Route de l'Orme aux Merisiers RD 128 / 91190 Saint-Aubin, France